

**AIRBORNE SYNTHETIC APERTURE RADAR, DIGITAL TERRAIN MODELS,  
AND GEOGRAPHIC INFORMATION SYSTEMS:  
TOOLS FOR MAPPING AND MANAGING LARGE LANDSLIDE HAZARDS  
IN SOUTHWESTERN BRITISH COLUMBIA**

by

**MARK CHARLES LEIR**  
B.A.Sc., The University of British Columbia, 1990

**A THESIS SUBMITTED IN PARTIAL FULFILLMENT  
OF THE REQUIREMENTS FOR THE DEGREE OF  
MASTER OF APPLIED SCIENCE**

in

**THE FACULTY OF GRADUATE STUDIES**

(Department of Geological Sciences)  
(Geological Engineering Program)

We accept this thesis as conforming  
to the required standard

**THE UNIVERSITY OF BRITISH COLUMBIA**

July 1995  
© Mark Charles Leir

In presenting this thesis in partial fulfilment of the requirements for an advanced degree at the University of British Columbia, I agree that the Library shall make it freely available for reference and study. I further agree that permission for extensive copying of this thesis for scholarly purposes may be granted by the head of my department or by his or her representatives. It is understood that copying or publication of this thesis for financial gain shall not be allowed without my written permission.

Department of Geological Sciences

The University of British Columbia  
Vancouver, Canada

Date July 31, 1995

## ABSTRACT

This research demonstrates the use of airborne synthetic aperture radar (SAR) and Geographic Information Systems (GIS) for mapping and predicting large rock landslide occurrences in southwestern British Columbia.

Lineaments in the Chilliwack area are mapped using geocoded 10 m resolution 1:20,000, 1:50,000, and 1:80,000 scale C-band SAR and compared to lineaments mapped with 1:50,000 scale black and white stereo airphotos. SAR lineament length and trend correlate well with airphoto lineaments and provide additional structural information about the Chilliwack area. Testing the ability of SAR to locate specific airphoto lineaments reveals that SAR tends to find the longer airphoto lineaments.

SAR is useful for detecting geomorphological landslide features such as lineaments, antislope scarps, deformation zones, and especially hummocky debris lobes, cone and fans. In areas covered by cultivation, logging activity, or mature forest, SAR proves most useful for revealing landslide debris and lineaments especially where tree canopy height corresponds subtle changes in ground morphology. Depending on the viewing geometry, SAR is able to detect landslide source and deposition zones not apparent in stereo airphotos.

Spatial relationships between regional faults, lineaments, plutonic contacts, bedrock geology, slope angle, and landslide hazard occurrence are explored using the IDRISI GIS and an objective multivariate statistical methodology called weights of evidence. Weights of evidence modelling determines landslide potential for regions where representative landslide occurrences are known, estimates uncertainty, ranks predictive power of input maps, and accounts for missing or incomplete data. The method is particularly well-suited for modelling multiclass maps and proximity to linear features.

The top five predictor maps are: 1) Custer Gneiss; 2) within 1300 m of a fault trace; 3) within 1200 m of a lineament; 4) Cultus Formation; 5) Chilliwack Formation, and; 5) Spuzzum Pluton. The proximity to a plutonic contact and slopes less than 20° are not positive predictors of landslide occurrence.

Predictor map weights are combined and map of posterior probability for predicting landslide occurrence is created. Areas of relative high landslide occurrence include the Fraser Canyon near Yale, the slopes above Chilliwack and the upper Chilliwack Valley, and adjacent to the Ross Lake Fault south of Hope. Adding this hazard zonation map with socio-economic criteria and landslide runout models within a GIS builds risk maps essential for development planning in mountainous terrain.

## TABLE OF CONTENTS

ABSTRACT.....	ii
TABLE OF CONTENTS .....	iv
LIST OF TABLES.....	vi
LIST OF FIGURES .....	vii
LIST OF PLATES .....	viii
ACKNOWLEDGMENTS.....	ix
CHAPTER 1      INTRODUCTION.....	1
1.1 Background.....	1
1.2 Research Synopsis.....	2
1.3 Thesis Structure .....	2
CHAPTER 2      HOPE STUDY AREA .....	4
2.1 Location.....	4
2.2 Physiographic Setting.....	4
2.2 Regional Geology.....	6
2.2.1 Lithology.....	6
2.2.2 Tectonic Setting.....	7
2.3 Glaciation and Quaternary History.....	9
CHAPTER 3      LANDSLIDE INVENTORY IN THE HOPE STUDY AREA.....	11
3.1 Introduction.....	11
3.2 Inventory Methodology.....	14
3.3 Characteristics of Landslides in the Inventory .....	14
3.4 Morphological and Spectral Landslide Indicators from Airphotos.....	15
3.5 Factors Affecting Landslide Distribution.....	18
3.6 Conclusions.....	21
CHAPTER 4      LINEAMENT AND LANDSLIDE HAZARD MAPPING WITH AIRBORNE SAR.....	23
4.1 Introduction.....	23

4.2 Introduction to Airborne SAR.....	23
4.3 SAR Applications in Geology .....	24
4.4 Scope .....	26
4.5 Chilliwack SAR Data and Study Site .....	26
4.6 SAR Image Processing and Enhancement.....	31
4.7 Lineament Mapping Methodology.....	32
4.8 Lineament Mapping Results .....	33
4.9 Landslide Hazard Mapping Methodology.....	41
4.10 Hazard Mapping Results .....	41
4.11 Conclusions.....	47
CHAPTER 5 LANDSLIDE HAZARD ZONING USING AN OBJECTIVE GIS MODEL.....	49
5.1 Introduction.....	49
5.2 Weights of Evidence Method .....	52
5.3 Data Inputs .....	55
5.4 Binary Map Reclassification.....	56
5.5 Conditional Independence .....	64
5.6 Results.....	66
5.7 Conclusions.....	69
CHAPTER 6 CONCLUSIONS .....	72
REFERENCES .....	76
APPENDIX I SUMMARY OF THE HOPE STUDY AREA GEOLOGIC HISTORY .....	86
APPENDIX II CHILLIWACK SAR PARAMETERS .....	88
APPENDIX III WEIGHTS OF EVIDENCE CALCULATIONS .....	90
APPENDIX IV NON-GEOLOGIC ACRONYMS AND TERMINOLOGY .....	99

## LIST OF TABLES

- Table 4.1. Airphoto lineaments located with SAR.
- Table 4.2. Chilliwack lineament data from Savigny (1995) and from this study.
- Table 5.1. Weights, standard deviations, and contrasts for bedrock geology ranked by the Studentized value of contrast  $C/s(C)$ .
- Table 5.2. Variation of weights of evidence with cumulative distance from faults. Studentized contrast  $C/s(C)$  is a maximum at 1300 m from the faults.
- Table 5.3. Values of Cramer coefficient  $V$  for quantifying conditional independence between lineaments, faults, selected geology and slope maps.
- Table 5.4. Positive and negative weights, sample variances, and contrast for all predictor maps. Maps are ranked by the Studentized value of contrast  $C/s(C)$ .

## LIST OF FIGURES

- Figure 2.1. Location map of the Hope study area.
- Figure 2.2. Intrusions and faults in the Hope study area. Adapted from Monger (1989).
- Figure 3.1. Landslide and lineament inventory for the Hope study area. Adapted from Savigny (1995) and English (*pers. comm.*).
- Figure 3.2. The Hope Fault seen in BC TRIM DEM.
- Figure 4.1. Chilliwack SAR viewing geometry.
- Figure 4.2. Chilliwack SAR image in relation to the Hope study area.
- Figure 4.3. SAR study area including five landslide hazards.
- Figure 4.4. Histograms of lineament frequency vs. length.
- Figure 4.5. Observed average lineament frequency and length vs. image scale for Appalachian airphoto lineaments (Shuman 1991), Chilliwack airphotos lineaments, and Chilliwack SAR lineaments.
- Figure 4.6. Histograms of lineament frequency vs. trend.
- Figure 4.7. Lineaments located with 1:50,000 scale airphotos and SAR, airphotos only, and SAR only.
- Figure 4.8. Histograms of lineament frequency vs. trend for airphoto lineaments located with SAR imagery.
- Figure 4.9. Location of Savigny (1995) Chilliwack airphoto lineaments and Chilliwack SAR lineaments.
- Figure 4.10. The Wahleach hazard seen from (a) airphotos and (b) airborne SAR.
- Figure 4.11. Cheam Slide, Popkum Slide, and debris cones seen in an airphoto.
- Figure 4.12. Cheam Slide, Popkum Slide, and debris cones seen in airborne SAR.
- Figure 5.1. Schematic diagram of GIS models within a landslide hazard expert system. Shaded components are addressed in this study.
- Figure 5.2. Bedrock geology and faults in the Hope study area. Adapted from Monger (1989).
- Figure 5.3. Fault buffers with faults and landslide hazards superimposed.
- Figure 5.4. Posterior probability map of landslide occurrence per hectare. Known landslide occurrences are outlined in white.

## LIST OF PLATES

- Plate 3.1.        The 1965 Hope Slide.
- Plate 3.2.        The prehistoric Katz Slide.
- Plate 3.3.        Lineament located near the headscarp of the Cheam Slide.
- Plate 3.4.        A series of lineaments at Cheekye Ridge, Squamish, B.C.

## ACKNOWLEDGMENTS

This research was made possible by the contribution and efforts of many people and organizations.

Foremost, I wish to thank Dr. K. Wayne Savigny for his patience, inspiration, political guidance, and wealth of opportunity. The members of my committee, Dr. R. Beckie, Dr. M. Journeay, and Dr. P. Murtha provided insightful technical suggestions.

Financial support was provided by the Watershed Management Division of the Greater Vancouver Regional District (V. Cameron and T. Griffing). Airborne SAR and Landsat TM imagery was loaned by the Canada Centre of Remote Sensing (V. Singhroy) and technical details tackled by D. Bedard. The B.C. Ministry of Environment Lands and Parks (R. Balser and R. Yazdani) loaned the BC TRIM DTM and 1:250,000 scale DEM data. G. Maedel and D. Stebbins at the University of British Columbia Faculty of Forestry FIRMS research lab provided access to PCI EASI/PACE and IDRISI GIS software. Bruce Geotechnical Consultants Inc. provided other important software. Thanks as well to Dr. G. Bonham-Carter at Geological Survey of Canada and C. Livingstone at CCRS for helpful discussions on GIS modelling and SAR interpretation. This research would have been impossible without the support of these people and the unconditional use of their resources.

My sincerest thanks to my family and friends for their patience, stability, and understanding. They provided me valuable opportunities to escape the iridescent glow of the computer monitor to see the real sun.

Thanks as well to K. Everard for sharing The Cave and paving the way with moral support, enlightening discussion, wisdom, and god-like computer knowledge and FORTRAN programming.

## CHAPTER 1

### Introduction

#### 1.1 Background

Worldwide population growth hastens urbanization and resource development of mountainous regions. An array of geologic hazards impedes this trend. The most prevalent are landslides which account for significant social and economic loss. Rapid location, identification, and management of landslide hazards is required so earth scientists, engineers, and urban planners can limit societal exposure to landslide risk.

A 5200 km<sup>2</sup> inventory of large rock landslides and lineaments in the Fraser Valley in southwestern British Columbia was completed by Savigny (1995) using 1:50,000 black and white airphotos. 1292 lineaments and 58 interglacial and post-glacial landslides between 1 million and 550 million cubic metres were located. Savigny proposed that, among other factors, bedrock lithology, and the presence of faults and lineaments may control the location of these instabilities.

Given the increasing affordability and computational capability of personal computers combined with the enormous developments in non photographic technology and Geographic Information System (GIS)<sup>1</sup> software, visual interpretation and image processing of digital imagery provides alternative means of creating hazard inventories. Additionally, rapid multivariate quantitative analysis of spatial geographic data for landslide hazard studies is now practical. For example, putting user selected causative factors of landslides and an existing landslide inventory into a rigorous quantitative algorithm within a GIS can produce a map of landslide hazard occurrence. An objectively rather than subjectively

---

<sup>1</sup> A list of non-geologic acronyms and terminology is found in Appendix IV.

derived hazard map helps reduce professional liability and accordingly, the value of it should not be undersold.

This study evaluates digital techniques for mapping large rock instabilities and lineaments and demonstrates a methodology for producing a hazard zonation map using the Savigny (1995) landslide inventory.

## 1.2 Research Synopsis

This research explores methodologies for the location, identification, and management of large rock instabilities in southwestern British Columbia. This research is in two parts. The first part evaluates the potential of airborne Synthetic Aperture Radar (SAR) for mapping landslide and lineament locations in the Chilliwack area by comparing the results to interpreted 1:50,000 black and white airphotos. The second part describes an objective statistical methodology for producing a landslide hazard map for the Hope study area from the Savigny (1995) landslide inventory using the PC based IDRISI GIS.

## 1.3 Thesis Structure

This thesis is divided into six chapters. Chapter one is the introduction, background, research synopsis, and thesis outline. Chapter two introduces the reader to the characteristics, physiography, and geology of the Hope study area. An introduction to the Savigny (1995) landslide and lineament inventory, the geomorphological and spectral characteristics of landslides in the inventory, and factors affecting landslide distribution are described in Chapter three. Chapter four analyses the utility of SAR for lineament and landslide mapping in the Chilliwack study area. Chapter five uses weights of evidence statistical modelling within a GIS to objectively create a landslide hazard map for the Hope study area. Conclusions are summarized in Chapter six. Appendices I through IV include the Hope study area geologic summary, airborne SAR parameters, weights of evidence calculations, and a list of non-geologic acronyms and terminology, respectively.

## CHAPTER 2

### Hope Study Area

#### 2.1 Location

The Hope study area is located 130 km east of Vancouver within the Coast and Cascade mountains of southwestern British Columbia (Fig. 2.1). The 8300 km<sup>2</sup> rectangular area is bounded by latitudes 49° to 50° N and longitudes 121° to 122° W. Population centers include Chilliwack, Harrison Hot Springs, Hope, Yale, and Boston Bar. Hope is the approximate center of the study area. Major highways 1, 3, 5, and 7 traverse the study area linking Vancouver to the interior of British Columbia.

#### 2.2 Physiographic Setting

Three major physiographic regions in the study area include the Coast Mountains, Cascade Mountains, and the Fraser Lowlands. The Fraser River, which drains most of the southern and central interior of British Columbia, traverses the three regions. It flows south through the study area forming the boundary between the Coast Mountains to the west and the Cascade Mountains to the east (Fig. 2.1). At Hope it turns southwest to meander through the Fraser Lowlands continuing west to the Strait of Georgia.

The Coast Mountains are the southeastern corner of a 100 km wide range extending 1700 km north from Vancouver to Yukon. They are comprised mainly of granite and other igneous rocks that have been tectonically uplifted and eroded. East of the Fraser River is the Cascade Mountains. These mountains extend from northern California to southern British Columbia and are composed of metasedimentary, metavolcanics, and some igneous plutons and volcanic rocks.

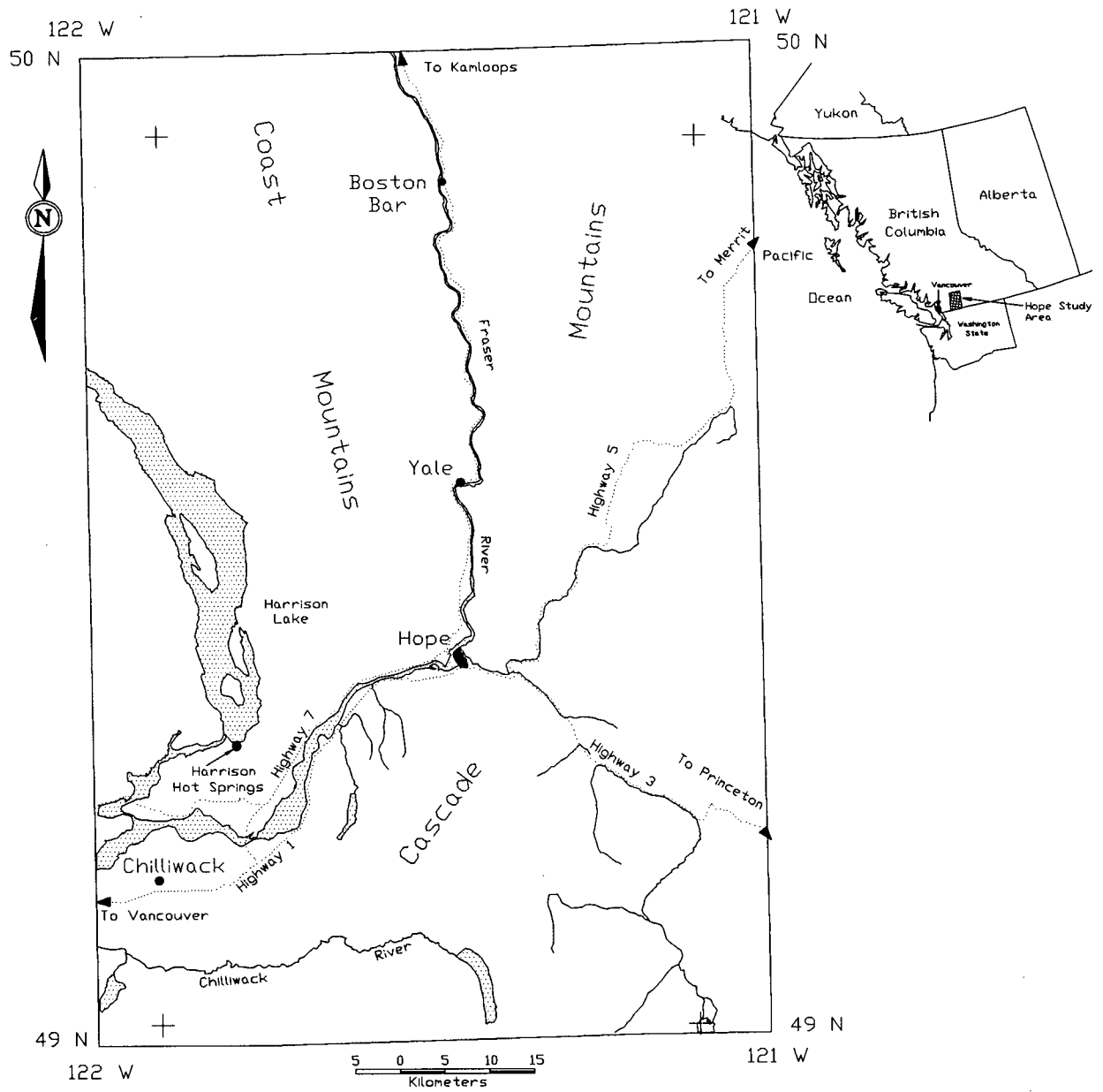


Figure 2.1. Location map of the Hope study area.

The Coast and Cascade mountains are generally rugged with an average local relief of 1250 m and slope angles of 20°. Mountains are deeply dissected, with angular, serrated peaks that often attain heights of 2000 m or more. Permanent ice fields are more common to the west. Mountains less than 1850 m are below the level of the Pleistocene ice sheet and are rounded. Valleys have been glaciated as evidenced by uneven longitudinal and U-shaped profiles, truncated spurs, and hanging side valleys. Drainage is structurally controlled (Monger 1970). The Fraser River above Hope follows a major fault zone and dendritic and radial patterns follow valleys from the high alpine base level. Lower mountain slopes and valleys are heavily timbered with coniferous trees and underbrush. Deciduous trees are less common than conifers and usually grow in valley bottoms and around anthropogenic features throughout the region. Bedrock exposures are uncommon in valley bottoms but are plentiful along valley walls and ridges above 1670 m amidst the low alpine vegetation.

The Fraser Lowlands form the southwestern corner of the British Columbia mainland and the adjoining northwest corner of Washington State. The southwest corner of the study area contains a portion of the Fraser Lowlands. Here the Fraser Lowland is a flat-bottomed northeast trending valley extending from Hope to Chilliwack flanked by the Coast Mountains to the north and the Cascade Mountains to the south. The Fraser River enters the lowlands at Hope and meanders west to Chilliwack where the valley widens to 15 km. Most of the valley is below 50 m elevation with isolated hills reaching heights of 150 m. The organic-rich soils, flat terrain, and gentle climate make this area one of the prime agricultural regions in Canada.

## 2.2 Regional Geology

### 2.2.1 Lithology

The southern Cascade Mountains consist of a north-northwest trending high-grade metamorphic gneiss and granite core zone flanked on both sides by sedimentary and volcanic rocks of lower metamorphic grade (Monger 1970). This core narrows and appears to plunge to the north-northwest beneath rocks of lower metamorphic grade (Monger 1991). Greater uplift in the Coast Mountains has

exposed relatively more granitic rocks than in the Cascade Mountains. Appendix I contains a lithologic and tectonic summary of the study area.

Stratified rocks range in age from middle Devonian to Recent (Monger, 1989). The oldest rocks are Middle Devonian amphibolites and schists and Lower Pennsylvanian to Lower Permian volcanic, chert, pelite, limestone and minor sandstone. Above these are Upper Triassic volcanics and Upper Triassic to Lower Cretaceous pelites, sandstone, conglomerates and volcanics. Capping these are coarse grained Lower Tertiary clastic and volcanic rocks. Pleistocene to Recent deposits locally fill major valleys.

Three separate events of plutonic intrusion have occurred in the study area (Monger 1970). The first is the Late Jurassic-Early Cretaceous emplacement of the foliated Eagle Peak granodiorite. This is followed by the Late Cretaceous intrusion of the massive quartz diorite Spuzzum Pluton (McTaggart and Thompson 1967), Scuzzy Pluton, and other small bodies forming the axis of the Cascades. Early to Middle Tertiary events include the Needle Peak, Mount Outram, Chilliwack and Mount Barr emplacements. The Needle Peak, Scuzzy Plutons, and the Chilliwack Batholith are primarily massive granites and granodiorite with sharp discordant contacts and widely spaced, well developed joints. They contrast with the older granites, which are commonly foliated (Monger 1970). Plutonic intrusions are partly responsible for high grade and contact metamorphism of the surrounding stratified rocks.

### 2.2.2 Tectonic Setting

The structural evolution of the Hope study area may record the final closure of oceanic or marginal basins between the Wrangelia Terrane to the west and the Cretaceous margin of North America to the east (Monger 1991). Crustal unrest represented by metamorphism, deformation, and uplift of Paleozoic to mid-Cretaceous rocks is evident but the characteristic north trending structural pattern of the area was established in a mid-Cretaceous to Early Tertiary orogeny (Monger 1970). Normal and strike-slip faulting in Early Tertiary time and mid-Tertiary to Recent uplift completed the structural evolution of the area. Figure 2.2 show the major faults in the study area mapped by Monger (1989).

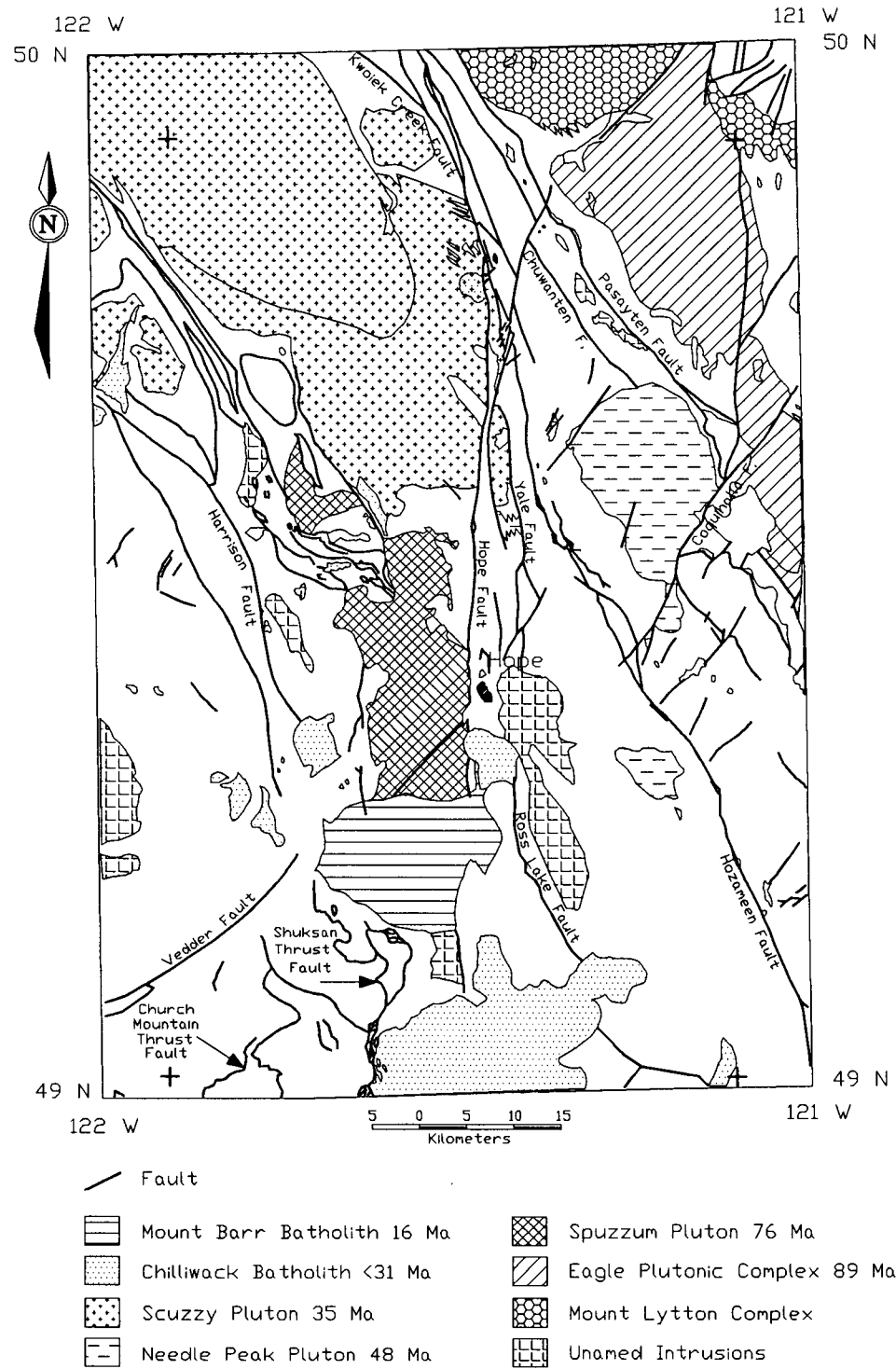


Figure 2.2. Intrusions and faults in the Hope study area. Adapted from Monger (1989).

During the orogeny the high grade gneiss and schist core of the Cascade Mountains was folded, faulted, and intruded by the Tertiary Chilliwack Batholith to the south and the mid-Cretaceous Spuzzum Pluton to the north. Stratified rocks on the east side of the core were folded and thrust eastward along the Hozameen, Chuwanten, and Pasayten reverse faults. Sedimentary and volcanic rocks on the west side of the core were folded and thrust to the southwest and west along east dipping Church Mountain and Shuksan thrust faults. Monger (1985) speculates that the Harrison Fault is a continuation of the fault system north of the Fraser River.

Trending north and cutting across Cretaceous rocks is the Eocene Fraser River Fault, a dextral wrench system with some dip slip displacement. Associated with the system are northwest-trending thrust faults and fold axes and north-trending strike-slip faults (Monger 1991). Near latitude 50°N rocks on the west side of the system are displaced 70 to 90 km to the north relative to the rocks on the east (Monger 1985). In the southern end of this zone are major, subparallel, steeply dipping faults - the Hope Fault to the west, the Yale Fault to the east, and the Ross Lake Fault to the south. In some places the Hope and Yale faults bound a graben with Eocene rocks displaced down on the east side of the Hope Fault. South of Hope the Oligocene Chilliwack Batholith is not faulted indicating movements along these faults have not occurred after emplacement.

The structural evolution of the area was completed with the relatively rapid uplift of the west side of the fault system beginning in the late Eocene time (Parrish 1983).

### 2.3 Glaciation and Quaternary History

Much of the present morphology in the Hope study area is a product of repeated glacial erosion and deposition during the late Wisconsin Fraser Glaciation. The climax of Fraser Glaciation occurred during the Vashon Stade 15,000 to 15,500 years ago (Clague and Luternauer 1983) when ice filled most valleys in southwestern British Columbia to thicknesses of at least 2000 m. By 9,500 years B.P. ice had retreated to the high alpine leaving oversteepened, U-shaped valleys filled with thick (up to 300 m), variable sequences of till, glaciofluvial, glaciolacustrine, and glaciomarine sediment. As meltwater supply and sediment load decreased aggradation was followed by degradation. Today many drainages

have incised sequences of reworked glacial deposits forming terraces up to 300 m thick that flank valley walls. Remnants of characteristic glacial landforms such as kettles, moraines, kames can be seen in the Hope study area. Rebounding of valley walls after removing ice load contributes to mountain top cracking. Mountain cracks, or sackungen, in conjunction with oversteepened valley walls contribute to rock instabilities in the Hope study area (Savigny 1995).

## CHAPTER 3

### Landslide Inventory in the Hope Study Area

#### 3.1 Introduction

Before a landslide hazard study is to begin in an area, general landslide characteristics such as size, type, controlling geologic structure and lithology must be hypothesized so that the study may continue with appropriate remote sensing tools and GIS methodology in hand. In this research the Fraser Valley landslide and lineament inventory provides landslide characteristics. Methodology of data collection and conclusions of this inventory are discussed in this chapter. In particular, morphological and spectral characteristics of inventoried landslides and factors leading to their spatial distribution are summarized. Once summarized, appropriate remote sensing tools and GIS methodology may be selected.

The landslide and lineament data used in this study is included in Figure 3.1. It is comprised of an inventory by Savigny (1995) and an inventory by English (*pers. comm.*)<sup>2</sup>. Savigny (1995) delineates 58 areas of instability and 1292 lineaments within a 40 km wide corridor centered along the Fraser River. 739 lineaments and 3 landslides west of the Savigny corridor were added by English (*pers. comm.*).

Other regional studies focusing on the identification and mapping of a landslide population by remote sensing include: neotectonics and landslides in the Yukon (Everard 1994), earthquake triggered landslides in California (Hansen and Franks 1991), landslide dams in the Canadian Cordillera (Evans 1986), landslides and tectonic assemblages, Canadian Cordillera (Evans 1984a), landslides in Tertiary basalt, Canadian Cordillera (Evans 1984b), large rock avalanches in New Zealand (Whitehouse and

---

<sup>2</sup>1995 personal communication re: Using GIS for debris flow hazard management on the Greater Vancouver Watershed Districts, southwestern British Columbia. Current M.Sc. thesis research, Department of Geological Sciences, University of British Columbia, Vancouver, Canada.

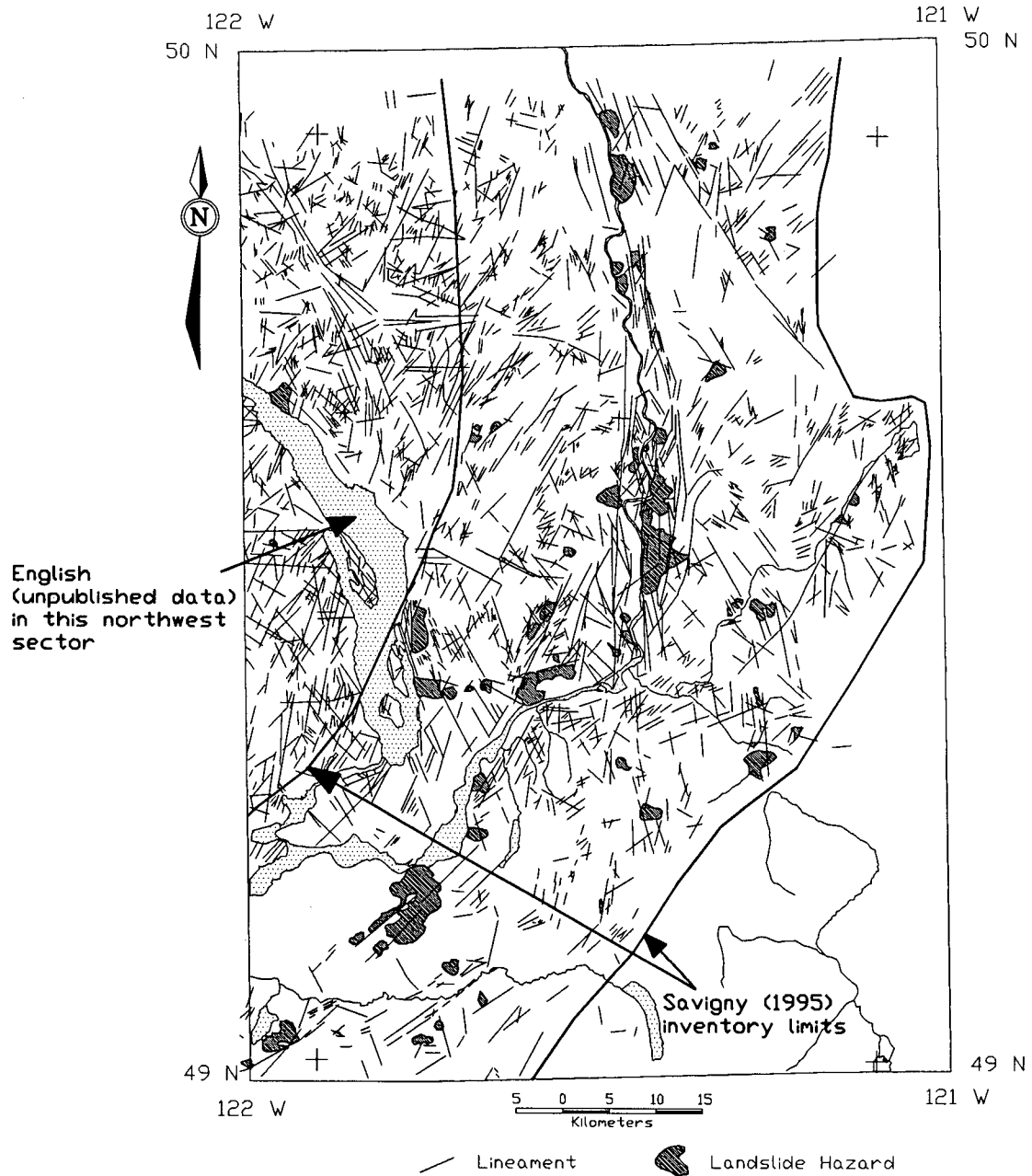


**Figure 3.1.** Landslide and lineament inventory for the Hope study area. Adapted from Savigny (1995) and English (*pers. comm.*).

Griffiths 1983), rock avalanches in the Mackenzie Mountains (Eisbacher 1979), landslides near San Francisco California (Nilsen and Brabb 1977), Fraser Canyon slope stability in British Columbia (Piteau 1977), and large rock landslides in the Canadian Rockies (Cruden 1976).

### 3.2 Inventory Methodology

The landslide and lineament inventory prepared by Savigny (1995) used 1:50,000 scale black and white stereo aerial photographs. Interpreted photographs were annotated, re-checked to improve consistency, and the information was transferred to a 1:250,000 scale topographic base map. Field verification was limited to aerial reconnaissance and short field traverses at approximately one-third of the landslides. The 58 landslide polygons in Figure 3.1 include the scarp, source area, and, if identified, the transportation and deposition zones. These areas show evidence of mass movement (ground cracking, visible displacement) and some have yet to fail catastrophically on a regional scale. Although partially subjective, all mass movement evidence should be included in slope hazard inventories and hazard map production. Full inclusion will create a hazard map describing the landslide potential of the area.

### 3.3 Characteristics of Landslides in the Inventory

Morphology of landslide size, age, activity, and type should be estimated before a remote sensing tool is chosen for landslide mapping. The slide characteristics in the study area are discussed below.

Inventoried landslides range in size from approximately 1 million m<sup>3</sup> to more than 500 million m<sup>3</sup>. The lower limit is the smallest slide that can be identified on a 1:50,000 scale airphoto. All of the landslides, except for the 1965 Hope Slide, are prehistoric, occurring during or shortly after the final stages of Fraser Glaciation (Savigny 1995). This fact has serious implications on landslide mapping. Landslides occurring over 3000 years ago will undoubtedly have subdued morphology, eroded headscarps, and debris hidden by uniform vegetation and anthropogenic features. Therefore most landslide hazards in this study area are not easy to distinguish from surrounding landforms.

Evidence of landslide movement is very difficult to detect at 1:50,000 scale. Recent movements will disturb the ground cover (i.e. stressed vegetation, eroded rock and soil) and may be detected from

high resolution/large scale imagery. The presence of smaller and more recent slide scars may be related to the mechanics of an adjacent larger slide. Field surveys along selected mountain ridges have recorded movements on the order of millimeters to centimeters per year (Savigny and Leir 1995). These movements are attributed to deep seated mass creep and/or mountain top sagging and may represent the early stages of landsliding (Hutchinson 1988, Savigny and Leir 1995). From remote sensing imagery landslides in this study area show little evidence of progressive movement and rarely exhibit a spectral signature that differs from the surrounding landscape.

More than 32 of the 58 landslides in the inventory are classified by Savigny (1995) as falls, topples, slumps, block slides, slides, flows and avalanches (Varnes 1978). All occur in bedrock except for one in Quaternary sediments. The remaining slides are unclassified. 68 % of the classified slides are rock slump or rock block slides. These types of movements involve shear displacement along one or more concave or near planar surfaces of weakness such as faults, joints, and bedding planes.

To summarize, the landslides in the inventory:

- 1) are large with volumes between 1 to > 500 million m<sup>3</sup>;
- 2) are predominantly prehistoric with subdued morphology obscured by uniform vegetation;
- 3) likely exhibit small progressive movements that are difficult to detect from remotely sensed imagery;
- 4) are located using morphological rather than spectral characteristics; and,
- 5) are mostly rock slump or rock block slides occurring along faults, joints, and bedding planes.

### 3.4 Morphological and Spectral Landslide Indicators from Airphotos

Traditional morphological indicators for landslides on airphotos include scarps, ground cracks, rupture surface scars, debris trains or lobes, bulges or depressions in slope profile, offset or dammed drainages, tonal variations, and contrasting vegetative patterns, and slope ponding (Rib and Liang. 1978). Utility of these indicators is restricted by the scale of the mapping and the characteristics of the

landslides. In this area unique indicators such as geological lineaments and lineament patterns prove to be more useful for locating bedrock controlled landslides.

The most useful indicators are morphological rather than spectral. Useful indicators include the presence of scarps, ground cracks, bulges and depressions, debris lobes, and offset or altered drainage courses. Slides in the study area are prehistoric, characterized by eroded scarps and subdued morphology obscured by mature alpine forest so contrasting vegetation patterns, tonal variations, and slope ponding are less reliable indicators. Large infrequent landslides rarely have anomalous vegetation and tonal patterns distinguishing them. Compare two rock avalanches in the inventory in Plates 3.1 and 3.2. Plate 3.1 is the 1965 Hope Slide, the most recent landslide in the inventory. The headscarp, source area, transportation and deposition zones exhibit abrupt spectral contrasts to the ground cover on the valley walls and floor. These properties are not common in this area. The Hope Slide is the only landslide in the inventory with contrasting spectral properties because it is a relatively new slide. It is easy to recognize in photographic and digital imagery by manual interpretation and automated methods. In complete contrast to the Hope Slide, but representing the majority of the slides in the inventory, is the Katz Slide in Plate 3.2. This slide may be the most recent of the dated slides in the inventory occurring approximately 3260 BP (Naumann and Savigny 1992). The headscarp, source area, transportation and deposition zones are obscured by mature vegetation. This slide, and others like it, are located by noticing morphological contrasts between the undulating debris and the flat valley floor rather than spectral contrasts.

Some landslides may be located by noticing changes in vegetation cover. In British Columbia abrupt changes in vegetation cover on mountain slopes are often attributed to regeneration in logging cut blocks, forest fire damage, or snow avalanche paths rather than the presence of a landslide. Additionally, movement rates on the order of centimeters per year (Savigny and Leir 1995) do not provide enough stress on vegetation to be detected reliably with infrared imagery (McKean *et al.* 1991). Slope ponding, identified by moist soil conditions and elongate ponds in depressions between antislope scarps, is best located with high resolution imagery.



Plate 3.1.      *The 1965 Hope Slide.*

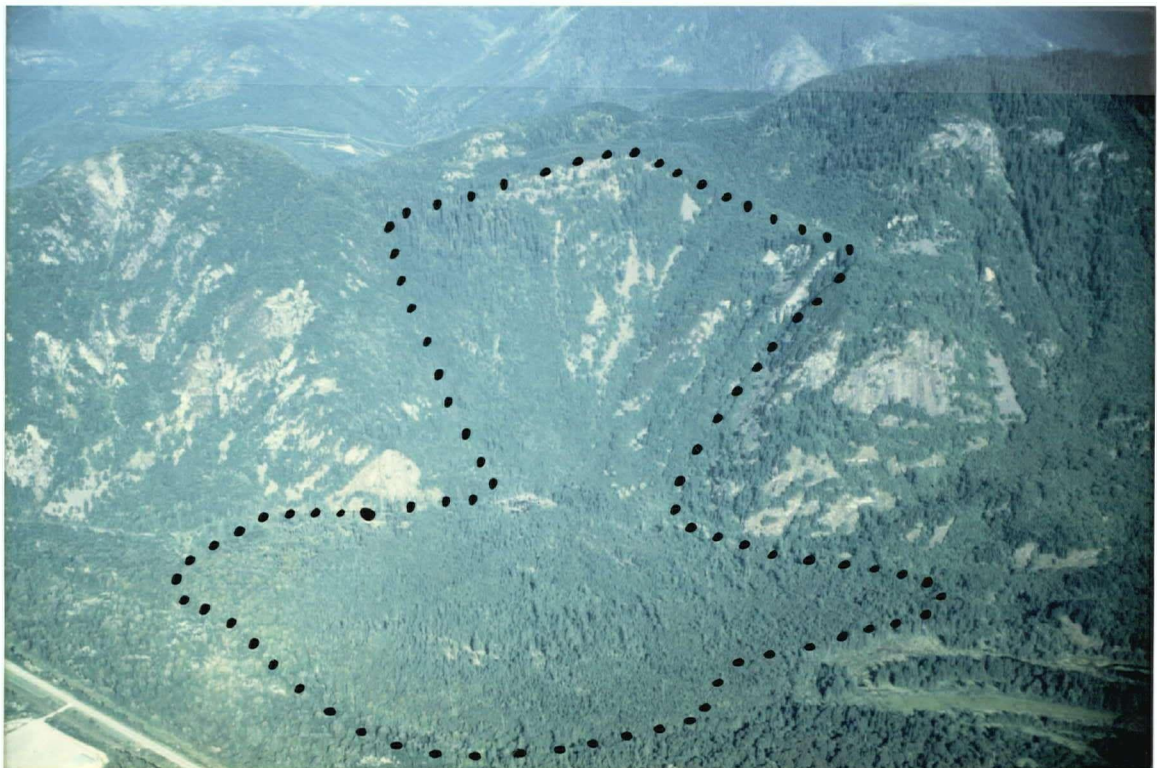


Plate 3.2.      *The prehistoric Katz Slide.*

Scarps, ground cracks, and depressions are often represented by lineaments. Lineaments are composite linear topographic, drainage, vegetation, moisture, and tonal alignments visible in remotely sensed imagery (Mollard 1988). In this study the terms fracture lineament, fracture trace (Lattman 1958), surface lineament, and photo lineament are used synonymously. Lineaments can be surface expressions of ground rupture associated with faulting, tectonic activity, glacial unloading, slope deformation and other forms of geological stress relief. Here most lineaments are seen in stereo imagery as single or multiple pervasive straight scarps or narrow depressions 0.5 m to tens of metres deep. Plate 3.3 is an example of a single lineament found near the headscarp of the Cheam Slide. It is associated with mountain top cracking that likely preceded catastrophic failure. Plate 3.4 is an example of a series of lineaments resulting from the deep seated creep on Cheekye Ridge near Squamish, British Columbia. Repeated glaciation erodes major structures into deep linear troughs which are kilometers long. The Hope and Yale faults seen in a digital elevation model (DEM) in Figure 3.2 are examples of this.

Failure surfaces, flanks, headscarps, antisllope scarps, tension cracks, and grabens often coincide with a particular orientation of lineament or lineament set. Locating the lineaments often leads to locating a landslide. Savigny (*pers. comm.*) often found landslide scars between conspicuous gaps in lineament trends. With exception of lineament/vegetation correlations (McKean *et al.* 1991, McFall and Singhroy 1989), stereo imagery or imagery sensitive to morphological change is required to find most lineaments.

### 3.5 Factors Affecting Landslide Distribution

Savigny (1995) proposed that, among other factors, the presence of regional faults, lineaments, plutonic contacts, carbonate, ultramafic, gabbro, and peltic rocks, and glacial erosion and unloading may control the location of large rock landslides. These spatial relationships are derived from airphoto interpretation, assessment of the inventory, and field observation. A GIS is used here to quantitatively examine the relationships between the proposed factors and landslide occurrence. The following is a summary of the correlations noted by Savigny.

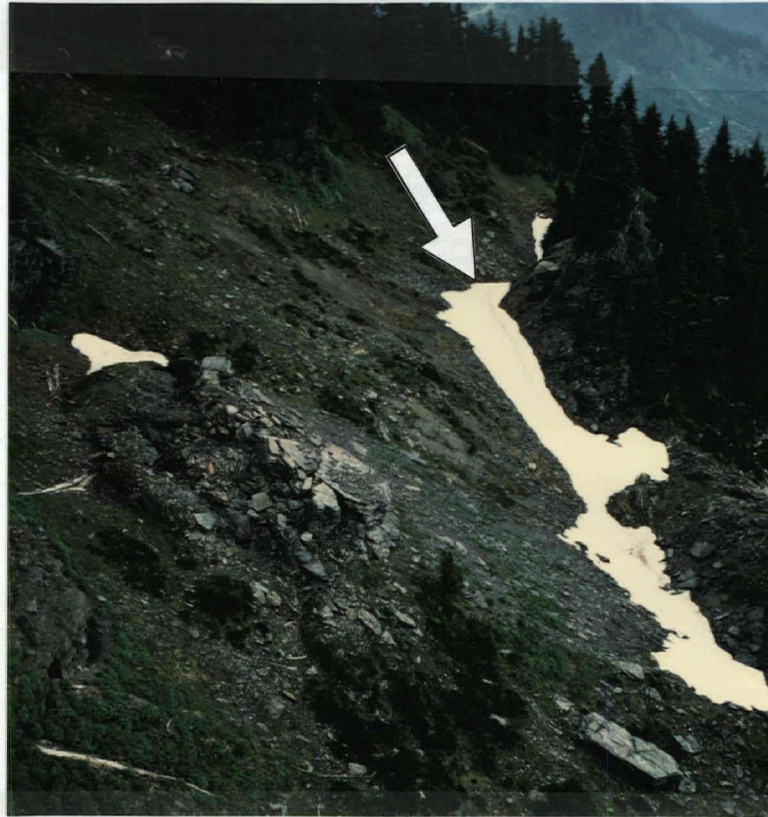


Plate 3.3. *Lineament located near the headscarp of the Cheam Slide.*

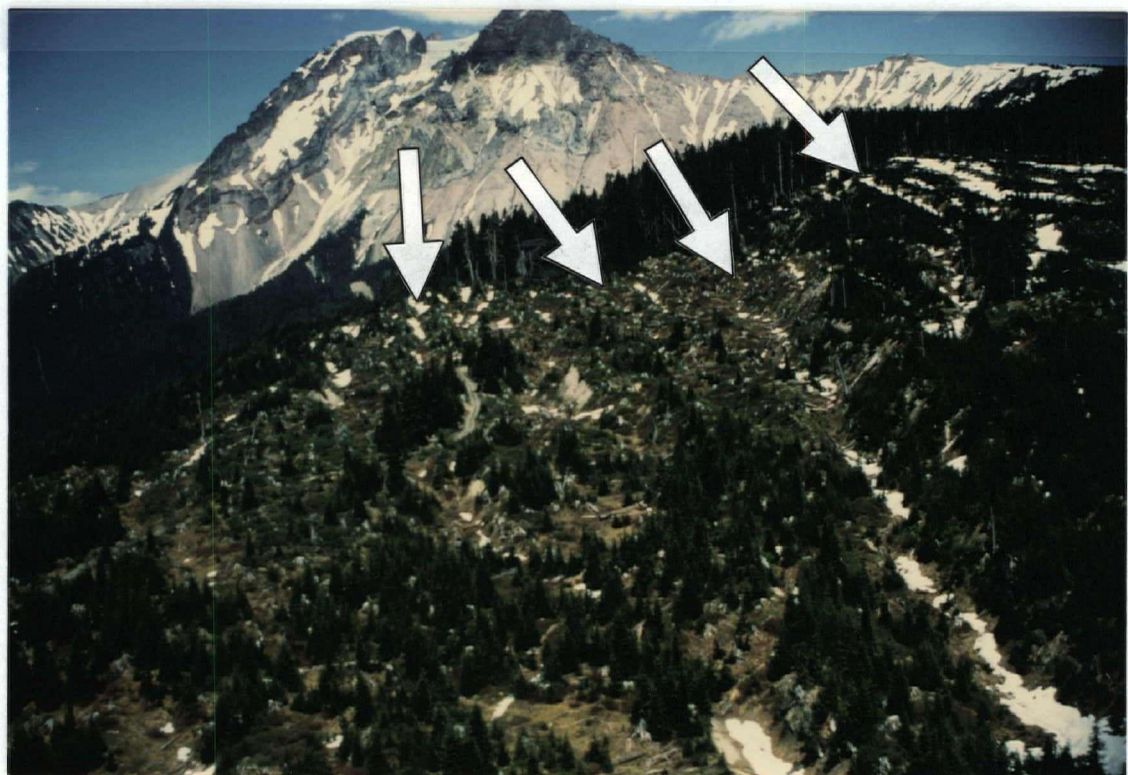
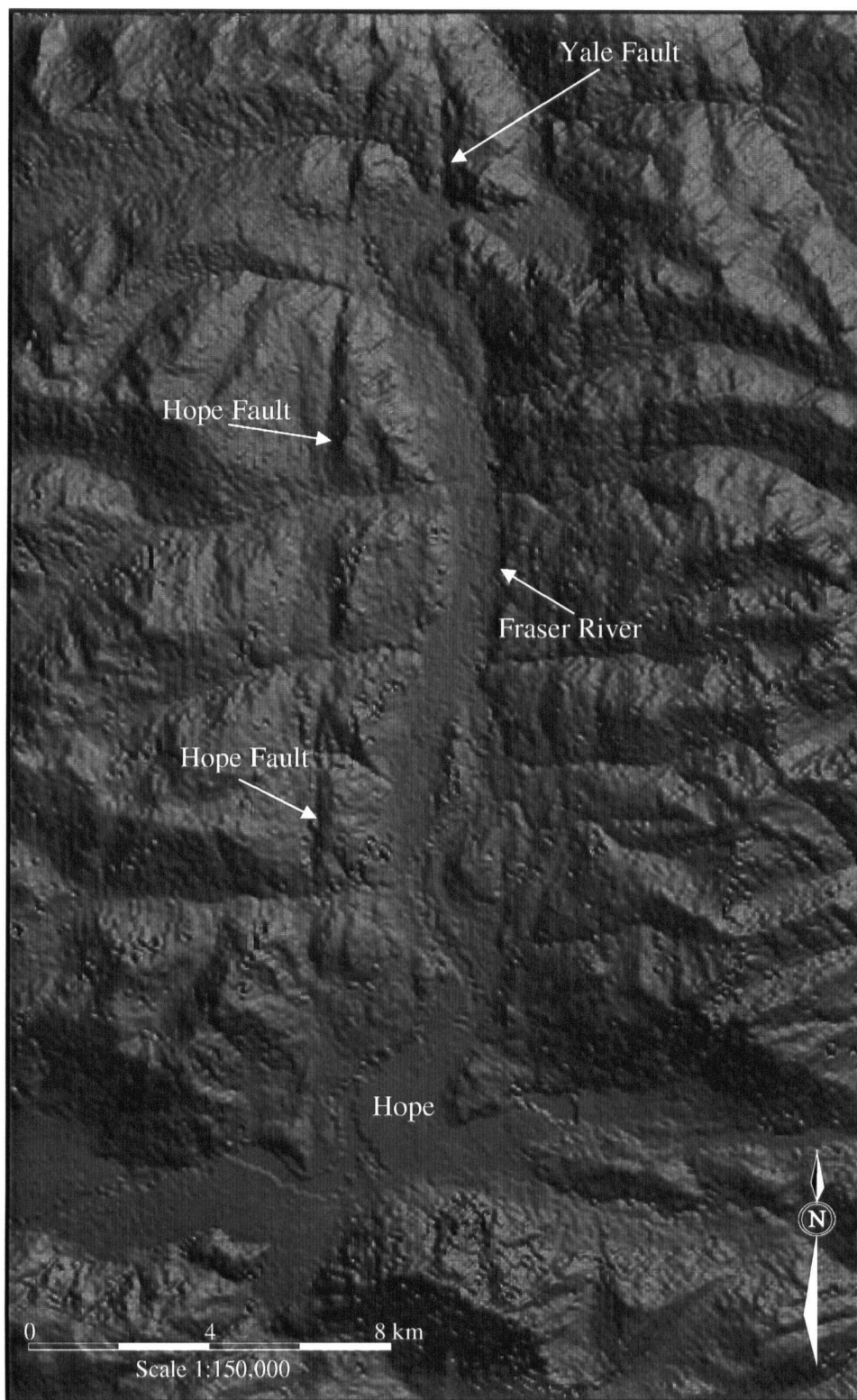


Plate 3.4. *A series of lineaments at Cheekye Ridge, Squamish, B.C.*



**Figure 3.2.** *The Hope Fault seen in BC TRIM DEM.*

1) Most landslides occur near north to north-northwest trending transcurrent faults, including the Hozameen, Ross Lake, Hope, Harrison faults. Large landslides are present along the northeast trending Vedder Fault trace. This spatial association with faults may be related to fracture density near the faults. Field evidence suggested that discontinuities near faults were more common and more closely spaced within one kilometer of the fault. Additionally, many lineaments, which are surface expressions of the discontinuities, often intersect and are truncated by landslide headscarps.

2) Approximately 70% of the landslides occur in the metasedimentary or metavolcanic rocks adjacent to plutons. No specific pendant formation shows a disproportionate frequency of landslide occurrence.

3) Deep erosion and oversteepened slopes and local isostatic recovery caused by repeated glaciation also contributes to the instability of the region. Linears of glaciotectionic origin are recognized in the area and one coincides with the apex of the 1965 Hope Slide headscarp.

4) Although difficult to prove, precipitation (Naumann 1990) and neotectonics (Everard 1994) are believed to be causative factors in some of the large landslides. Correlating historic precipitation and seismic data to prehistoric landslide occurrence is subjective at best. Human activity, although a well known factor in small landslides, has not caused any large landslides to date.

### 3.6 Conclusions

Landslides in the Hope study area are predominantly large (volume > 1 million m<sup>3</sup>) prehistoric rock slumps or rock block slides occurring along faults, joints, and bedding planes. They exhibit subdued morphology obscured by uniform vegetation and are best located in remotely sensed imagery using morphological rather than spectral characteristics. Morphological indicators used for landslide identification include scarps, ground cracks, bulges and depressions, hummocky debris, offset stream courses. Spectral indicators are less useful in this study area. They include vegetation contrast, tonal changes, and slope ponding. A high resolution remote sensing tool with stereo capability and/or sensitive to morphological change is required for proper landslide hazard mapping in this study area. Airborne

synthetic aperture radar (SAR) is a high resolution remote sensing tool that is sensitive to morphological change. The utility of SAR for landslide hazard mapping is compared to airphotos in Chapter 4.

Based on the airphoto inventory of landslides and lineaments, spatial relationships between regional faults, lineaments, plutonic contacts, and pendant rocks and landslide hazard occurrence have been proposed by Savigny (1995). These relationships will be quantitatively explored in Chapter 5 of this thesis. Precipitation, neotectonic, or land use data have not been included in this GIS study of landslide occurrence.

## CHAPTER 4

### Lineament and Landslide Hazard Mapping with Airborne SAR

#### 4.1 Introduction

In many parts of Canada airphotos are readily available at relatively low cost. Airphotos provide stereo capability and superior resolution and are excellent tools for lineament and landslide hazard mapping. If airphotos are not available, as is the case in countries with military restrictions, what alternate imagery should be used for lineament and landslide hazard mapping? How does this alternative imagery compare to airphotos? What additional or different information can the imagery provide when used in combination with airphotos?

In the Hope study area lineament and landslide hazard mapping by Savigny (1995) uses 1:50,000 scale black and white stereo airphotos. Lineament mapping uses both morphological and spectral contrasts in the image. The large prehistoric rock landslides are located and identified by observing subtle changes in spatial lineament patterns and geomorphology. In the Hope area, morphological rather than spectral contrasts play a larger role in mapping these types of hazards. Imagery that rely on spectral contrasts (i.e. Landsat MSS (Multispectral Scanner), Landsat TM (Thematic Mapper) or SPOT (Systeme Pour l'Observation de la Terre) are not the best tools for identifying these types of landslides. Rengers *et al.* (1992) found that stereo imagery is key for morphological landslide identification. Besides airphotos, SPOT and the new Canadian RADARSAT satellite can provide stereo imagery. Satellite and airborne SAR provide pseudo stereo capability because of low angle illumination geometry.

In addition to stereo, lineament and landslide mapping requires imagery with an optimum combination of scale and resolution. For accurate identification, the landslide should be at least 40 times larger than the pixel resolution (Rengers *et al.* 1992). For example the average landslide dimension in the

Hope study area is 1000 m with the smallest being 200 m. Depending on the contrast between the slide features and surrounding landscape, to identify the smallest slide the image resolution must be less than 5 m. Besides airphotos, only SAR and SPOT are close to this resolution.

Lineament mapping is also dependent on image scale and resolution. Shuman (1991) found that as image scale decreases lineament frequency decreases and lineament length increases exponentially. 10 m resolution SPOT images often reveal more lineaments than 30 m resolution Landsat (Knapp *et. al.* 1994). Manual lineament interpretation of hardcopy imagery can be performed most efficiently if  $R \times S = 0.1$  mm, where R is the ground resolution, S is the image scale, and the 0.1 mm corresponds to the limit of the human eye (Yamaguchi 1985). For example, the optimum scale for a 10 m resolution hardcopy SPOT or SAR scene is  $0.001/10 = 0.0001$  or 1:100,000. The equation represents a balance between image resolution and field of view. If the scale is too large then more images must be interpreted and the image may look blocky because individual pixels may be seen. If the scale is too small lineaments may be missed because the resolution is too small.

Note this relationship was derived using hardcopy images. For some applications images are interpreted directly from a computer screen. For these softcopy images, the resolution and dimensions of the computer monitor is the constraint rather than the human eye. For example, a 17" monitor (316 mm wide by 237 mm high) at 1024 x 768 resolution produces pixels 0.3 mm square. The equation now reads  $R \times S = 0.3$  mm and the optimum scale for a 10 m resolution SAR or SPOT image would be 1:33,000. Individual pixels could be clearly seen in an image larger than 1:33,000 scale and interpretation becomes too difficult. Smaller than 1:33,000 scale the image would be decimated and detail would be lost. On the other hand, a fewer number of images could be interpreted because the field of view is larger. A logical question now arises: In the example above, what scale of imagery smaller than 1:33,000 should be used to maximize lineament information but minimize interpretation time?

In conclusion, to efficiently map lineaments and landslides in the Hope Study area imagery must provide some form of stereo capability to capture the geomorphology and sufficiently low resolution (5 to 10 m pixels at the most) to identify the smallest landslides. Depending on the resolution of the imagery and the method of interpretation (hardcopy or softcopy) the optimal scale is between 1:33,000 and

1:100,000. To date only low resolution SAR or stereo SPOT are capable of providing stereo at resolutions less than 10 m. This research will compare the utility of SAR to airphotos for lineament and landslide mapping in the Hope study area.

#### 4.2 Introduction to Airborne SAR

SAR is an active remote system that uses microwave energy as a source for illuminating a target. Optical remote sensing data such as aerial photographs, Landsat (MSS and TM) and SPOT use the sun to illuminate ground targets. SAR platforms may be airborne or spaceborne. SAR imagery looks similar to black and white airphotos with a low sun angle but digitally provides very different data than the traditional optical data. Feder (1986) provided an interesting analogy to describe the principles of SAR. He wrote;

Radar is analogous to holding a flashlight over your right shoulder and illuminating an object held an arms length in your left hand. If the object is a mirror, it will be a specular reflector. That is, when held horizontally, the mirror will reflect energy away from you. As you progressively tilt the mirror to vertical, it will progressively reflect more energy back to you. The mirror contrasts with a piece of crumpled tissue, a diffuse reflector, which will return a large amount of energy to you regardless of the illuminating geometry.

Introductory discussions of SAR can be found in Lillesand and Kiefer (1994), Sabins (1987), and Feder (1986). Details and technical discussion can be found in the Radar Remote Sensing Training Manual by Werle (1992) and the Manual of Remote Sensing (Colwell 1983).

For given target aspect, the comparison of return SAR energy permits us to interpret the nature of the target. The factors that determine the reflectivity of a target are: 1) the incidence angle between the radar beam and the sloping ground; 2) the target surface roughness, which is a function of the radar wavelength - the rougher the surface the more energy is reflected; 3) target moisture - moist targets exhibit high reflectivity; and 4) the look direction - targets perpendicular to the look direction (parallel to the flight direction) exhibit higher reflectivity.

The most important radar parameters for lineament mapping are: 1) look direction, as it will determine the preferential enhancement of the terrain; 2) incidence angle, which affects the degree of topographic enhancement; 3) spatial resolution, which affects the amount of fine structural detail that

can be seen. For maximum lineament enhancement the radar look direction should be orientated perpendicular ( $\pm 20^\circ$ ) to the primary grain (tectonic or topographic) of the terrain. This  $40^\circ$  wide zone where linear features are easier to detect is called the enhancement zone. Linear features parallel to ( $\pm 20^\circ$ ) the SAR look direction are more subtle and difficult to detect. (Harris 1984). This  $40^\circ$  zone is called the suppression zone. The effects of the enhancement and suppression zones on SAR lineament mapping are demonstrated in Section 4.8. HH polarization provides marginally more geological information than VV polarization (Paradella *et al.* 1994).

Advantages of SAR include an all weather capability, limited vegetation and soil penetration, enhancement of subtle topographic features, and relatively high resolution. The longer SAR wavelengths (1 to 10 cm) permit penetration of clouds and, under certain conditions, some vegetation and soil cover. The low illumination angle enhances topographic detail. Pixel resolutions to 6 m are common with airborne platforms while satellites can provide pixel resolutions down to 10 m. It is the latter two advantages that make SAR, particularly airborne SAR, useful for geological investigation.

#### 4.3 SAR Applications in Geology

Satellite and airborne SAR applications in geology (Singhroy *et al.* 1993, 1994, Evans 1992, Werle 1992) include geological mapping in the Northwest Territories (Gibbins and Slaney 1991) and the Precambrian Shield (Mussakowski *et al.* 1991), surficial geology mapping in glaciated terrain (Kenny *et al.* 1994, Singhroy *et al.* 1992), and structural mapping for mineral exploration in Nova Scotia (Harris 1991) and hydrocarbon exploration in the western Canadian sedimentary basin (Misra *et al.* 1991), northeast British Columbia (Posehn and Genereux 1991), and Papua New Guinea (Dekker *et al.* 1989).

Geologic hazard studies involving SAR are not common, landslide investigations are rare. Integrated C-band SAR and SPOT images were used to correlate seismic epicenters to regional geologic structure and topography near the North Nahanni River in the northeast Canadian Cordillera of the Northwest Territories (Moon *et al.* 1991). Neotectonic mapping in southeast Spain is improved with integrated ERS-1 SAR with Landsat TM (Mason *et al.* 1994). Lineaments visible from SAR imagery provide essential clues to the tectonic setting of the 1988 Saguenay earthquake and the nearby

Charlevoix-Kamouraska seismic zone in Quebec Canada (Roy *et al.* 1993). X-band Side-Looking Radar (X-SLAR), traditional airphoto and color infrared (CIR) images were used to investigate and interpret bedrock landslides, rockfalls, and rock mass deformation in the area of the Yangtze Gorges in China (Yong and Qinghua 1990).

Lineament mapping comparisons between SAR and Landsat imagery are relatively common. Lineament mapping with Landsat MSS (80 m resolution) and Seasat-SAR (25 m resolution) in central Nova Scotia by Harris (1984) concluded that Seasat SAR provided the most lineament information in terms of absolute numbers. In general, more detailed structural patterns are mapped from the remotely sensed imagery than that which exists on the regional geology maps (Harris 1984). Preliminary lineament mapping in the Appalachian Plateau with Landsat TM (30 m resolution) and SLAR indicate that for a given amount of observation time SLAR shows more lineaments and longer lineaments than TM (Shuman 1991). Near Sudbury Ontario more lineaments were derived from 6 m resolution C-SAR than Landsat TM, but their average length is shorter (Premmanee 1989). The only published case where Landsat TM found more and longer lineaments than Seasat SAR is in the Cobequid Highlands of Nova Scotia. (Harris *et al.* 1987). Here Landsat was useful in delineating lineaments highlighted by changes in vegetation pattern. From these experiments SAR appears to be a better tool than Landsat for lineament mapping.

Comparative analyses between SAR and other imagery are scarce. Shuman (1991) compared lineament length and frequency to image scale for airphotos, Landsat TM and SAR but the images were all at different scales. For interpretive work in mountainous relief Kotyukh and Monakhov (1990) found X-band SAR to be more graphic than aerial photographs but aerial photographs are slightly better than radar in broad-leaved forests. In Newfoundland, Graham and Grant (1991) found that morainal topography is seen much more clearly in SAR than on airphotos, allowing hummocky and ribbed moraine to be readily mapped. For these reasons airborne SAR may reveal hummocky landslide debris better than airphotos at similar scale. There are no published studies that specifically evaluate the utility of SAR for landslide hazard mapping. Additionally, most geological SAR studies, with the exception of Moon *et al.* (1991) and Dekker *et al.* (1989) have occurred in physiographies that are favorable to SAR -

low to moderate rolling topography with moderate vegetation cover. This SAR study is one of the first in high alpine mountainous terrain.

#### 4.4 Scope

The aims of this research are to demonstrate the use and evaluate the utility of airborne SAR for lineament and landslide hazard mapping. To evaluate the utility of SAR, the results of the lineament landslide mapping is compared to 1:50,000 black and white airphotos. Firstly lineaments derived from SAR and airphotos are compared using maps of lineament location and histograms of lineament length and orientation. Secondly, the relationships between image scale on lineament length and frequency are quantified for SAR. Finally three different landslide types are mapped using SAR and airphotos and the results are qualitatively compared.

#### 4.5 Chilliwack SAR Data and Study Site

Airborne C-band ( $\lambda=5.66$  cm) HH polarization SAR (Livingstone *et al.* 1987) was acquired by the Canada Centre for Remote Sensing (CCRS) along a NE/SW flight line on August 7, 1993. The data were collected in narrow mode, providing an 18 km wide swath with pixel spacing of 3.9 m in the azimuth and 4.0 m in the range direction. The radar look direction was from the north-west, and the depression angles range from  $45^\circ$  at the near edge to  $14^\circ$  at the far edge. Figure 4.1 is a diagram of the Chilliwack SAR viewing geometry. Signal data were processed in real-time to seven looks and converted from slant to ground range, producing data with a nominal resolution of 6 m. Appendix II contains the Chilliwack SAR and Convair 580 aircraft flight parameters.

The Chilliwack SAR image (Figure 4.2), a 18 km by 48 km area totaling  $875 \text{ km}^2$  (87500 Ha.), covers the steep mountainous terrain of the North Cascade Mountains and the flat rural urban areas of the lower Fraser Valley. The mountains on the southeast side of the Fraser valley between Hunter Creek and the Chilliwack River were selected for the Chilliwack SAR study site. It is well illuminated and is representative of the physiography and geology of the inventory area and, in general, southwestern

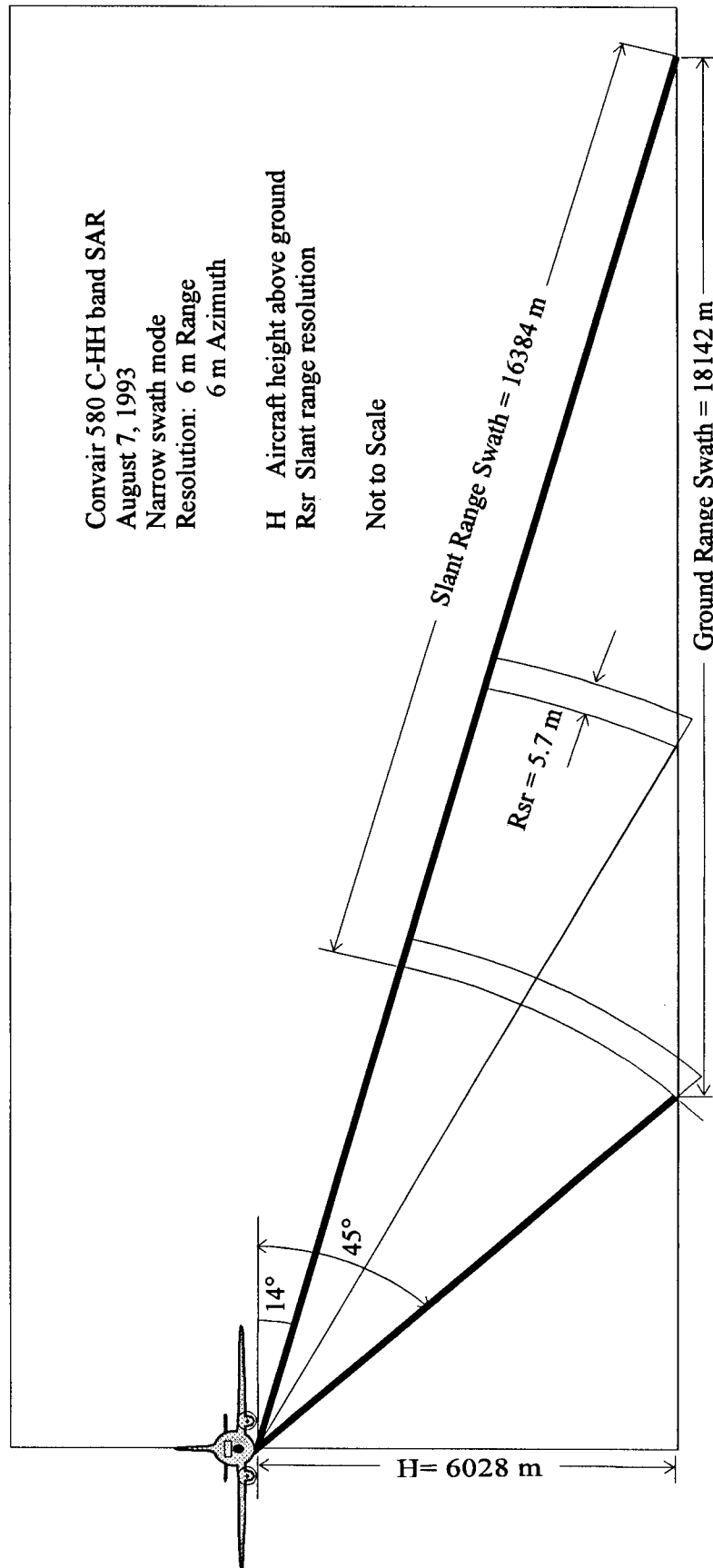


Figure 4.1. Chilliwack SAR viewing geometry.

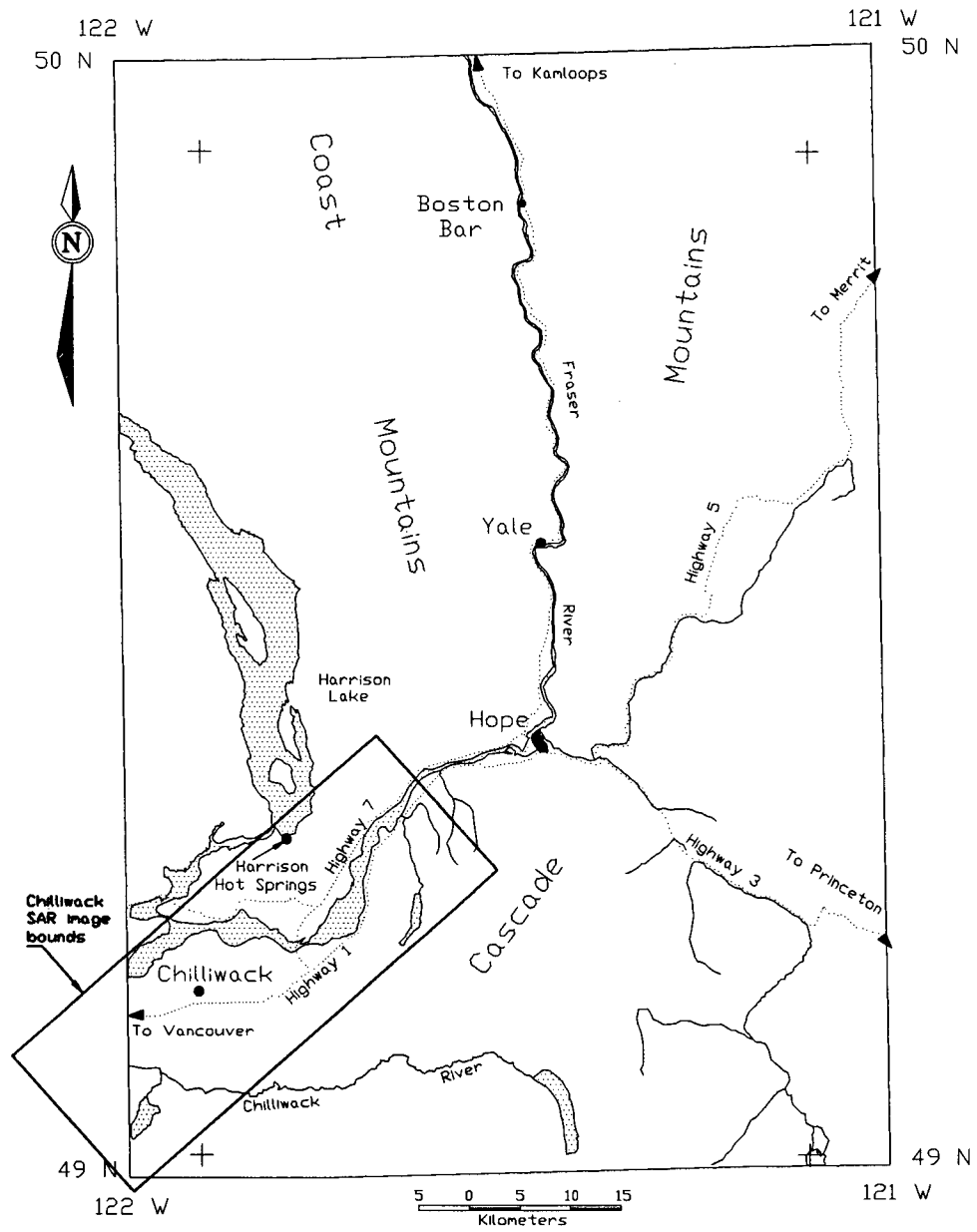


Figure 4.2. Chilliwack SAR image in relation to the Hope study area.

British Columbia. Figure 4.3 shows the locations of five different areas of mass wasting in the Chilliwack SAR; the Wahleach hazard, the Popkum Slide, the Cheam Slide, a north debris cone, and a south debris cone. These hazards are used to evaluate the mapping capability of SAR in Sections 4.9 and 4.10. Wahleach is an example of a hazard involving non-catastrophic movement manifested in subtle lineaments rather than well defined source, transportation, and deposition zones. The Popkum and Cheam slides are large prehistoric landslides with defined deposition zones. The debris cones north of the Popkum Slide and south of Cheam Slide have definable source, transportation and deposition zones.

The Wahleach hydroelectric development (Moore *et al.* 1992) is located 12 km northwest of Chilliwack adjacent to the Trans Canada Highway (Fig. 4.3). Water flows from a reservoir at Wahleach Lake through a steel lined tunnel and inclined shaft to a power house adjacent to the highway. The tunnel is excavated in massive to highly fractured granodiorite. Subvertical joints strike parallel and perpendicular to the slope trend and a third set dips 40° subparallel to the slope. Subvertical shear zones strike parallel to slope trend and are more widely spaced than joints. Thorough investigations indicate that no extensive shear zones are oriented in a direction conducive to downslope sliding. The ridge in which the tunnel is located is crossed by lineaments. Trees growing in these linear depressions indicate a history of downslope movement over several hundred years. In January 1989 a 15 mm wide tension crack and eight compressional zones were found in the steel lining of the tunnel. Using creep movements recorded at surface from 1989 to 1990, numerical modelling studies by Savigny and Rinne (1991) suggested that these deformations were caused by downslope creep of a toppling style failure involving up to 60 million m<sup>3</sup> of rock. Moore *et al.* (1992) concluded that;

“the lack of throughgoing adversely oriented discontinuities, the long history of diffuse, slow movements and the insensitivity of these movements to groundwater, indicate that the present movements will continue for considerable time and that a large rockslide is not imminent”.

The Popkum Slide (Cavers 1992) is approximately 6 km southwest of Wahleach (Fig. 4.3). The hummocky deposition zone located on the northwest side of the Trans Canada Highway contrasts with the surrounding flat floodplain of the Fraser River. Preliminary field investigations suggests a rock avalanche originated from the adjacent slopes of Mount Cheam and deposited massive till-like material

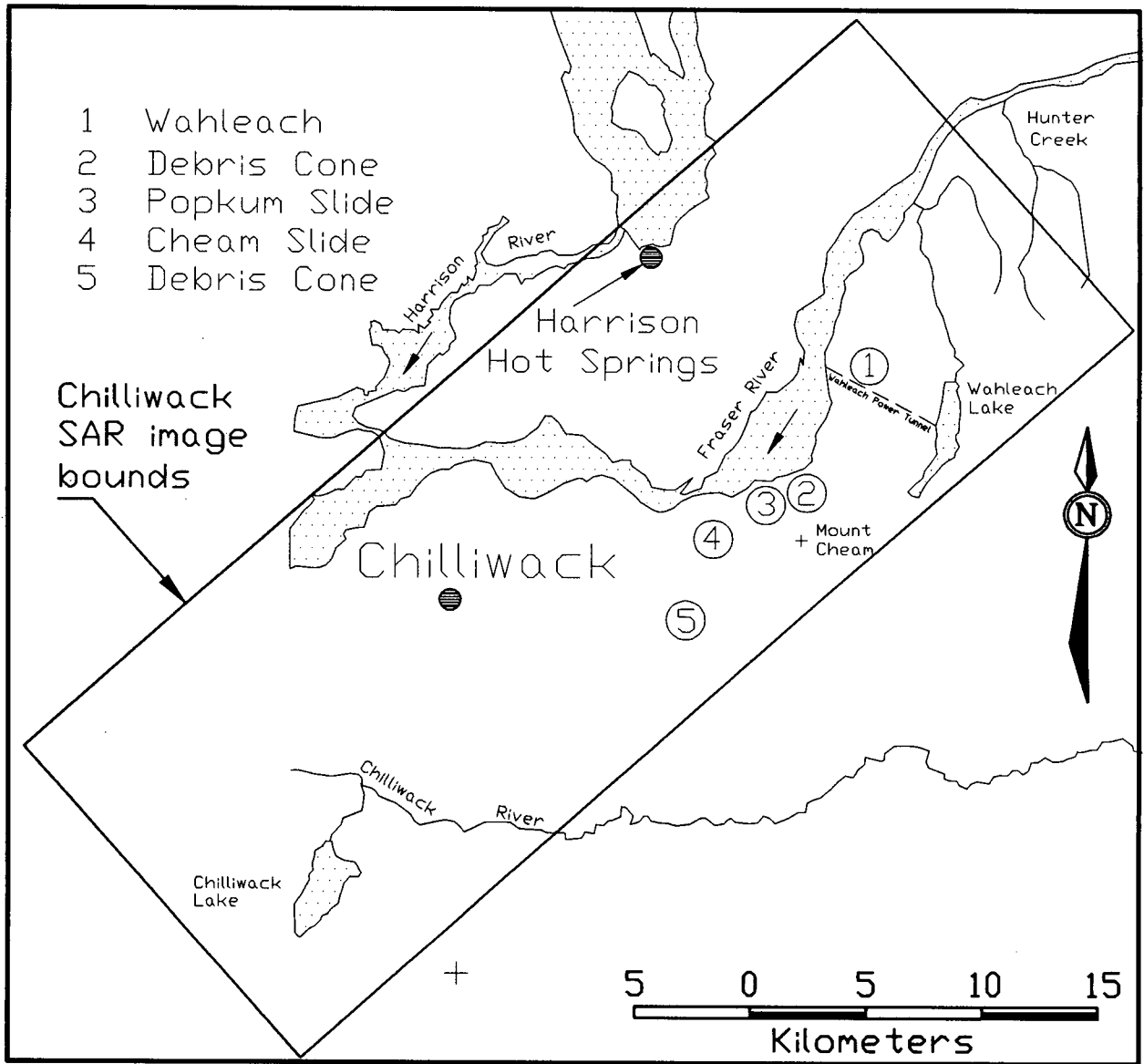


**Figure 4.3.** SAR study area including five landslide hazards.

consisting of a heterogeneous mixture of silt, sand, gravel and cobbles. (Cavers 1992). A large graben approximately 20 to 40 m wide and 16 m deep, associated cracks, holes and evidence of toppling are evident near the summit of Mount Cheam (Cavers 1992). The relationship between the debris and the graben, if any, is unclear.

The Cheam Slide (Naumann 1990) is a mid-Holocene rock avalanche located on the southeast side of the Fraser River 15 km east of Chilliwack (Fig. 4.3). Of the five slope hazards in the SAR imagery, the Cheam Slide provides the best example of a prehistoric source, transportation and deposition zone. Similar to Popkum Slide, the contrasting arcuate hummocky debris immediately north of the Trans Canada highway is the most notable feature. The rubble and diamicton overlying thick Fraser Valley sand and gravel was likely deposited between 4500 to 5000 years B.P. in a post glacial environment (Naumann 1990). The source zone, identified by Naumann from airphoto interpretation and field investigation, is a large asymmetrical wedge originating 400 m above the debris on an unnamed mountain immediately southwest of Mt. Cheam. Naumann proposed that the wedge is bounded by a thrust fault ( $340^{\circ}/21^{\circ}$ ) and a joint set ( $100^{\circ}/49^{\circ}$ ). The source area is difficult to discern as it is obscured by vegetation and years of erosion. From airphotos Savigny (1995) noted two prominent lineaments intersecting near the toe of the slide that contribute to a precipitous, glacial oversteepened lower slope. Additionally, sackungen immediately northeast of the wedge scarp and across the mountain top are interpreted as mountain deformation.

The debris cones north of Popkum Slide and south of Cheam Slide are not components of large rock landslides but are included in the SAR mapping evaluation because the cone morphology is representative of landslide debris. Also, debris cones and the processes that create them are very common in mountainous terrain and should not be overlooked.

#### 4.6 SAR Image Processing and Enhancement

A number of data processing and enhancement tasks (Singhroy *et al.* 1994) were carried out in order to improve the radiometric quality of the imagery and geometrically correct the SAR data. Visible antenna pattern effects required across-track radiometric smoothing using a fourth order polynomial fit

and speckle reduction was achieved using a single pass 7 by 7 Lee adaptive filter (PCI 1992). The Chilliwack SAR was geocoded (PCI 1992, Toutin *et al.* 1992) to Universal Transverse Mercator (UTM) coordinates using 1:20,000 scale British Columbia Terrain Resource Inventory Map (TRIM) digital data and DEM. The SAR and DEM were resampled to 10 m pixel spacing using 218 ground control points (GCPs) and a second order cubic convolution transformation. The Root Mean Square (RMS) error for the SAR was 2.69 pixels (15.97 m) and 3.71 lines (14.45 m), and for the DEM was 0.43 (24 m). This error is acceptable for mapping lineaments and slide features at 1:20,000 scale and smaller. A linear contrast stretch was used to improve the visual contrast of the lineaments and landslide features. Geocoding of the SAR using the B.C. TRIM DTM and DEM requires approximately 7 days to complete.

#### 4.7 Lineament Mapping Methodology

Lineaments are manually mapped by the author using 1:50,000 scale black and white stereo airphotos, geocoded softcopy 1:20,000, 1:50,000 and 1:80,000 Chilliwack SAR images, and techniques adapted from Lattman (1958), Wheeler and Wise (1983), and Mollard (1988). This mapping program has several objectives: 1) consistent identification of lineament features; 2) elimination of non-geologic lineament features; 3) determination of the location, length, and trend of each lineament; 4) collection of lineament data in digital format.

Airphoto stereo pairs in the Chilliwack study area are interpreted for 20 minutes and lineaments drawn with a mouse on screen using the geocoded SAR image as background reference. For the SAR interpretation, an enhanced SAR image and a BC DTM vector overlay are viewed simultaneously on screen for a maximum of 20 minutes. Lineaments are identified and drawn on-screen as vectors using a mouse. A 1:20,000 scale DTM vector overlay of paved roads, gravel roads, cutlines, railways, bridges, trails, pipelines, powerlines, hydrology, buildings, clearcuts, and other anthropogenic features facilitates the delineation the non-geologic lineament features.

The final lineament vector layers are exported to a spreadsheet and GIS for statistical and spatial analysis. Lineament trends are calculated using the vector endpoint coordinates and the program

TREND (Leir 1994) and lineament lengths are determined using the AREA module in the IDRISI (Eastman 1993) GIS software.

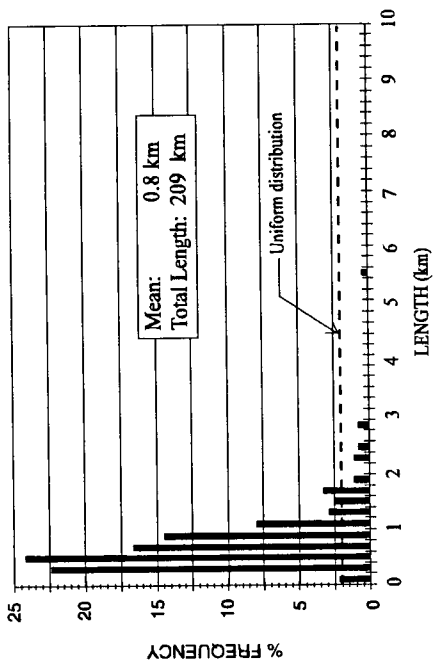
#### 4.8 Lineament Mapping Results

Histograms of lineament frequency vs. length (Fig. 4.4), and frequency vs. trend (Fig. 4.6) compare lineaments located from 1:20,000, 1:50,000 and 1:80,000 scale SAR images to those located with 1:50,000 scale airphotos. Four histograms are shown in each figure; (a) 197 lineaments located with 1:50,000 scale airphotos; (b) 278 lineaments located with 1:20,000 scale SAR; (c) 165 lineaments located with 1:50,000 scale SAR image, and; (d) 135 lineaments located with 1:80,000 scale SAR image. The horizontal dashed lines at 2% (Fig. 4.4) and 3% (Fig. 4.6) normalized frequency represent a uniform distribution of lineaments.

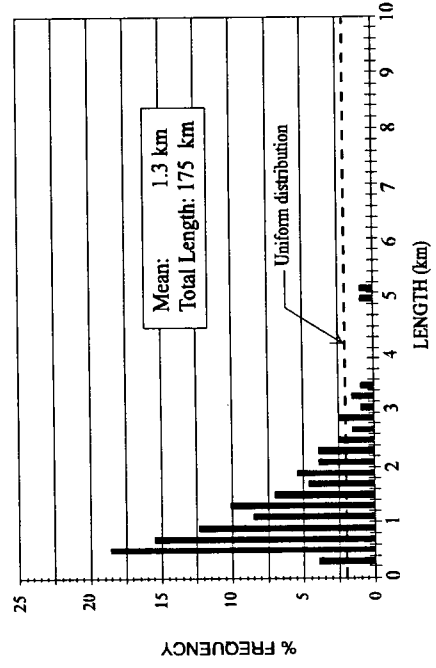
Figure 4.4 demonstrates that all three scales of SAR imagery reveal lineaments similar in length to airphoto lineaments. Lineaments from airphotos and SAR range from 0.5 to 3.0 km long and average 1 km. Generally, as SAR scale increases, average lineament length decreases and frequency of occurrence increases. For example, 1:20,000 scale SAR lineaments on average are shorter and are more frequent than 1:80,000 scale lineaments. This relationship is observed by Shuman (1991) for airphoto lineaments in the Appalachian Mountains. Figure 4.5 shows the inverse relationship between frequency and scale and the proportionate relationship between length and scale. Chilliwack SAR lineament data follow these relationships but are less sensitive to image scale than the Appalachian airphoto lineaments.

Lineament trends derived from airphotos exhibit two distinct trends at 010° to 055° and 155° to 160° with corresponding maxima at 040° and 155° (Fig. 4.6a). The Chilliwack SAR, with a look direction of 140°, has a lineament enhancement zone between 030° and 070° and a suppression zone between 120° and 160° respectively (Fig. 4.6b, c, and d). Accordingly, lineaments with trends perpendicular  $\pm 20^\circ$  are within the enhancement zone and are easier to detect while lineament trends parallel to the look direction  $\pm 20^\circ$  are within a suppression zone and are difficult to detect.

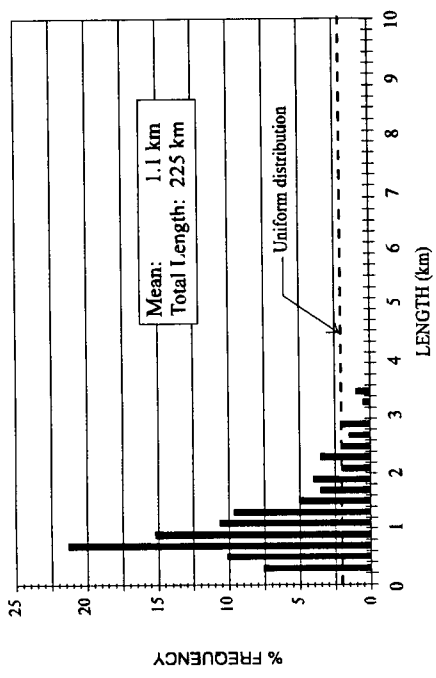
Figures 4.6b, c, and d demonstrate that, in general, the three scales of SAR imagery detect the two distinct airphoto trends and their corresponding maxima. Distinct SAR trends include 010° to 050°



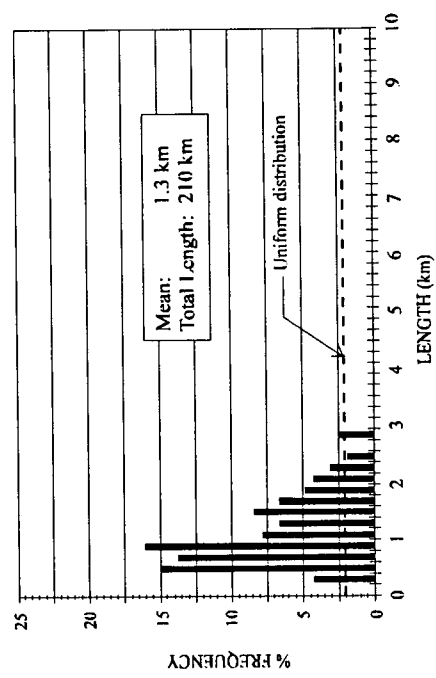
(b) 278 lineaments located with 1:20,000 scale SAR.



(d) 135 lineaments located with 1:80,000 scale SAR.

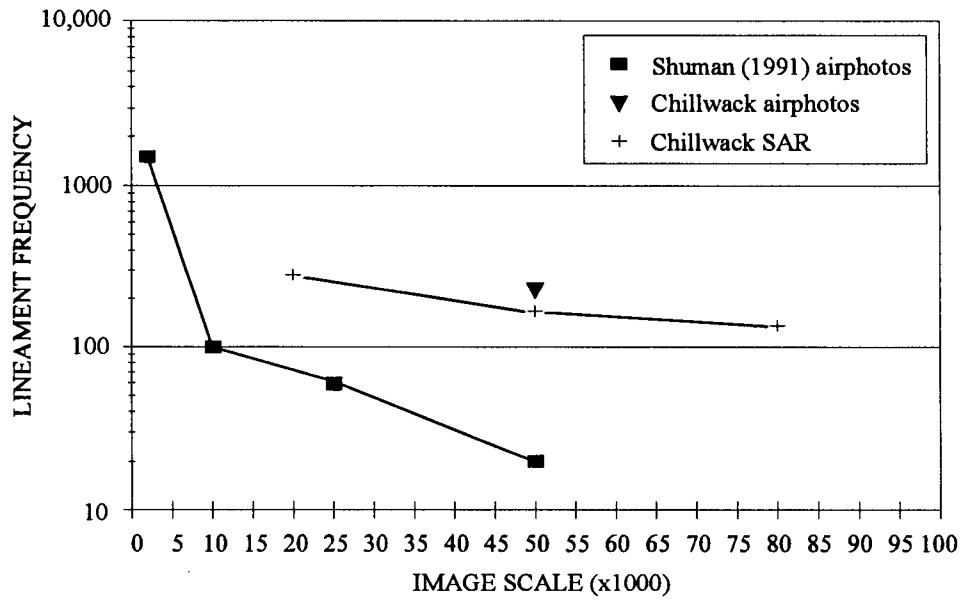


(a) 197 lineaments located with 1:50,000 scale airphotos.

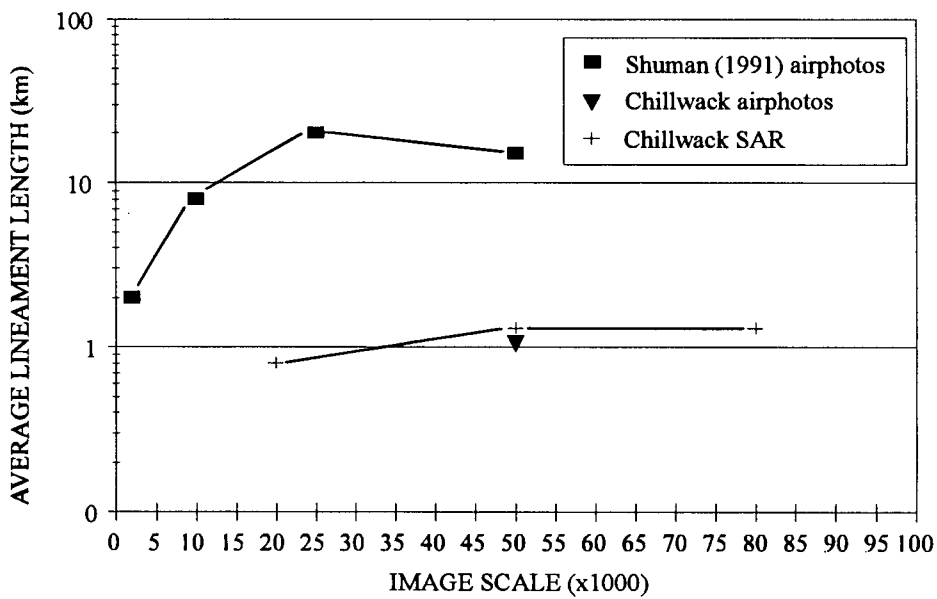


(c) 165 lineaments located with 1:50,000 scale SAR.

Figure 4.4. Histograms of lineament frequency vs. length.

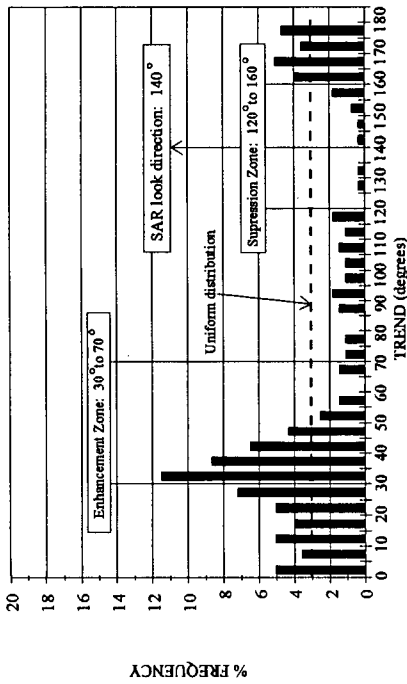


(a) Lineament frequency vs. image scale.

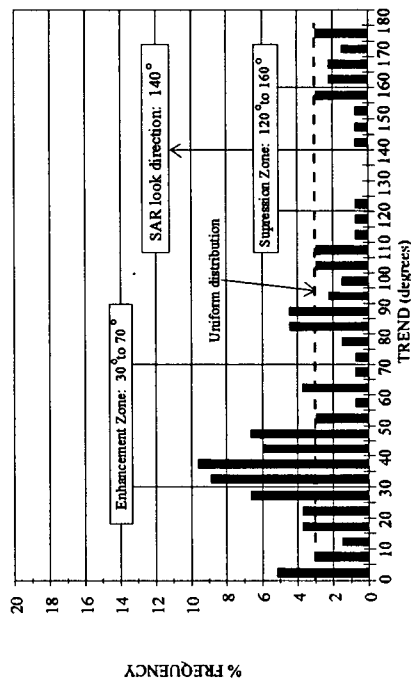


(b) Average lineament length vs. image scale.

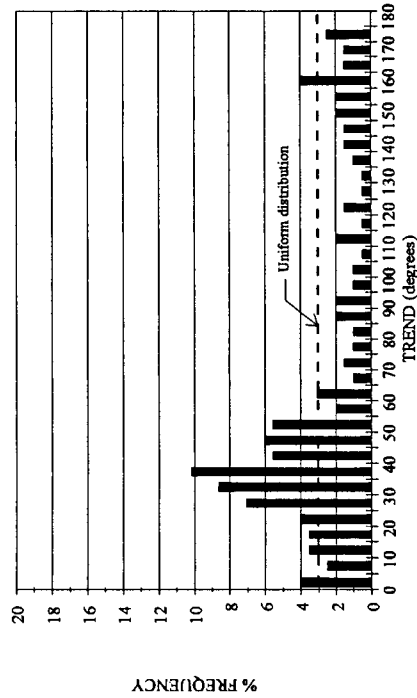
Figure 4.5. Observed average lineament frequency and length vs. image scale for Appalachian airphotos lineaments (Shuman 1991), Chillwack airphoto lineaments, and Chillwack SAR lineaments.



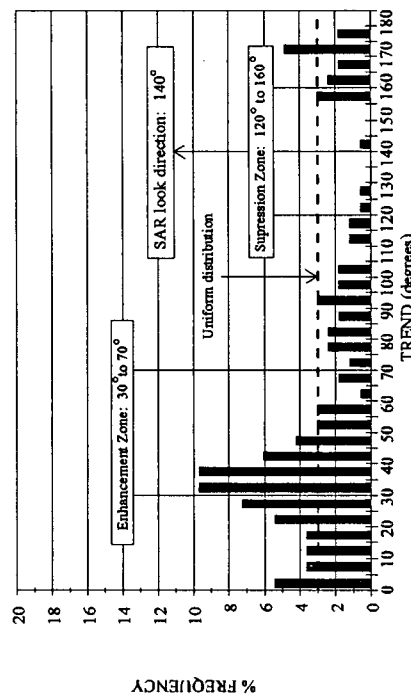
(a) 197 lineaments located with 1:50,000 scale airphotos.



(b) 278 lineaments located with 1:20,000 scale SAR



(c) 165 lineaments located with 1:50,000 scale SAR



(d) 135 lineaments located with 1:80,000 scale SAR.

Figure 4.6. Histograms of lineament frequency vs. trend.

and 160° to 180° with maxima around 040° and 170° respectively. In all scales SAR highlights lineaments trending 000° to 005°, a lineament trend not recognized in the airphotos. 1:80,000 SAR has detected lineaments around 085° but has failed to locate the 160° to 180° zone.

Using the airphoto lineament data base as an experimental control, the SAR evaluation focuses on how well SAR locates the airphoto lineaments. Table 4.1 lists the total number, total length, and average length of airphoto lineaments located with SAR imagery. At best SAR located 77 of 197 (39%)

	Lineaments located with airphotos	Airphoto lineaments located with SAR		
		1:20,000	1:50,000	1:80,000
Image Scale	1:50,000	1:20,000	1:50,000	1:80,000
Total Number	197 (100%)	76 (39%)	77 (39%)	67 (34%)
Total Length (km)	225(100%)	98 (44%)	109 (48%)	97 (43%)
Average Length (km)	1.1	1.3	1.4	1.4

Table 4.1. *Airphoto lineaments located with SAR.*

airphoto lineaments which is 49% of the total airphoto lineament length. This percentage is low considering Figures 4.4 and 4.6 show that SAR lineament length and orientations match, in general, with the airphoto lineament length and trend. These facts imply that SAR is locating other lineaments with lengths and trends similar to airphoto lineaments. On the other hand, 88 of 165 (53%) SAR lineaments did not match with any airphoto lineaments. This means that just over half of the SAR lineaments contribute additional structural information about the Chilliwack area.

Figure 4.7 shows the location of lineaments found with 1:50,000 scale airphotos and SAR, airphotos only, and SAR only. Inspection of Figure 4.7 reveals that SAR has located most of the long airphoto lineaments. Shorter airphoto lineaments are difficult to see in SAR imagery because SAR has lower resolution than airphotos. Additionally, SAR imagery has difficulty highlighting lineaments that are characterized by smooth or wide depressions, troughs or valleys. Lineaments that are characterized

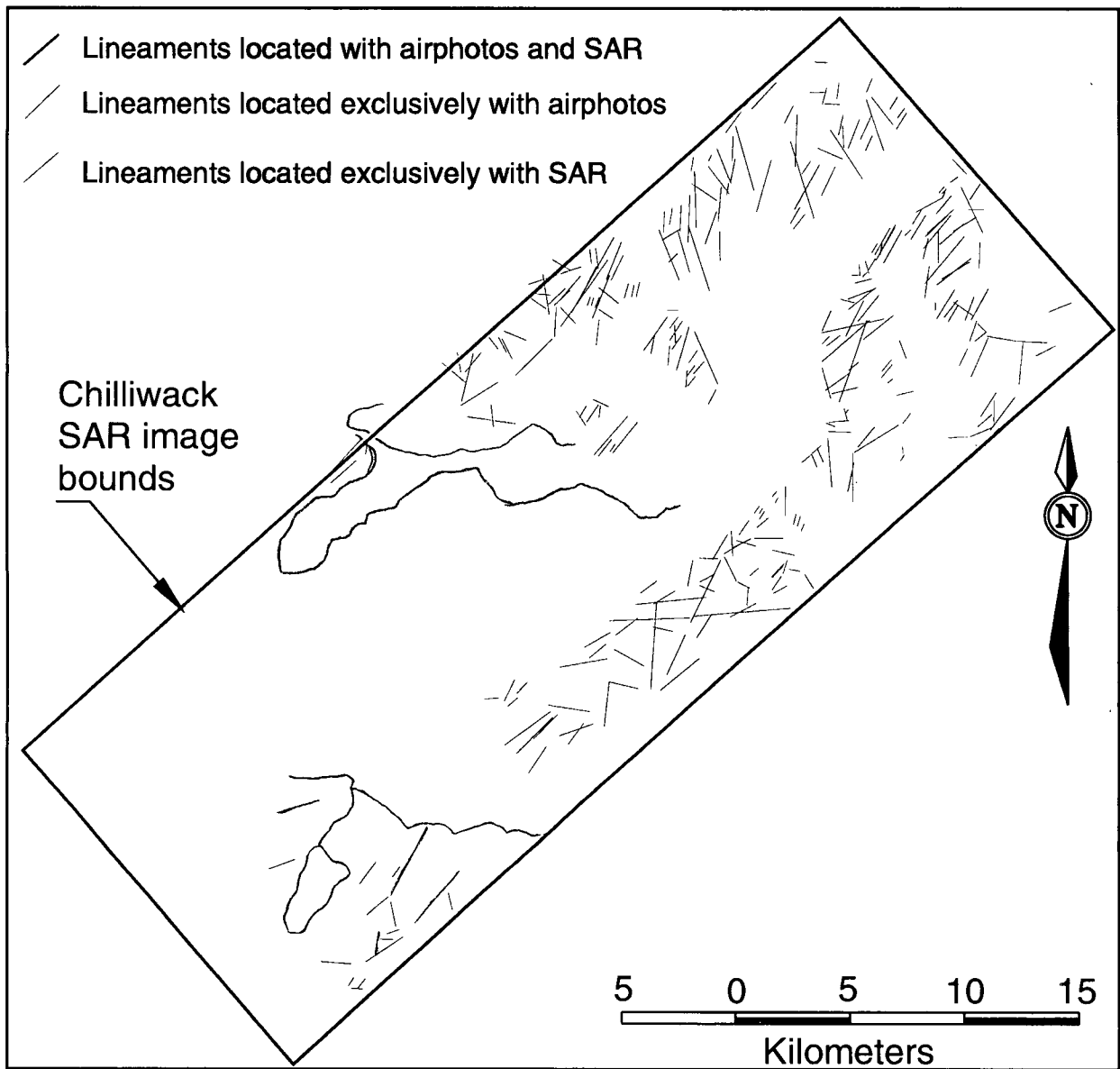


**Figure 4.7.** Lineaments located with 1:50,000 scale airphotos and SAR, airphotos only, and SAR only.

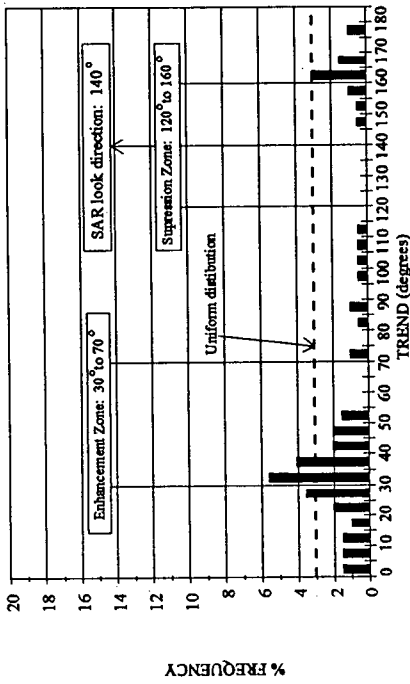
by abrupt changes in morphology, like antislope scarps or terraces, are easier to see in a SAR image. Finally, despite missing some of the shorter airphoto lineaments, many of the airphoto lineaments found with SAR could be lengthened in the SAR image.

Figure 4.8 shows histograms of lineament frequency vs. trend for airphoto lineaments located with SAR imagery. The purpose of this figure is to determine which airphoto lineament trends, if any, SAR preferentially locates. One would expect that most of the airphoto lineaments within the enhancement zone between 030° and 070° would be located. This is not the case. In fact a disproportionate number of airphoto lineaments within the enhancement zone were not located by SAR. The zone in which SAR missed the most airphoto lineaments is between 035° and 040°.

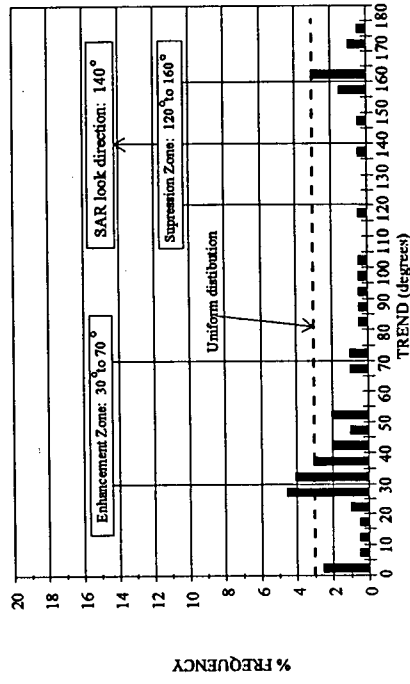
The issue of adding the SAR lineament data interpreted by the author to the Savigny (1995) landslide and lineament data base for GIS analysis in Chapter 6 will now be discussed. Comparison of the author's Chilliwack airphoto and SAR lineaments to Chilliwack airphoto lineaments interpreted by Savigny (1995) are presented below in Table 4.2. This table lists lineament frequency, total length, average length, and average trend. The Savigny (1995) lineaments are, on average, longer and trend

	Savigny (1995) airphoto lineaments	Airphoto lineaments	SAR lineaments
Image Scale	1:50,000	1:50,000	1:50,000
Total Number	108	197	165
Total Length (km)	248	225	210
Average Length (km)	2.3	1.1	1.3
Average Trend	81°	67°	63°

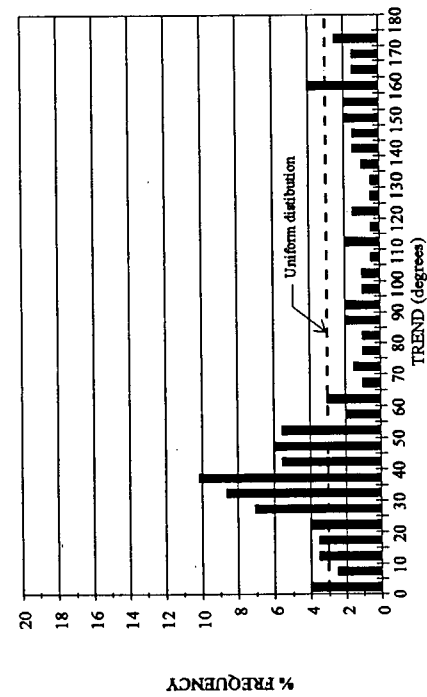
Table 4.2. *Chilliwack lineament data from Savigny (1995) and from this study.*



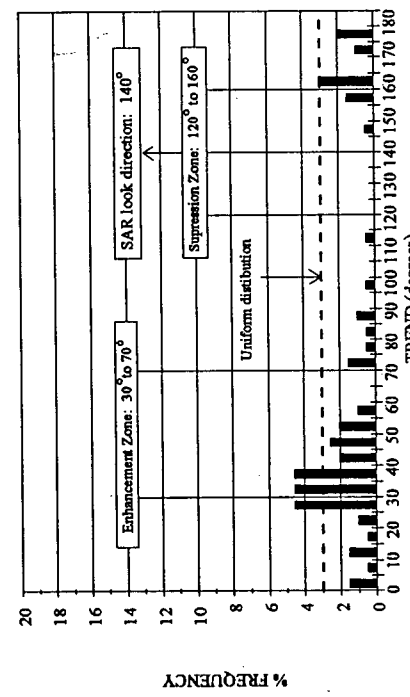
(a) 197 lineaments located with 1:50,000 scale airphotos.



(b) 76 airphoto lineaments located with 1:20,000 scale SAR.



(c) 77 airphoto lineaments located with 1:50,000 scale SAR.



(d) 67 airphoto lineaments located with 1:80,000 scale SAR.

Figure 4.8. Histograms of lineament frequency vs. trend for airphoto lineaments located with SAR imagery.

considerably more east-west than the author's airphoto and SAR lineaments. The author's airphoto and SAR lineament data are closely matched to the Savigny (1995) airphoto lineaments suggesting that differences are likely caused by interpreter biases rather than the imaging tools. Figure 4.9 shows the two sets of lineament data with different length and orientations. It is common for two interpreters to collect slightly different data. Lineament data quality is also commensurate with interpreter experience. The Chilliwack SAR lineaments will not be used in the GIS hazard analysis since the differences in length and trend are substantial and the SAR lineaments would contaminate the regional Savigny (1995) lineament database.

#### 4.9 Landslide Hazard Mapping Methodology

The purpose of Sections 4.9 and 4.10 is to determine the utility of SAR for mapping landslide hazards. Five hazard sites in the Chilliwack study area include the Wahleach instability, the Cheam Slide, the Popkum Slide, and two debris cones. The sites are located in Figure 4.3 and described in Section 4.5. Geomorphological features mapped include the source, transportation, and deposition zones, debris, scarps, and lineaments. The SAR hazard mapping is qualitatively compared to black and white stereo airphotos of similar scale in Figures 4.10 through 4.12. Although a single airphoto is compared, observations presented here are based on interpretation of stereo airphoto pairs.

#### 4.10 Hazard Mapping Results

Figure 4.10 compares an airphoto to an airborne SAR image of the Wahleach instability. The zone of slope deformation boundaries include the white dashed arc and the east-west trending stream gullies intersecting the dashed arc to the north and the south. This is a relatively difficult instability to identify in remote sensing imagery. It is located in airphotos using morphological indicators such as the concave arced depression at A, the north trending lineament left of B, and the north-northwest trending lineaments to the right of C. Despite lower resolution than airphotos, all of these subtle features can be identified in the SAR image because the features have prominent morphological rather than spectral signature. In areas covered by mature forest SAR detects subtle changes in ground morphology by

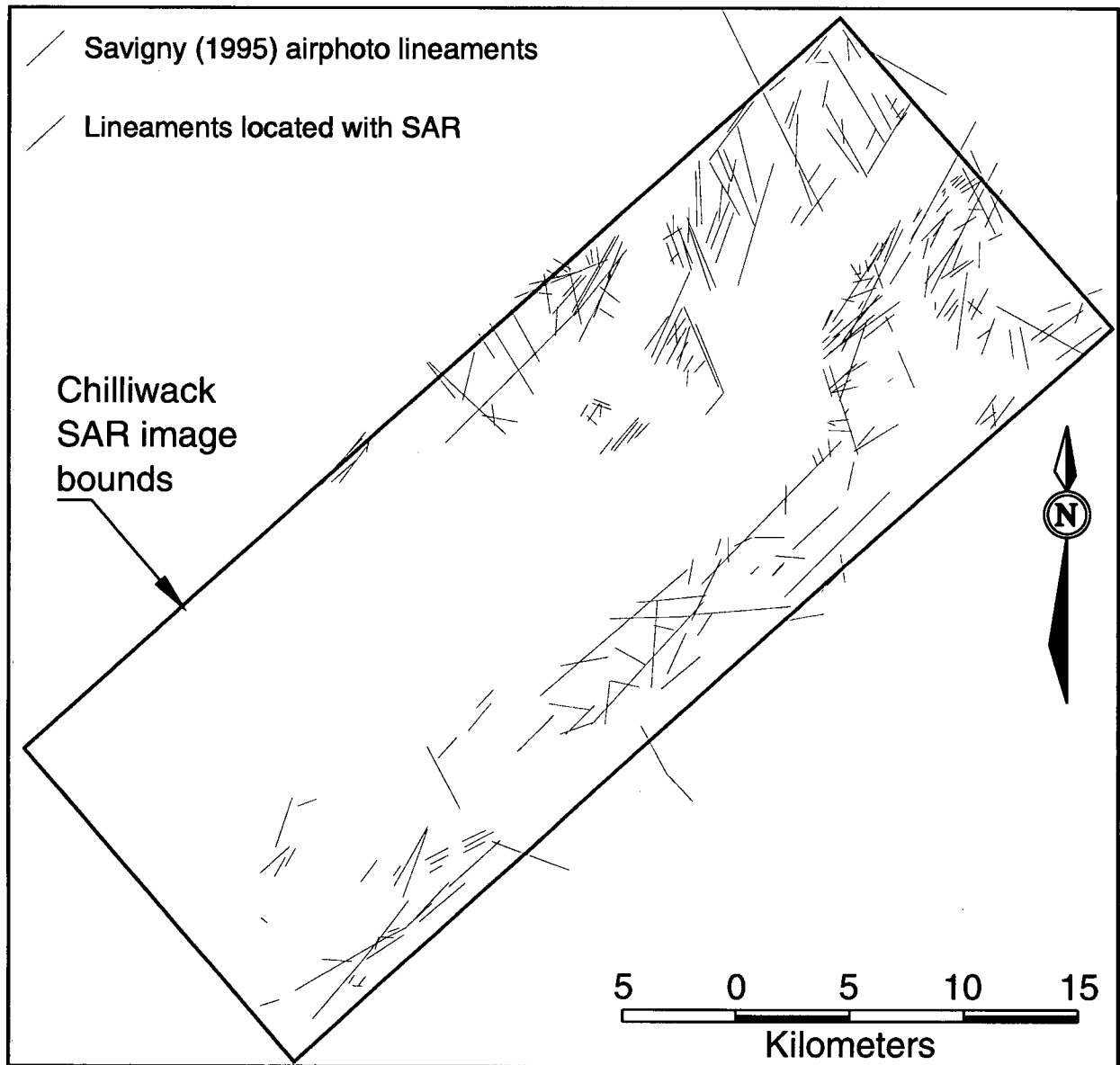


Figure 4.9. Location of Savigny (1995) Chilliwack airphoto lineaments and Chilliwack SAR lineaments.

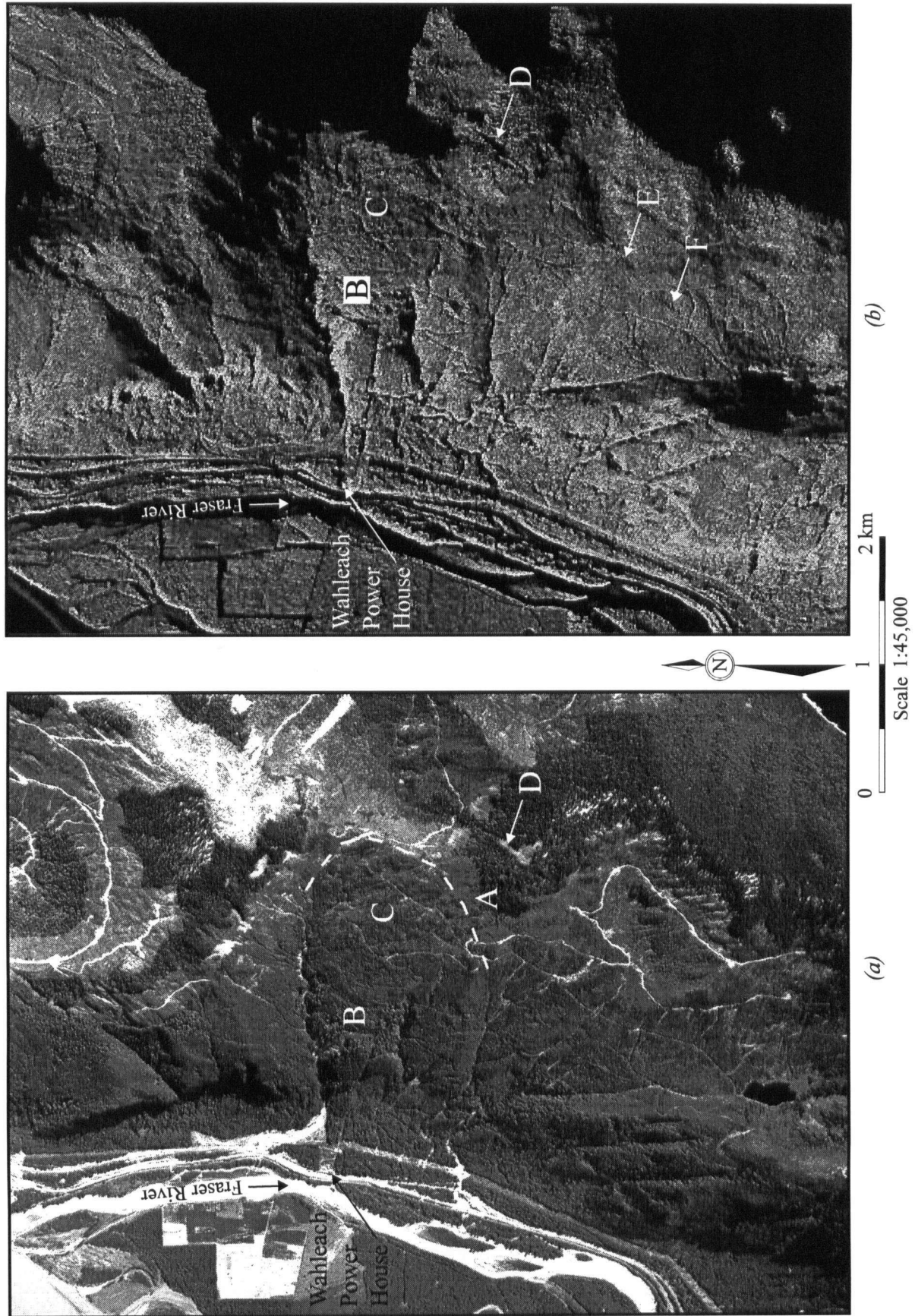


Figure 4.10. The Wahleach hazard seen from (a) airphotos and (b) airborne SAR.

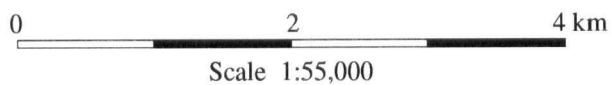
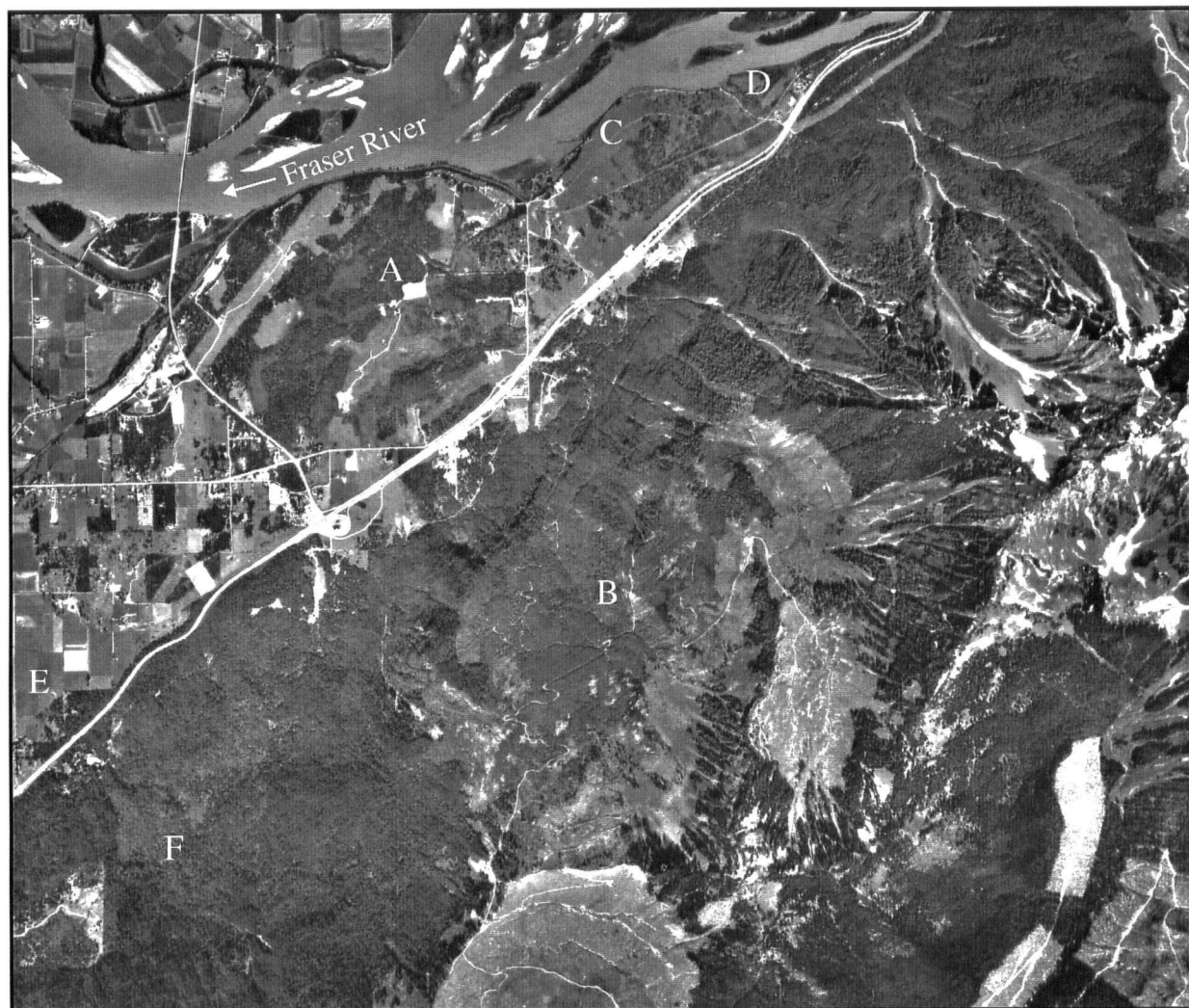
detecting the corresponding changes in tree canopy height. SAR is more sensitive to changes in tree canopy height than stereo airphotos.

Anthropogenic features such as logging roads can often hide landslide hazard evidence. In the SAR image a southwest trending lineament can be identified at D and along trend at E and F. In the airphoto the lineament is identified as a natural open patch in the trees at D but a logging road has hidden the lineament at E and F. The lineament can be seen in the SAR at E and F because lineaments are often appear wider and darker than roads.

In Figure 4.11 the Cheam Slide (A and B), the Popkum Slide (C), and two debris cones (D, and E) are mapped in airphotos and compared to the SAR image in Figure 4.12. The Cheam Slide debris (A) is the most dramatic example of how SAR highlights contrasting geomorphology. The Cheam debris is apparent in stereo airphotos but much of it is hidden by anthropogenic features such as roads, fence lines, buildings, agricultural fields, gravel pits, railway lines, and power lines. In the SAR image the geomorphology of the debris are not hidden. Moreover, the arcuate outward radiating pattern that is common in rock avalanche debris is more apparent in the SAR image. This radial pattern is slightly visible in the Popkum Slide debris seen to the right of C. Additional landslide colluvium between points A and E is easier to locate in the SAR than the airphotos.

Naumann (1990) proposed that an asymmetrical wedge on the mountain side above the Cheam Slide debris (B) is the source area for the Cheam Slide. Stereo aerial photographs are required to see the wedge. In the SAR image a bowl bounded by two mountain ridges is all that can be discriminated. The wedge cannot be seen because the line of intersection between the two planes trends nearly parallel with the SAR look direction.

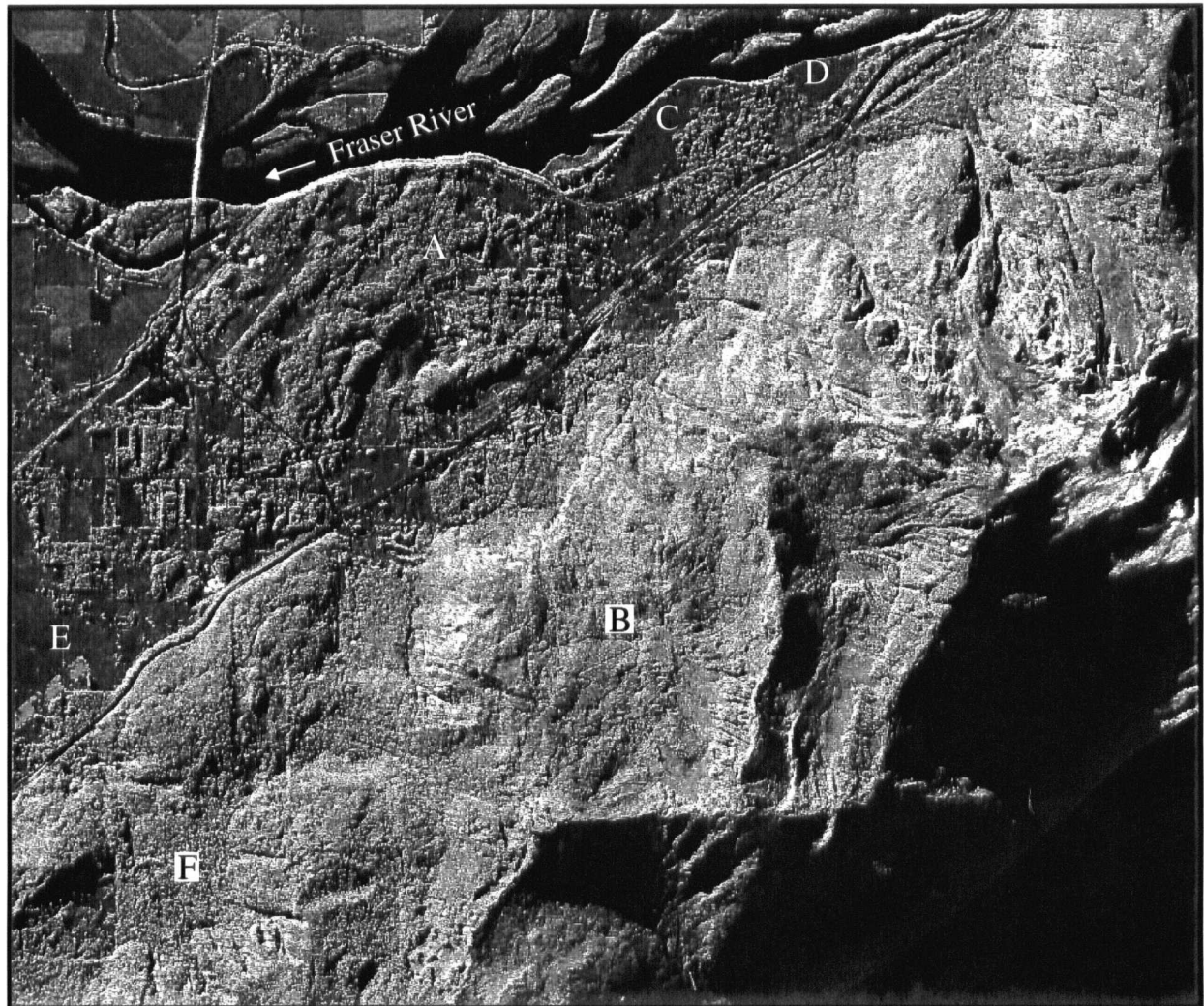
Immediately right of C is the debris to the Popkum Slide. Again anthropogenic disturbance, especially the removal of trees, has made it difficult to identify the Popkum landslide colluvium in stereo airphotos. Changes in surface texture caused by the contrasting SAR returns of the flat fields and the tree covered debris makes the geomorphological change apparent in the SAR imagery. Like the Cheam debris a faint radial pattern can be seen in the Popkum debris. A source area for this debris can not been determined. The Popkum debris may be related to the debris fan located directly across the highway.



- A Cheam Slide debris
- B Cheam Slide source area
- C Popkum Slide debris
- D Debris cone
- E Debris cone
- F Debris cone source area



Figure 4.11. Cheam Slide, Popkum Slide and debris cones seen in an airphoto.



0 2 4 km  
Scale 1:55,000

- A Cheam Slide debris
- B Cheam Slide source area
- C Popkum Slide debris
- D Debris cone
- E Debris cone
- F Debris cone source area



Figure 4.12. Cheam Slide. Popkum Slide, and debris cones seen in airborne SAR.

To the right of D is a tree covered debris cone traversed by the highway and a gas and an oil pipeline. The cone is a deposition zone for continuous raveling and sporadic debris flow events originating from the mountainside. The cone can be seen in stereo airphotos but because of the contrasting geomorphology between the flat Fraser floodplain, the cone, and the steep mountainside, the cone stands out very well in the SAR image. The source and transportation zones for this cone are readily mapped in both images.

At E another debris cone spills onto the flat floodplain. The source and transportation zones for the cone are labeled at F. Unlike the source zone for the Cheam Slide, the correct SAR viewing geometry has highlighted a bowl shaped source area that is not, even with stereo viewing, visible in aerial photographs.

#### 4.11 Conclusions

Lineaments in the Chilliwack study area are located and digitized on-screen using geocoded 1:20,000, 1:50,000, and 1:80,000 scale C-band SAR and compared to 1:50,000 scale black and white airphotos. SAR lineament length and trend correlate well with lineaments found in airphotos. As with airphotos, as SAR image scale increases observed lineament frequency also increases and lineament length decreases. SAR lineament length and trend are less sensitive to changes in scale than airphoto lineaments.

The ability of SAR imagery to locate specific airphoto lineaments was tested. 1:50,000 scale SAR located the most airphoto lineaments (39%). SAR tends to enhance the longer airphoto lineaments. It was expected that SAR would locate most of the airphoto lineaments within the 030° to 070° enhancement zone. This was not the case. In fact, this zone missed more airphoto lineaments than any other. Since 53% (88 out of 165) of the SAR lineaments are not airphoto lineaments, most of the lineaments found with SAR provide additional structural information about the Chilliwack area.

The Savigny lineaments are, on average, longer and trend considerably more east-west than the author's airphoto and SAR lineaments. The author's airphoto and SAR lineament data are a close match compared to the Savigny airphoto lineaments suggesting that the differences are likely caused by

interpreter biases rather than the imaging tools. The Chilliwack SAR lineaments will not be used in the GIS hazard analysis since the differences in length and trend are substantial and the SAR lineaments would contaminate the regional Savigny lineament database.

Landslide hazard mapping was done using black and white stereo aerial photographs and the results were quantitatively compared to equivalent scale 10 m resolution SAR imagery. SAR imagery is a very useful tool for detecting landslide hazard features that have geomorphological characteristics. Such features include, lineaments, antislope scarps, deformation zones, and especially hummocky debris lobes, cone and fans.

Despite a lower resolution than airphotos, SAR detected all of the major features seen in airphotos. In areas masked by anthropogenic features such as logging and cultivation, SAR proved more useful in revealing landslide debris and lineaments. In areas covered by mature forest SAR detects subtle changes in ground morphology by detecting the corresponding changes in tree canopy height. Airphoto stereo is less sensitive to changes in tree canopy height.

The outward radial pattern typical of rock avalanche debris was more visible in SAR imagery. Analysis of this radial pattern helps locate the source and determine mechanics of the slide. Depending on the viewing geometry SAR is able to detect hazard source zones not apparent in stereo airphotos while in other circumstances features are more easily detected by analyzing aerial photographs.

## CHAPTER 5

### Landslide Hazard Zoning Using an Objective GIS Model

#### 5.1 Introduction

Landslide hazard mapping is not restricted to locating landslides but it is focused on making predictions about the occurrences of future landslides. Landslide hazard maps outline zones of probability of landslide occurrence calculated from the presence or absence of contributing factors such as weak bedrock type or geologic structure. These maps are used for land use planning and regulation, documenting landslide damage potential, routing and design of linear facilities, and forest harvesting and road building (Gerath *et al.* 1994). For a given area three basic principles guide all landslide zonation studies (Varnes 1984); 1) Future natural slope failures will most likely be in geologic, geomorphic and hydrologic situations that have led to past and present failures; 2) Identifying the failure inducing factors of landsliding permits extending landslide occurrence prediction into larger areas; and, 3) the degree of potential hazard can be built up depending on the number of failure-inducing factors present, their severity and their interaction.

A GIS is an exceptionally useful tool for landslide zonation studies because, like most GIS projects, map data from diverse sources (point, line, polygon, raster) can be digitally captured, co-registered, stored, and then quantitatively modeled. Beyond the storage and display utility of GIS is the rapid quantitative multivariate modelling of spatial data. Although currently under-utilized in GIS, quantitative modelling is an infinitely more powerful GIS technique for decision makers. IDRISI (Eastman 1993) and SPANS from the Ottawa-based company Intera-Tydac Inc. are examples of raster based GIS software providing a wide scope of modelling functions. For example overlaying two or more

input maps, say of slope angle, surficial, and bedrock geology, within various models produces an output map of landslide potential. These multivariate models may be physical (Wadge 1988) (deterministic or deductive), or empirical (inductive) (Wadge *et al.* 1991) based on theoretical, semi-empirical, heuristic, or statistical relationships (Bonham-Carter 1994a) (Fig 5.1). The models and method of description usually form the core of an expert system (Wislocki and Bentley 1991, Pearson *et al.* 1991, Wislocki *et al.* 1992).

Physical models usually utilize theoretical and semi-empirical relationships (Fig. 5.1). Theoretical models, such as finite element or finite difference groundwater flow models based on the equations of fluid motion, are usually too complex to practically incorporate into a GIS although a GIS may be used to define input data or visualize results. Semi-empirical models used within a GIS include rockfall energy balance (van Dijke and van Westen 1990), and the infinite slope stability model (Wadge 1988, Brass *et al.* 1991) incorporating root cohesion (Shasko and Keller 1991). Input maps include slope angle, soil depth, soil strength, depth to the groundwater table, and vegetation type. Hazard assessment is usually obtained by calculating a factor of safety for each grid cell over the study area and cells with a factor of safety greater than one are considered stable. Semi-empirical models are best reserved for smaller study areas (< 1:100,000 scale) with relatively uniform geology where the distances between data points or drill holes are short enough for easier interpolation. These types of models often rely on an accurate DEM to determine slope distances, angles and heights.

As a general rule, empirical models (Fig. 5.1) are used in hazard mapping when the governing principles are too complex to express mathematically. When empirical techniques are used, factors contributing to the occurrence of a hazard are weighted based on the relative importance of that factor. The assignment of these weights may be “knowledge-based”, that is, assigned on the basis of subjective expert opinion (Gupta and Joshi 1990, Mejía-Navarro *et al.* 1994, Mejía-Navarro and Wohl 1994), or they may be “data-based” using objective statistical criteria. Objective statistical methods, which require a landslide database, include logistic regression (Yin and Yan 1988, Ellen *et al.* 1993), stepwise discrimination (Carrara *et al.* 1991), and weights of evidence (Bonham-Carter *et al.* 1988, 1989, Goodacre *et al.* 1993).

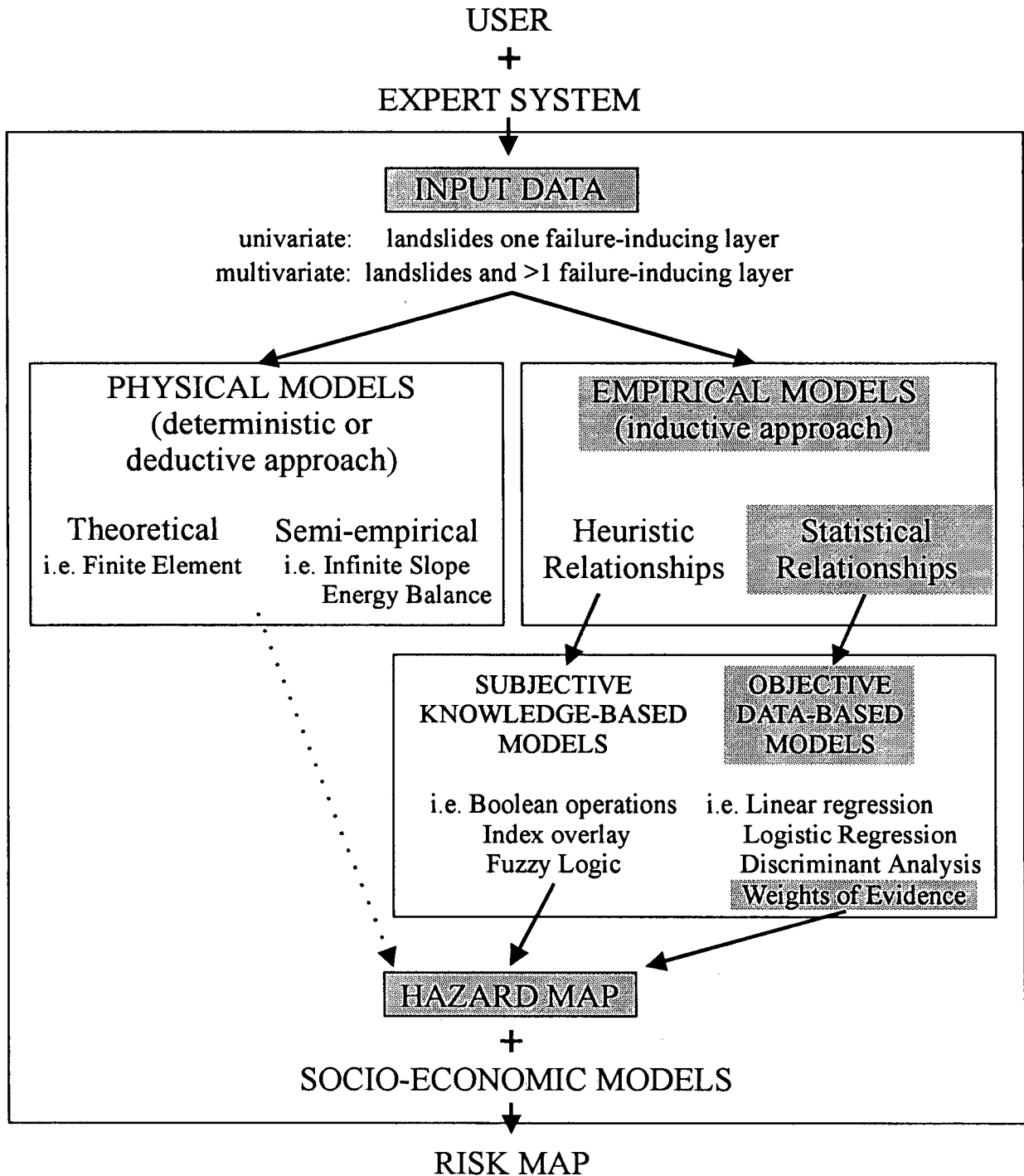


Figure 5.1. Schematic diagram of GIS models within a landslide hazard expert system. Shaded components are addressed in this study.

Other objective methods such as Monte Carlo simulations for resolving spatial uncertainty or Frequency-Magnitude analyses on past landslide events may be performed to supplement the database.

Hazards become significant only when they impinge upon human activity. A socio-economic rulebase describes the potential social and economic loss sustained if a landslide is to occur. These rules are incorporated into the GIS using empirical techniques and are combined with the hazard map to produce a risk map. Socio-economic rules and the generation of risk maps are beyond the scope of this research.

The most recent multivariate geological hazard studies have used knowledge-based methods to rank the controlling factors for landslide occurrence (Gupta and Joshi 1990, Mejía-Navarro *et al.* 1994, Mejía-Navarro and Wohl 1994). Multivariate objective methods are computationally intensive because every combination of factors must be analyzed (Yin and Yan 1988) so recent evaluations have used a single controlling factor, usually climate (Ellen *et al.* 1993). The work presented in this thesis differs from other GIS landslide hazard studies in that 1) the multiple controlling factors are ranked objectively, 2) the weights of evidence algorithm is used, 3) large rock landslides are investigated, and 4) it is the first landslide hazard study in Canada to use a GIS.

## 5.2 Weights of Evidence Method

This study uses the multivariate data-driven statistical model called weights of evidence to objectively rank and combine four failure-inducing data layers (bedrock geology, faults, lineaments, and slopes) into a map of landslide hazard potential. Originally developed in a nonspatial context for disease prediction (Spiegelhalter and Knill-Jones 1984), Bonham-Carter *et al.* (1988, 1989), Agterberg (1989), Agterberg *et al.* (1990), Bonham-Carter (1994a) have applied the weights of evidence methodology to spatial data for predicting the location of gold deposits and earthquake epicenter densities (Goodacre *et al.* 1993).

Weights of evidence modelling uses the locations of known landslide hazard occurrences (called the response variable) to objectively determine the weights for each failure-inducing map (called the predictor variable). Both the response and predictor variables are binary, that is, they are either present

(on) or absent (off) although a predictor map may be multistate (i.e. multiple rocks types in a bedrock geology map). Two weights,  $W^+$  and  $W^-$ , for each predictor map refer to where the binary pattern is either present or absent, respectively. Using Bayesian statistics, weights  $W^+$  and  $W^-$  are calculated using areas of the predictor variables, the total study area, the landslide area intersecting each predictor variable, and the total area of landslides within the study area. Weights usually vary between 2 and -2 and a weight of 0 is used where the pattern is missing or unknown.  $W^+$  is the amount of positive influence that predictor variable has on the probability of a slide being present.  $W^-$  is the amount of negative influence that predictor map has on the probability of a slide being present. The difference  $C = W^+ - W^-$  indicates the predictive power of that binary map. The higher this difference the more likely a slide will be present within that binary predictor map. The influence of each predictor map can be objectively ranked using  $C$  and the significance of  $C$  tested by estimating  $s(C)$ , the sample variance. The variance of the contrast  $s(C)$  is approximately the sum of the variances of the weights. Using an application of Bayes Rule and the assumption of conditional independence between the predictor maps, a map of posterior probability of landslide occurrence is created by adding (for each cell within the study area) the weights of each input map to the prior probability of landslide occurrence. The posterior probability may be larger or smaller than the prior probability depending on the overlap combination of predictor maps and their weights. Variances in the weights  $s(W)$  are used to determine the uncertainty in the calculated posterior probability.

In summary, the weights of evidence calculations involve several steps. These steps are well described with examples in Bonham-Carter *et al.* (1989) and Bonham-Carter (1994a).

- 1) A series of predictor maps (i.e. bedrock geology, faults, lineaments, etc.) are chosen that are likely to be useful evidence for predicting landslide occurrence. A conceptual landslide model (i.e. Savigny 1995) for the study area usually serves as a guide to the selection process.

- 2) Each predictor map must be binary. Multiclass maps (i.e. bedrock geology) must be reclassified to binary form by combining or removing classes. Weights of evidence calculations can be used on each class to select the important classes. Vector maps (faults, lineaments, contacts) may be optimized using buffers as described below in Section 5.4.

- 3) Estimate the prior probability of landslide occurrence. (i.e. the probability of landslide occurrence per unit cell, given no further information). In this study the prior probability happens to be 0.02 calculated by dividing the total area of the landslides by the total study area.
- 4) Calculate the positive and negative weights ( $W^+$  and  $W^-$ ), contrast  $C$ , sample variances  $s(W^+)$ ,  $s(W^-)$ , and  $s(C)$  for each binary predictor map, using conditional probability ratios.
- 5) Test for conditional independence of each pair of predictor maps with respect to landslide occurrence using a pairwise test. Combine or remove problem maps to reduce the effects of conditional independence. Tests for conditional independence require an overlap between two predictor maps and the response variable and are generally carried out outside the GIS using data files generated by the GIS.
- 6) Generate the posterior probability map of landslide occurrence by adding the weights of several predictive maps using a formulation of Bayes Rule.
- 7) Generate a posterior probability variance map to determine the uncertainty of posterior probability calculations.
- 8) Apply a goodness-of-fit test to check the overall conditional independence assumption.

As outlined in the introduction, to date, most GIS hazard studies have used subjective methods or objective regression techniques to assign the weights for each predictor map. Weights of evidence is considerably more computationally intensive than methods involving subjective choice of weights. In comparison to the regression technique, weights of evidence is easy to interpret, simple to program, missing data can be accommodated, and patterns with complex spatial geometry (i.e. complex bedrock geology) can be modeled with the same computational effort as simple geometry (Bonham-Carter *et al.* 1989). Weights of evidence is particularly well-suited to situations in which the response variable is a binary point object, such as a seismic epicenter. Weights of evidence can also be useful for predicting the presence/absence of an area object, such as a landslide, although the uncertainty of the weights and posterior probability cannot be considered absolute, and should be used in a relative sense only (Bonham-Carter 1994b). This is the case in this study.

Other advantages of weights of evidence include the ability to determine a zone of influence around a vector predictor map by optimizing the contrast  $C$  using binary reclassification techniques.

This is discussed in Section 5.4. Finally, variances of weights and missing data can be mapped to show the uncertainty in the calculated posterior probability map. Areas where the posterior probability is less than 1.5 times the variance are relatively uncertain and may be masked out from the posterior probability map.

On the other hand weights of evidence is only applicable in regions where the response variable is fairly well known (i.e. a landslide inventory is available) so that the weights and posterior probability can be calculated. This model is not always applicable in poorly explored regions, and if it is used with only a small number of landslide occurrences, the results must be interpreted with caution. The predictor maps must be conditionally independent with respect to the landslides and this should be tested. Regression modelling does not require conditional independence. Additionally, highly correlated predictor maps are not suitable for weights of evidence modelling. For example if the presence or absence of a lineament depends on whether a fault is present or absent then the lineament and fault predictor maps may be correlated and should not be used with weights of evidence modelling unless they are pretreated by principal component analysis, or similar methods (Bonham-Carter 1994b). Weights of evidence is not an appropriate method where the response variable is multistate or continuous (i.e. not binary). Thus it cannot be used to predict number of landslides nor the size of landslide unless the landslide dataset is partitioned into binary subsets (small, medium, and large landslides) and the methodology is applied to each subset. As a cautionary note, the actual values of the weights and contrast, although not sensitive to the choice of unit cell size (1 ha in this study), can be sensitive to the choice of the study region. By changing the boundaries of the region the values of the weights can be drastically changed. This does not negate the usefulness of the approach, but does indicate that the results are region-dependent (Bonham-Carter 1994b).

### 5.3 Data Inputs

As concluded in Chapter 3, airphoto inventory of landslides and lineaments, spatial relationships between regional faults, lineaments, plutonic contacts, and pendant rocks and landslide hazard occurrence have been proposed by Savigny (1995). To quantitatively investigate these spatial relationships,

predictor maps of lineaments, faults, bedrock geology, and a digital elevation model are coregistered in the IDRISI GIS software as raster layers with 100 m pixels. The study area, shown in Figure 2.1, is the west half of the 1:250,000 scale 92H NTS topographic mapsheet. Faults and bedrock geology (Fig 2.1 and Fig 5.2) are digitized from a 1:250,000 scale bedrock geology map (Monger 1989). For simplicity the mechanical character of the faults are not distinguished. Landslides and lineaments (Fig. 3.1) compiled from the airphoto inventory (Savigny 1995, English *pers. comm.*) are digitized from a 1:250,000 mapsheet. The 1:250,000 scale DEM provided by the B.C. Ministry of Environment is resampled from 75 m to 100 m pixels and converted to a slope map using the IDRISI functions. The multiclass bedrock geology and slope maps and the vector fault and lineament maps are reclassified into a binary form that maximized the spatial relationships between them and the landslide polygons. Correlations between seismic epicenters and faults were investigated using weights of evidence. Due to the type (deep seismic events) and spatial accuracy ( $\pm 10$  km) of the seismic data and the absence of a distribution pattern, relationships between the surface trace of faults and the epicenters could not be made. Seismic epicenter data are not included in this investigation.

#### 5.4 Binary Map Reclassification

The process of converting multiclass maps to a binary form is carried out subjectively, using geological judgment, or objectively using statistics. In the field of geology where there is relatively more reliance on subjective interpretation, usually the best technique is to reclass the map subjectively using the objective reclassification as a guide. Results of binary reclassification of bedrock, faults, lineaments, and plutonic contacts are provided, along with sample calculations, in Appendix III. Binary reclassification procedures are described in Bonham-Carter *et al.*(1988, 1989) and Bonham-Carter (1994a) so the technique is briefly described here.

The multiclass bedrock geology map is partitioned into separate binary maps with each map representing one bedrock group or formation. Attempts are made to subjectively group the bedrock geology into five engineering geology classes (Massive, Foliated, Bedded, Volcanic, and Carbonate). Since the bedrock geology GIS layer is originally classified by formation rather than rock type, a

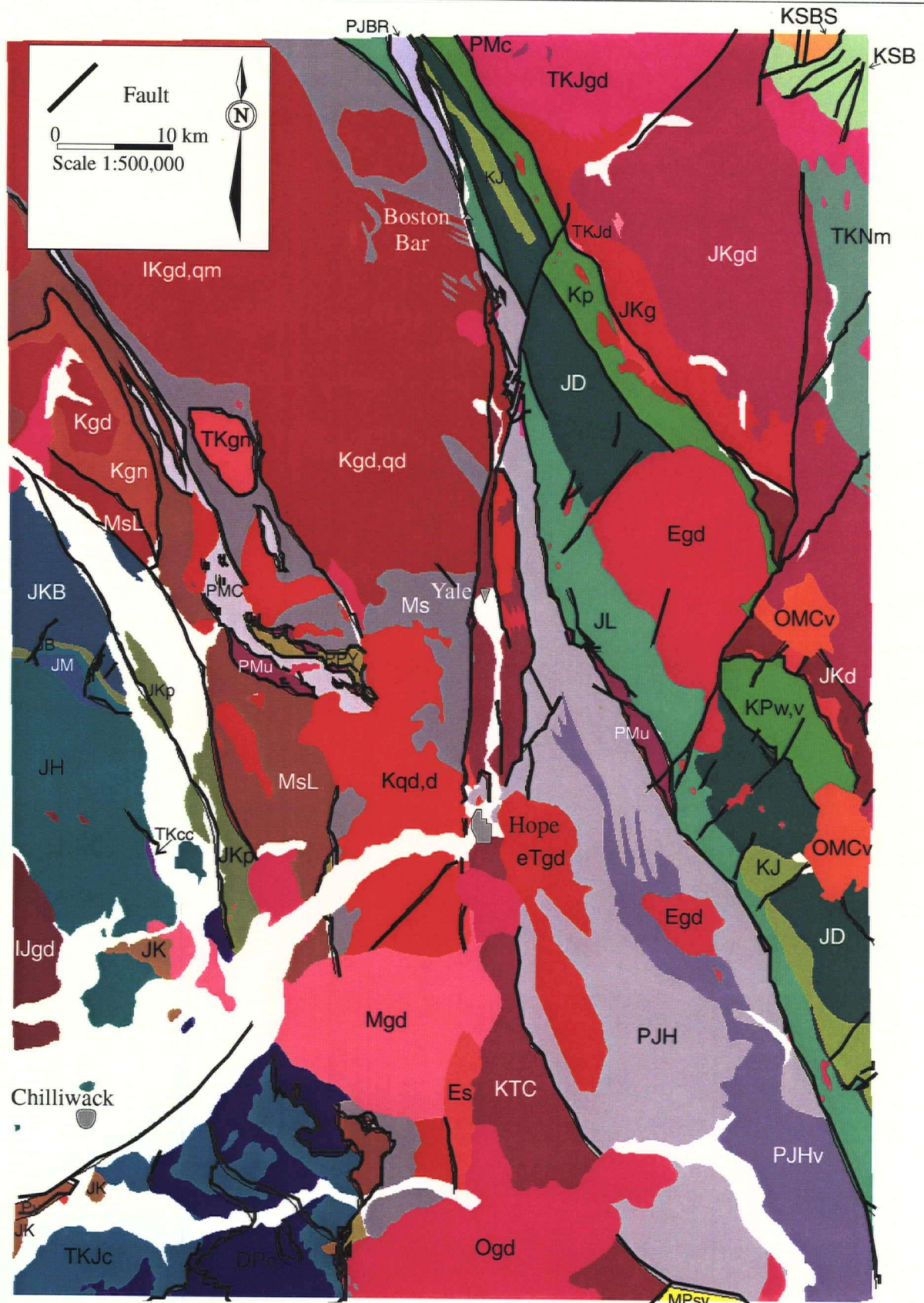


Figure 5.2. Bedrock geology and faults in the Hope study area. Adapted from Monger (1989).

white	QUATERNARY SEDIMENTS	glacial till, glacial fluvial, glacial lacustrine, alluvium, colluvium
MPSv	SKAGIT FORMATION:	felsic, intermediate pyroclastics
Mgd	MOUNT BARR BATHOLITH:	granodiorite
OMCv	COQUIHALLA FORMATION:	intermediate, felsic pyroclastics, and flows
Ogd	CHILLIWACK BATHOLITH:	granodiorite
Egd	MOUNT OUTRAM PLUTONS:	granodiorite
Es	EOCENE SEDIMENTARY	Sandstone, conglomerate, argillite
eTgd		Intrusions of granodiorite
KTC	CUSTER GNEISS:	pegmatitic granite gneiss, pelitic schist and amphibolite
Ms	SETTLER SCHIST:	garnet biotite, staurolite, kyanite and sillimanite schist local amphibolite and siliceous schist
MsL	SLOLLICUN SCHIST:	mainly greenschist grade, mafic to intermediate volcanics, phyllite, minor volcanic, carbonate-clast conglomerate
IKgd,qm	SCUZZY PLUTON:	granodiorite (gd), quartz monzonite (qm)
KSB	SPENCES BRIDGE GROUP:	volcanics, sandstone, shale, conglomerate.
KSBS	SPIUS CREEK FORMATION:	mafic volcanics
KPw,v	PASAYTEN GROUP:	undifferentiated sandstone, conglomerate, argillite, minor tuff
KJ	JACKASS MOUNTAIN GROUP:	sandstone, argillite, conglomerate
Kqd	SPUZZUM PLUTON:	quartz diorite, diorite
Kgn	BREAKENRIDGE GNEISS:	felsic and mafic gneiss
JKB	BROKENBACK HILL FORMATION:	intermediate pyroclastics and flows
JKP	PENINSULA FORMATION:	sandstone and conglomerate
Jkgd	EAGLE PLUTONIC COMPLEX:	granodiorite and gneiss
Jkd	EAGLE PLUTONIC COMPLEX:	diorite and amphibolite
Jkg	EAGLE PLUTONIC COMPLEX:	muscovite-biotite granite and pegmatite

BEDROCK GEOLOGY LEGEND (adapted from Monger 1989)

IJs	THUNDER LAKE SEQUENCE:	sandstone, conglomerate, argillite
JK	KENT FORMATION:	conglomerate, sandstone, argillite
IJg	OSPREY LAKE BATHOLITH:	granite and granodiorite
JB	BILLHOOK CREEK FORMATION:	intermediate volcanics
JM	MYSTERIOUS CREEK FORMATION:	argillite, tuff
JH	HARRISON LAKE FORMATION:	volcanics, pyroclastics, argillite, conglomerate
JL	LADNER GROUP:	argillite, siltstone
JD	DEWDNEY CREEK FORMATION:	sandstone, argillite, volcanics
TKJgd	MOUNT LYTTON COMPLEX:	granodiorite
TKJd	MOUNT LYTTON COMPLEX:	diorite and amphibolite
TJu	TULAMEEN COMPLEX:	alkaline intrusions, ultramafic
TKJc	CULTUS FORMATION:	argillite, sandstone, minor carbonate
TKNm	NICOLA GROUP:	amphibolite, foliated diorite, mylonite and chlorite schist, marble
TKcc	CAMP COVE FORMATION:	siliceous argillite, mafic volcanics
TKgn	HORNET CREEK GNEISS:	granite-gneiss
PMc	COGBURN SCHIST:	meta-chert, pelite, amphibolite, marble, ultramafic rock
PMu		Ultramafic rock, local gabbro
PJH	HOZAMEEN COMPLEX:	undifferentiated chert pelite, volcanics, minor limestone
PJHv	HOZAMEEN COMPLEX:	mafic volcanics
PJBR	BRIDGE RIVER COMPLEX:	siliceous chlorite schist, phyllite
PJu		Ultramafic rock, local gabbro
Pv	VEDDER COMPLEX:	amphibolite, gneiss, minor ultramafic rock
DPc	CHILLIWACK GROUP:	undifferentiated pelite, sandstone, minor conglomerate, mafic and felsic volcanics, carbonate
PPY	YELLOW ASTER COMPLEX:	metadiorite and gabbro

BEDROCK GEOLOGY LEGEND continued (adapted from Monger 1989)

formation may be included in more than one engineering geology class. This causes serious conditional independence and autocorrelation problems so the engineering classification was abandoned. Calculated weights, variances, contrasts, and Studentized values of contrast for each bedrock formation are listed in Table 5.1. The formations are listed in order of their Studentized value of the contrast  $C/s(C)$ . Normally the magnitude of the contrast  $C$  indicates the predictive power of that map. A better indicator is the Studentized value of the contrast which is the measure of certainty with which the contrast is known. If the ratio is large, implying the contrast is large compared to the standard deviation, the contrast is more likely to be real. Ideally it is desirable to see a Studentized value greater than 1.5 or 2 (Bonham-Carter 1994b). Small areas will usually result in a large standard deviation and smaller studentized value suggesting the contrast  $C$  is not as reliable as other contrasts. In Table 5.1 formations in the shaded region have Studentized contrasts greater than 1.5 and are considered "good" data. The  $W+$  weights of these formations will be used to create the map of posterior probability of landslide occurrence. Ultramafic gabbro rocks have the largest contrast but a high standard deviation that reduces the reliability of the contrast magnitude. The Custer Gneiss, Chilliwack Group, and Cultus Formations are the three most important bedrock predictors of landslide occurrence. Granite gneiss, pelitic schist, amphibolite, pelite, sandstone, conglomerate, carbonate, and argillite are rocks that comprise these three formations. As expected, from an engineering standpoint, the massive younger plutonic rocks are not good predictors of landslide occurrence as indicated by the negative contrast  $C$ .

The multiclass slope map was reclassified subjectively into six classes;  $< 10^\circ$ ,  $10^\circ < 20^\circ$ ,  $20^\circ < 30^\circ$ ,  $30^\circ < 40^\circ$ ,  $40^\circ < 50^\circ$ , and  $> 50^\circ$ . Additional classes may maximize the spatial relationship between slope and landslide occurrence but too many classes increase computational effort the possibility of conditional dependence.

Binary reclassification of the faults, lineaments, and plutonic contacts predictor maps used an objective approach. This approach is the same for each vector map so the technique is illustrated here using the fault map. The question is, in determining how to make a binary anomaly map from the faults map, what is the best distance to choose a cutoff? By making the buffer too narrow, the effect is to reduce the binary pattern to a very small area, and many of the landslide occurrences are missed. By

Rock Group/Formation	W+	s(W+)	W-	s(W-)	C	s(C)	C/s(C)
Custer Gneiss	1.7732	0.0220	-0.1174	0.0081	1.8906	0.0235	80.5926
Chilliwack Group	1.5737	0.0259	-0.0778	0.0080	1.6514	0.0271	61.0072
Cultus Formation	1.4190	0.0297	-0.0550	0.0079	1.4740	0.0307	48.0142
Spuzzum Pluton	1.0960	0.0244	-0.0719	0.0080	1.1679	0.0257	45.5322
Slollicun Schist	0.9843	0.0285	-0.0482	0.0079	1.0325	0.0296	34.8816
Peninsula Formation	1.2024	0.0521	-0.0158	0.0077	1.2182	0.0526	23.1433
Ultramafic, gabbro	1.2297	0.0598	-0.0121	0.0076	1.2418	0.0603	20.5873
Dewdney Creek Formation	0.5108	0.0319	-0.0241	0.0078	0.5348	0.0328	16.2967
Ultramafic, gabbro	2.0142	0.1303	-0.0033	0.0076	2.0175	0.1305	15.4595
Hozameen Complex	0.1977	0.0259	-0.0167	0.0079	0.2144	0.0271	7.9087
Hozameen Complex	0.2576	0.0416	-0.0078	0.0077	0.2655	0.0423	6.2787
Billhook Creek Formation	0.7895	0.1559	-0.0013	0.0076	0.7909	0.1561	5.0663
Jackass Mountain Group	0.1402	0.0802	-0.0012	0.0076	0.1414	0.0806	1.7547
Ladner Group	0.0347	0.0431	-0.0011	0.0077	0.0358	0.0438	0.8162
Princeton Group	-0.2951	0.1106	0.0016	0.0076	-0.2967	0.1109	-2.6763
Breakenridge Gneiss	-0.4769	0.1067	0.0031	0.0076	-0.4799	0.1069	-4.4877
Eagle Plutonic Complex	-0.6318	0.1394	0.0026	0.0076	-0.6344	0.1396	-4.5429
Coquihalla Formation	-0.6953	0.1185	0.0041	0.0076	-0.6994	0.1187	-5.8920
Pasayten Group	-5.2604	0.7071	0.0218	0.0076	-5.2822	0.7072	-7.4694
Needle Peak Pluton	-0.4344	0.0550	0.0105	0.0077	-0.4450	0.0555	-8.0130
Chilliwack Batholith	-0.4095	0.0491	0.0123	0.0077	-0.4218	0.0497	-8.4831
Mount Barr Batholith	-0.5300	0.0618	0.0107	0.0076	-0.5407	0.0623	-8.6830
Settler Schist	-0.5430	0.0500	0.0170	0.0077	-0.5600	0.0506	-11.0729
Eagle Plutonic Complex	-2.0253	0.1624	0.0142	0.0076	-2.0396	0.1626	-12.5420
Early Tertiary Intrusions	-2.0328	0.1493	0.0170	0.0076	-2.0498	0.1495	-13.7145
Eagle Plutonic Complex	-1.3383	0.0591	0.0475	0.0077	-1.3859	0.0596	-23.2613
Scuzzy Pluton	-1.5433	0.0418	0.1318	0.0077	-1.6751	0.0425	-39.4451

**Table 5.1.** *Weights, standard deviations, and contrasts for bedrock geology ranked by the Studentized value of contrast C/s(C).*

making the buffer too large the capability of the faults for narrowing the search area is reduced. To determine the optimal buffer width the weights are calculated for 100 m wide successive cumulative distance buffers and the variations are examined. Variation of weights of evidence with cumulative distance from faults is shown in Table 5.2.

Distance (m)	W+	s(W+)	W-	s(W-)	C	s(C)	C/s(C)
<100	0.4773	0.0510	-0.0087	0.0077	0.4860	0.0516	9.4208
200	0.4954	0.0258	-0.0368	0.0079	0.5322	0.0270	19.7233
300	0.5223	0.0196	-0.0707	0.0082	0.5930	0.0212	27.9477
400	0.5528	0.0171	-0.1009	0.0085	0.6537	0.0191	34.2767
500	0.5858	0.0153	-0.1369	0.0087	0.7227	0.0176	40.9502
600	0.6165	0.0136	-0.1927	0.0092	0.8092	0.0164	49.3328
700	0.6424	0.0127	-0.2406	0.0095	0.8830	0.0158	55.7540
800	0.6658	0.0118	-0.3031	0.0099	0.9688	0.0154	62.7967
900	0.6837	0.0111	-0.3738	0.0105	1.0575	0.0152	69.3902
1000	0.6918	0.0106	-0.4386	0.0110	1.1304	0.0152	74.2134
1100	0.6899	0.0102	-0.4965	0.0114	1.1864	0.0153	77.4137
1200	0.6840	0.0099	-0.5466	0.0119	1.2306	0.0155	79.5335
<b>1300</b>	<b>0.6648</b>	<b>0.0097</b>	<b>-0.5893</b>	<b>0.0123</b>	<b>1.2541</b>	<b>0.0157</b>	<b>80.0665</b>
1400	0.6416	0.0095	-0.6255	0.0127	1.2671	0.0159	79.8096
1500	0.6182	0.0094	-0.6510	0.0131	1.2692	0.0161	78.9752

**Table 5.2.** Variation of weights of evidence with cumulative distance from faults. Studentized contrast  $C/s(C)$  is a maximum at 1300 m from the faults.

By inspecting the Studentized contrasts for faults in Table 5.2 1300 m is chosen as the optimal fault buffer size for predicting landslide occurrence. The contrast C did not peak as cumulative area increased so the optimal buffer width was chosen where the Studentized value of C ( $C/s(C)$ ) peaked. Figure 5.3 shows the 1300 m wide buffer with the faults and landslides superimposed. The positive weight at 1300 m  $W+ = 0.6488$  is assigned to where the buffer is present and  $W-$  assigned to where the buffer is absent. The lineaments predictor map was thresholded at 1200 m. This indicates that the predictive power of a lineament is maximized within 1200 m of the lineament.  $W = 0$  is assigned to the

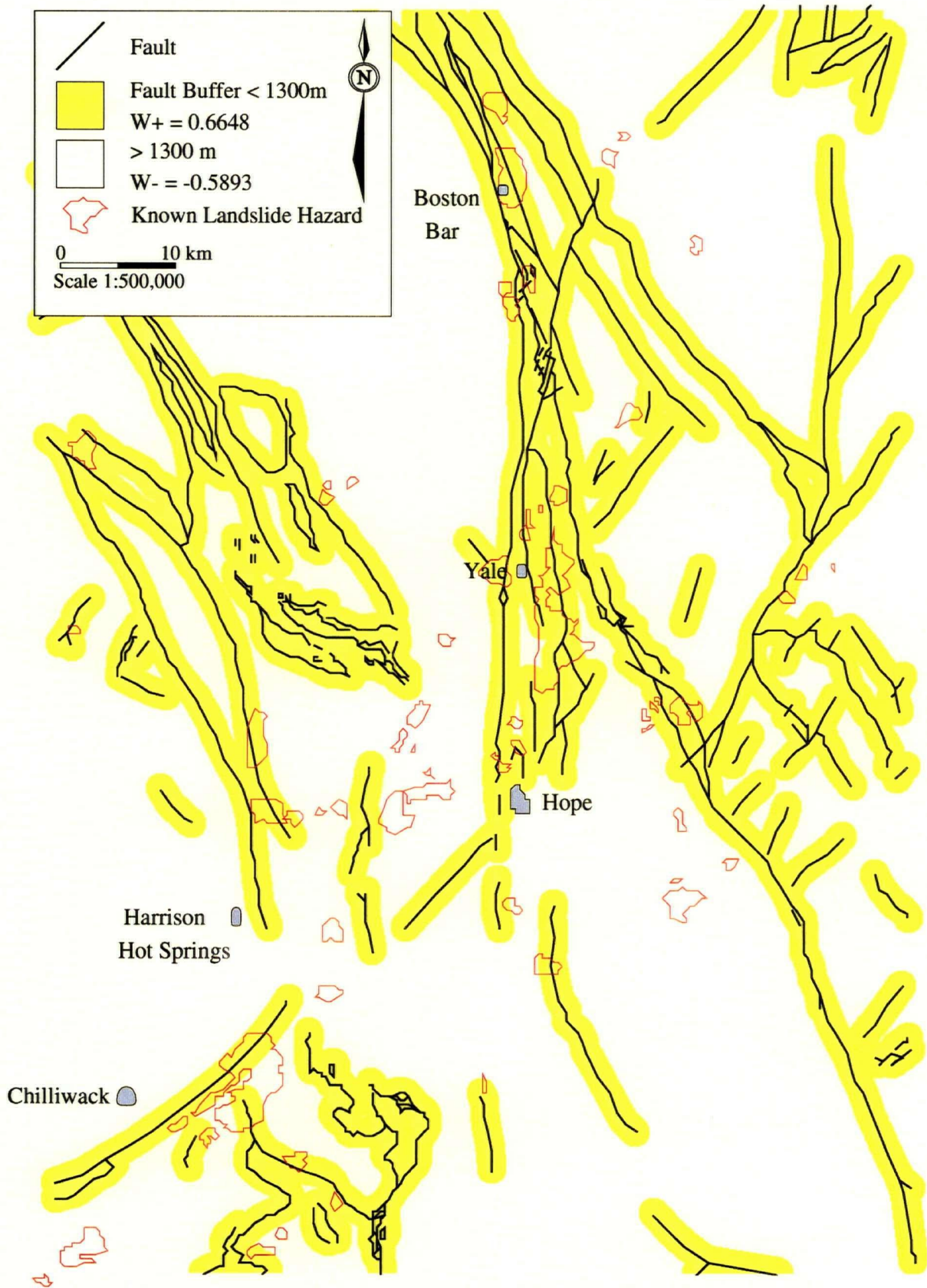


Figure 5.3. Fault buffers with faults and landslide hazards superimposed.

northeast corner of the lineaments predictor map because airphoto coverage was not available and lineaments were not collected there.

### 5.5 Conditional Independence

Conditional independence is assumed to exist when combining two or more maps with Bayesian models, such as weights of evidence. In practice, conditional independence is always violated to some degree so the pairwise test (Bonham-Carter 1994b) is used to check the severity of violation. Two binary maps  $B_1$  and  $B_2$  are conditionally independent with respect to landslides  $S$  when:

$$N\{B_1 \cap B_2 \cap S\} = \frac{N\{B_1 \cap S\} \cdot N\{B_2 \cap S\}}{N\{S\}} \quad (5.1)$$

In words, if the observed number of landslide cells (left-hand side of the equation) is significantly different than the expected (or theoretical) number of landslide cells (right-hand side of the equation) then the two binary maps are not conditionally independent. The pairwise test uses contingency tables and  $X^2$  (chi-square) to quantify the degree of conditional independence between all possible pairings of binary maps (Bonham-Carter 1994b). A large value of  $X^2$  results from the observed area being greater or less than the expected area. In this study the response variable (landslides) is measured in terms of an area rather than a point (i.e. mineral occurrences). Consequently chi-square values only provide a relative measure of spatial correlation because  $X^2$ , being sensitive to units of measurement, produces wildly different values than those tabled. A better indicator, Cramer coefficient, which depends on  $X^2$  and the total area of the landslides, is normalized and is not affected by units. Cramer coefficient  $V$  is defined as

$$V = \sqrt{\frac{X^2}{N\{S\}}} \quad (5.2)$$

where  $N\{S\}$  is the total slide area. The magnitude of  $V$  varies from 0 (independence) to 1 (dependence) and is used here to quantify the relative degree conditional independence between maps. The results are presented in Table 5.3.

The largest  $V$  value coincides to the Spuzzum Pluton and faults association. Inspecting the data reveals at the intersection of the Spuzzum Pluton and the fault buffer the expected number of landslide

Map	Lineaments	Faults	20°-30° Slopes	30°-40° Slopes	40°-50° Slopes	>50° Slopes	Average
<b>Lineaments</b>		0.1224	0.0549	0.0824	0.0318	0.0600	0.0767
<b>Faults</b>			0.0511	0.0284	0.0059	0.0339	0.0339
<b>Custer Gneiss</b>	0.1236	0.2153	0.0268	0.0256	0.0093	0.0221	0.0983
<b>Chilliwack Group</b>	0.0472	0.1208	0.0315	0.0473	0.0079	0.0331	0.0616
<b>Cultus Formation</b>	0.1724	0.1819	0.0034	0.0451	0.1598	0.0959	0.1182
<b>Spuzzum Pluton</b>	0.0369	0.3762	0.0659	0.0613	0.0432	0.0576	0.1760
<b>Slollicun Schist</b>	0.0896	0.0311	0.0062	0.0831	0.0578	0.0585	0.0542
<b>Peninsula Formation</b>	0.0180	0.1172	0.1008	0.0638	0.0392	0.0725	0.0834
<b>Ultramafic, gabbro</b>	0.1336	0.1018	0.0038	0.0646	0.0340	0.0422	0.0592
<b>Dewdney Creek Fm.</b>	0.0787	0.0774	0.0485	0.0393	0.0641	0.0517	0.0577
<b>Ultramafic, gabbro</b>	0.0935	0.0712	0.0584	0.0710	0.0448	0.0591	0.0617
<b>Hozameen Complex chert, pelite,</b>	0.1054	0.0582	0.0422	0.0517	0.0957	0.0674	0.0656
<b>Hozameen Complex volcanics</b>	0.0901	0.0628	0.0646	0.0571	0.0476	0.0569	0.0581
<b>Billhook Creek Fm.</b>	0.0875	0.0619	0.0562	0.0634	0.0575	0.0591	0.0597
<b>Jackass Mountain Group</b>	0.0936	0.0700	0.0292	0.0380	0.0086	0.0281	0.0402
<b>Average</b>	0.0982	0.1471	0.0501	0.0574	0.0609	0.0563	0.0828

**Table 5.3.** Values of Cramer coefficient  $V$  for quantifying conditional independence between lineaments, faults, selected geology and slope maps.

cells is greater than observed by a factor of 10. This is reasonable as two strong predictors like faults and the Spuzzum Pluton should, when intersected, have high landslide occurrence and the expected number of landslides should be high. In the field there is a low observed occurrence at the intersection of both maps suggesting landslide occurrence is more related to the Spuzzum Pluton than the nearby faults. Although an interesting speculation, this conditional dependence between the Spuzzum Pluton and the faults has should be removed by combining the two maps into one and calculating a new weight. If this is not done then the posterior probability map will over-predict the number of landslide occurrences where the Spuzzum Pluton and faults maps intersect.

The second largest  $V$  value is the Custer Gneiss and faults association. This correlation is the exact opposite of the Spuzzum Pluton/Faults association. Where both binary maps are present the theoretical number of landslide cells is less than the observed number. This correlation is not surprising since the 1300 m wide fault buffer covers most of the Custer Gneiss, eliminating many locations where landslides can exclusively intersect the Custer Gneiss. The Custer Gneiss and the faults buffer are almost the same binary map. If the binary maps are not combined then the posterior probability map will over-predict the number of landslide occurrences where the Custer Gneiss and faults maps intersect.

Relative to the averages, values of  $V$  indicate no other serious problems of conditional independence occur between the binary predictor maps. Overall the faults predictor map shows a slight correlation with the other maps but the magnitude (0.14) does not warrant removing it from the posterior map calculations.

## 5.6 Results

From the weights in Table 5.4 it is clear that the presence of the Custer Gneiss, faults, lineaments, Chilliwack and Cultus formations increases the probability of landslide presence, whereas the presence of the plutonic contacts and slopes less than  $20^\circ$  are negative factors.

For most of the predictor maps, the presence of a pattern has more influence than the absence of the pattern. For example regions where the Custer Gneiss is present score very strongly, but regions

Binary Map	W+	s(W+)	W-	s(W-)	C	s(C)	C/s(C)
Custer Gneiss	1.7732	0.0220	-0.1174	0.0081	1.8906	0.0235	80.5926
Faults (< 1300 m)	0.6648	0.0097	-0.5893	0.0123	1.2541	0.0157	80.0665
Lineaments (< 1200 m)	0.4012	0.0080	-1.4462	0.0248	1.8474	0.0260	70.9965
Chilliwack Group	1.5737	0.0259	-0.0778	0.0080	1.6514	0.0271	61.0072
Cultus Formation	1.4190	0.0297	-0.0550	0.0079	1.4740	0.0307	48.0142
Spuzzum Pluton	1.0960	0.0244	-0.0719	0.0080	1.1679	0.0257	45.5322
Stollicun Schist	0.9843	0.0285	-0.0482	0.0079	1.0325	0.0296	34.8816
Slopes 40°-50°	0.8766	0.0306	-0.0387	0.0078	0.9153	0.0316	29.0037
Peninsula Formation	1.2024	0.0521	-0.0158	0.0077	1.2182	0.0526	23.1433
Slopes 30°-40°	0.3662	0.0172	-0.0720	0.0085	0.4382	0.0192	22.8456
Ultramafic, gabbro	1.2297	0.0598	-0.0121	0.0076	1.2418	0.0603	20.5873
Slopes 20°-30°	0.2038	0.0131	-0.0901	0.0093	0.2939	0.0161	18.3122
Dewdney Creek Formation	0.5108	0.0319	-0.0241	0.0078	0.5348	0.0328	16.2967
Ultramafic, gabbro	2.0142	0.1303	-0.0033	0.0076	2.0175	0.1305	15.4595
Hozameen Complex; chert, pelite,..	0.1977	0.0259	-0.0167	0.0079	0.2144	0.0271	7.9087
Hozameen Complex; volcanics	0.2576	0.0416	-0.0078	0.0077	0.2655	0.0423	6.2787
Billhook Creek Formation	0.7895	0.1559	-0.0013	0.0076	0.7909	0.1561	5.0663
Slopes >50°	0.2694	0.1194	-0.0010	0.0076	0.2704	0.1197	2.2596
Jackass Mountain Group	0.1402	0.0802	-0.0012	0.0076	0.1414	0.0806	1.7547
Plutonic Contacts (< 300 m)	-0.0954	0.0260	0.0094	0.0079	-0.1048	0.0272	-3.8580
Slopes 0°-10°	-0.2829	0.0187	0.0661	0.0083	-0.3489	0.0205	-17.0505
Slopes 10°-20°	-0.2968	0.0156	0.1120	0.0087	-0.4089	0.0179	-22.8868

**Table 5.4.** Positive and negative weights, sample variances, and contrast for all predictor maps. Maps are ranked by the Studentized value of contrast  $C/s(C)$ .

where it is absent are not strongly downweighted. Conversely, notice that the absence of lineaments cause a significant downweighting.

Apart from the Custer Gneiss and plutonic contacts, the strong positive binary maps predicted by the weights of evidence model are the same as those proposed by Savigny (1995). Three of the top four formations are composed of weak metamorphosed sediments including amphibolite, pelite, sandstone, conglomerate, carbonate, and argillite. The presence of bedded sandstone and conglomerate suggest that the landslides may be more structurally controlled than previously thought. Although considered a massive rock from an engineering standpoint, the Custer Gneiss, as seen in the conditional probability test, may be a weak rock because of the spatial association with faults and pelitic schist.

The fault and lineaments thresholded at 1300 m and 1200 m respectively. These corridors of optimal influence agree with field observation of fracture density near faults. Field evidence suggested that discontinuities near faults were more common and more closely spaced within one kilometer of the fault (Savigny 1995).

Finally, in this study, weights of evidence suggests that the steeper the slope the more likely a landslide will be present. This is expected from a physical standpoint. In the future, slopes, elevations, and landslide occurrence can be spatially correlated to investigate the relationship between landslide occurrence and glacial stress relief.

To calculate the posterior odds of landslide occurrence  $O(S|B_n)$ , the GIS adds the weights of predictor maps  $B_j$ ,  $j = 1, 2, 3, \dots, n$  to the prior odds using the expression:

$$O(S|B_1^k \cap B_2^k \cap B_3^k \dots B_n^k) = e^{\sum_{j=1}^n w_j^k + \log_e \left( \frac{N\{S\}}{N\{T\} - N\{S\}} \right)} \quad (5.3)$$

where the superscript  $k$  refers to the presence (+) or absence (-) of binary pattern  $j$  and  $N\{T\}$  and  $N\{S\}$  refers to the area of the study area and landslides, respectively (Bonham-Carter *et al.* 1989). Negative weights ( $W^-$ ) are not used for the geology and slope multiclass maps because each class is mutually exclusive. For example, the negative weight ( $W^- = -0.0901$ ) is not used for areas where  $20^\circ$  to  $30^\circ$  slopes are not present because another slope class, say  $30^\circ$  to  $40^\circ$ , is present.

Posterior probability is calculated using

$$P = \frac{O}{(1 + O)} \quad (5.4)$$

and the resulting map is shown in Figure 5.4. The map shows six probability classes ranging from less than 2% (the prior probability) to greater than 40 % probability of a landslide being present per hectare.

The highest probabilities occur within 1300 m of fault, 1200 m of a lineament and along the steeper slopes where the strong indicator rocks (i.e. Custer Gneiss, Custer and Cultus Formations) occur. The Fraser Canyon near Yale, the slopes above Chilliwack and the upper Chilliwack Valley, and adjacent to the Ross Lake Fault south of Hope are three areas that have high probability of landslide occurrence. The reader is reminded that this map is the result of a methodology and not rigorous interpretation and therefore should not be used for planning purposes.

Probabilities are best used in a relative sense rather than absolute because of the problems associated with an “area type” response variable (Bonham-Carter 1994b). In the future landslide studies, rather than using landslide polygons that represent the initiation, transportation and deposition zones, landslide polygons should be contracted to a single pixel that represents the point of landslide initiation. Nevertheless, these objective zones of probability are extremely useful for landslide hazard zoning. Areas of known and unknown landslide hazard can be ranked on the basis of the geology, landuse, and other landslide model criteria and combined with socio-economic rules and run-out models to create a map of landslide risk.

Uncertainty in the post probability map is checked by calculating post probability variances and determining zones where the studentized posterior probability ( $P_{\text{post}}/S_{\text{total}}$ ) is less than 1.5 (Bonham-Carter *et al.* 1989). No zones of uncertainty matching this criteria were found.

## 5.7 Conclusions

- 1) Weights of evidence modelling provides a simple objective statistical method for predicting landslide potential for regions where a number of representative landslide occurrences are known. The objective weights are straightforward to interpret; an estimate of uncertainty can be made, both using the variances of the weights and the variance due to missing or incomplete data. The

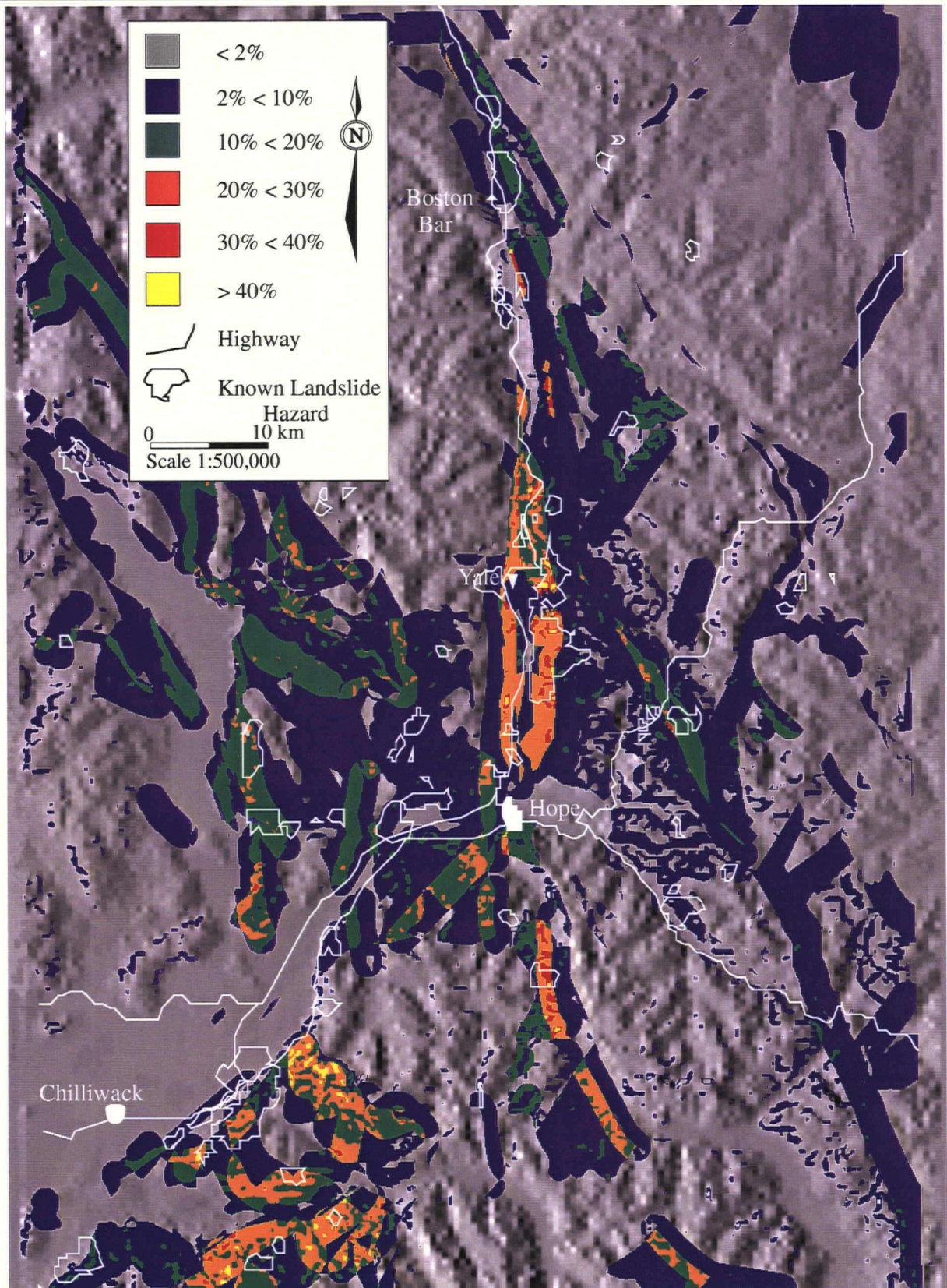


Figure 5.4. Posterior probability map of landslide occurrence per hectare. Known landslide occurrences are outlined in white.

method is particularly well-suited for modelling structural information such as proximity to linear features, as well as slope, elevation and bedrock geology. A raster based GIS, such as IDRISI or SPANS, is excellent software for building the database, modelling, and visualizing the results.

- 2) The top five predictor maps in order of their importance for predicting known large rock landslide occurrence in the Hope study area are: 1) presence of Custer Gneiss; 2) within 1300 m of a fault trace; 3) within 1200 m of a lineament; 4) presence of Cultus Formation; 5) presence of Chilliwack Formation; 5) presence of Spuzzum Pluton. The proximity to a plutonic contact and slopes less than 20° are not positive predictors of landslide occurrence. Apart from the Custer Gneiss and the plutonic contacts, these results agree with field observation made by Savigny (1995).
- 3) A map of posterior probability of large rock landslide occurrence was created for the Hope study area. Areas of relative high landslide occurrence include the Fraser Canyon near Yale, the slopes above Chilliwack and the upper Chilliwack Valley, and adjacent to the Ross Lake Fault south of Hope.
- 4) Since weights of evidence is better suited for point objects as the response variable, future studies should use points of landslide initiation instead of landslide polygons. If point objects are used conditional independence tests using chi-squares and posterior probabilities may be interpreted on an absolute rather than relative basis.
- 5) In the future, adding the posterior probability map with socio-economic criteria and landslide runout models within a GIS is a useful technique for creating landslide risk maps. Risk maps provide essential information for development planning in mountainous terrain.
- 6) In the Hope area future detailed studies include investigating the relationships between landslide occurrence and; 1) different fault mechanisms (i.e. ductile and mechanically brecciated); 2) orientations of bedding, foliation, structure, and geologic contacts; and 3) elevation.

## CHAPTER 6

### Conclusions

This research was undertaken to demonstrate the use of airborne SAR and GIS for mapping and managing large rock landslides in the Hope study area in southwestern British Columbia. The utility of SAR for lineament and landslide hazard mapping was compared to airphotos. Based on an airphoto inventory of landslides and lineaments, spatial relationships between regional faults, lineaments, plutonic contacts, and pendant rocks and landslide hazard occurrence proposed by Savigny (1995) were explored using a GIS and an objective statistical methodology called weights of evidence.

Landslides in the Hope study area are predominantly large volume ( $> 1$  million  $m^3$ ), prehistoric rock slump, or rock block slides, occurring along faults, joints, and bedding planes. They exhibit subdued morphology obscured by uniform vegetation and are best located in remotely sensed imagery using morphological rather than spectral characteristics. Morphological indicators useful for landslide identification include scarps, ground cracks, bulges and depressions, hummocky debris, offset stream courses. Spectral indicators, such as vegetation contrast, tonal changes, and slope ponding are less useful in this study area. A high resolution remote sensing tool with stereo capability and/or sensitive to morphological change, such as airborne SAR, is required for proper landslide hazard mapping in this study area.

Lineaments in the Chilliwack study area were located and digitized on-screen using geocoded 1:20,000, 1:50,000, and 1:80,000 scale C-band SAR and compared to 1:50,000 scale black and white airphotos. SAR lineament length and trend correlate well with lineaments found in airphotos. As with airphotos, as SAR image scale increases observed lineament frequency increases and lineament length

decreases. SAR lineament length and trend are less sensitive to changes in scale than airphoto lineaments.

The ability of SAR imagery to locate specific airphoto lineaments was tested. 1:50,000 scale SAR located the most airphoto lineaments (39%). SAR tends to enhance the longer airphoto lineaments. It was expected that SAR would locate most of the airphoto lineaments within the 030° to 070° enhancement zone. This was not the case. In fact, this zone missed more airphoto lineaments than any other. Since 53% (88 out of 165) of the SAR lineaments are not airphoto lineaments, most of the lineaments found with SAR provide additional structural information about the Chilliwack area.

The Savigny (1995) lineaments are, on average, longer and trend considerably more east-west than the author's airphoto and SAR lineaments. The author's airphoto and SAR lineament data are a close match compared to the Savigny airphoto lineaments suggesting that the differences are likely caused by interpreter biases rather than the imaging tools. The Chilliwack SAR lineaments were not used in the GIS hazard analysis since the differences in length and trend are substantial and the SAR lineaments would contaminate the regional Savigny lineament database.

Landslide hazard mapping was done using black and white stereo aerial photographs and the results were quantitatively compared to equivalent scale 10 m resolution SAR imagery. SAR imagery is a very useful tool for detecting landslide hazard features that have geomorphological characteristics. Such features include, lineaments, antislope scarps, deformation zones, and especially hummocky debris lobes, cone and fans.

Despite a lower resolution than airphotos, SAR detected all of the major features seen in airphotos. In areas masked by anthropogenic features such as logging and cultivation, SAR proved more useful in revealing landslide debris and lineaments. In areas covered by mature forest SAR detects subtle changes in ground morphology by detecting the corresponding changes in tree canopy height. Airphoto stereo is not as sensitive to changes in tree canopy height.

The outward radial pattern typical of rock avalanche debris was easily defined in SAR imagery. Analysis of this radial pattern helps locate the source and determine mechanics of the slide. Depending

on the viewing geometry SAR is able to detect hazard source zones not apparent in stereo airphotos while in other circumstances features are more easily detected by analyzing aerial photographs.

Weights of evidence modelling provides a simple objective statistical method for predicting landslide potential for regions where a number of representative landslide occurrences are known. The objective weights are straightforward to interpret; an estimate of uncertainty can be made, both using the variances of the weights and the variance due to missing or incomplete data. The method is particularly well-suited for modelling structural information such as proximity to linear features, as well as slope, elevation and bedrock geology. A raster based GIS, such as IDRISI or SPANS, is excellent software for building the database, modelling, and visualizing the results.

The top five predictor maps in order of their importance for predicting known large rock landslide occurrence in the Hope study area are: 1) presence of Custer Gneiss; 2) within 1300 m of a fault trace; 3) within 1200 m of a lineament; 4) presence of Cultus Formation; 5) presence of Chilliwack Formation. The proximity to a plutonic contact and slopes less than  $20^\circ$  are not positive predictors of landslide occurrence. Apart from the Custer Gneiss and the plutonic contacts these results agree with field observations by Savigny (1995).

A map of posterior probability of large rock landslide occurrence was created for the Hope study area. Areas of relative high landslide occurrence include the Fraser Canyon near Yale, the slopes above Chilliwack and the upper Chilliwack Valley, and adjacent to the Ross Lake Fault south of Hope.

Since weights of evidence is better suited for point objects as the response variable, future studies should use points of landslide initiation instead of landslide polygons. If point objects are used conditional independence tests using chi-squares and posterior probabilities may be interpreted on an absolute rather than a relative basis.

In the future, adding the posterior probability map with socio-economic criteria and landslide runoff models within a GIS is a useful technique for creating landslide risk maps. Risk maps provide essential information for development planning in mountainous terrain.

In the Hope area future detailed studies include investigating the relationships between landslide occurrence and; 1) different fault mechanisms (i.e. ductile and mechanically brecciated); 2) orientations of bedding, foliation, structure, and geologic contacts; and 3) elevation.

## REFERENCES

- Agterberg, F.P. 1989. Systematic approach to dealing with uncertainty of geoscience information in mineral exploration. Proceedings, Twenty-first Applications of Computers and Operations Research in the Mineral Industry (APCOM) Symposium, Las Vegas, February 27-March 2, Chapter 18, pp. 165-178.
- Agterberg, F.P., Bonham-Carter, G.F., and Wright, D.F. 1990. Statistical pattern integration for mineral exploration. Proceedings, COGEO DATA Symposium on Computer Applications in Resource Exploration, July 1988, Espo, Finland, Pergamon Press, pp. 1-21.
- Bonham-Carter, G.F., Agterberg, F.P., and Wright, D.F. 1989. Weights of evidence modelling: a new approach to mapping mineral potential. Statistical Applications in Earth Sciences, ed. F.P. Agterberg and G.F. Bonham-Carter, Geological Survey of Canada, Paper 89-9, pp. 171-183.
- Bonham-Carter, G.F., Agterberg, F.P., and Wright, D.F. 1988. Integration of geological datasets for gold exploration in Nova Scotia. Photogrammetric Engineering and Remote Sensing, Vol. 54, No. 11, pp. 1585-1592
- Bonham-Carter, G. F. 1994a. Geographic Information Systems for Geoscientists: Modelling with GIS. Pergamon Press, Elsevier Science Inc., Tarrytown, New York, pp. 398.
- Bonham-Carter, G. F. 1994b. When to use weights of evidence method for map data. Proceedings of Workshop Mcaulay Land Use Research Institute, Aberdeen, September, pp. 1-15.
- Brass, A., Wadge, G., and Reading, A.J. 1991. Designing a GIS for the prediction of landsliding potential in the West Indies. Neotectonics and Resources, Cosgrove, J. and Jones, M., editors, London, Belhaven Press, pp. 220-230.
- Carrara, A., Cardinali, M., Detti, R., Guzzetti, F., Pasqui, V., and Reichenbach, P. 1991. GIS techniques and statistical models in evaluating landslide hazard. Earth Surface Processes and Landforms, Vol. 16, pp. 427-445.
- Cavers, D. 1992. Popkum Slide. *in* Technical Tour No. 2, Fraser Valley and Fraser Canyon Areas, Technical Tours Guidebook, Bitech Publishers Ltd., GeoHazards '92, Vancouver, Canada, May 6 -9, pp. 66.
- Clague, J.J. and Luternauer, J.L. 1983. Late Quaternary geology of southwestern British Columbia. Geological Association of Canada, Mineralogical Association of Canada, Canadian Geophysical Union, Joint Annual Meeting (Victoria, British Columbia, Canada), Field Trip Guidebook, No. 6, 112 p.

- Colwell, R.N. 1983. *Manual of Remote Sensing*, 2nd Edition, Vol. 1&2, American Society of Photogrammetry, Falls Church, V.A., pp. 429-474.
- Cruden, D.M. 1976. Major rock slides in the Rockies. *Canadian Geotechnical Journal*, Vol. 13, No. 1, pp. 8-20.
- Dekker, F., Balkwill, H., Slater, A., Herner, R., and Kampschuur, W. 1989. Hydrocarbon exploration through remote sensing and fieldwork in the onshore eastern Papuan fold belt, Gulf Province, Papua New Guinea. *Proceedings, Seventh Thematic Conference on Remote Sensing for Exploration Geology*, Calgary, Alberta, Canada, October 2-6, pp. 65-80.
- Eastman, J.R. 1993. *IDRISI: A raster based Geographic Information System. Users Guides*, Version 4.1, rev. 0, Graduate School of Geography, Clark University, Worcester, Massachusetts, U.S.A.
- Eisbacher, G.H. 1979. Cliff collapse and rock avalanches (sturzstroms) in the Mackenzie Mountains, northwestern Canada. *Canadian Geotechnical Journal*, Vol. 16, No. 2, pp. 309-334.
- Ellen, S.D., Mark, R.K., Cannon, S.H., and Knifong, D.L. 1993. Map of debris flow hazard in the Honolulu District of Oahu, Hawaii. *U.S. Geological Survey Open-File Report 93-213*, 25 p.
- Evans, D.L. 1992. Geologic process studies using synthetic aperture radar (SAR) data. *Episodes*, Vol. 15, No. 1, pp. 21-31.
- Evans, S.G. 1984a. The landslide response of tectonic assemblages in the southern Canadian Cordillera. *Proceedings, 4th International Symposium on Landslides*, Vol. 1, pp. 495-502.
- Evans, S.G. 1984b. Landslides in Tertiary basaltic successions. *Proceedings, 4th International Symposium on Landslides*, Vol. 1, pp. 503-510.
- Evans, S.G. 1986. Landslide damming in the Cordillera of western Canada. *Landslide Dams: Processes, Risk and Mitigation*, (ed.) R.L. Schuster; American Society of Civil Engineers, Geotechnical Special Publication, No. 3, pp. 111-130.
- Everard, K.E. 1994. Regional characterization of large landslides in southwest Yukon, with emphasis on the role of neotectonics. Unpublished M.A.Sc. thesis, Geological Engineering Program, Department of Geological Sciences, The University of British Columbia, Vancouver, Canada, 165 p.

- Feder, A.M. 1986. Selected comparisons of aircraft-borne and orbital imaging radar data and their geologic significance. Contributions to the Geology of South Texas, ed. Wilford Lee Stapp, The South Texas Geological Society, San Antonio, Texas, U.S.A., pp. 10-23.
- Gerath, R.F., Hungr, O., and VanDine, D.F. 1994. Landslide hazard mapping guidelines for British Columbia. Report to The Earth Sciences Task Force, B.C. Government Resources Inventory Committee. Draft report prepared by Thurber Engineering Ltd., Vancouver, B.C. in association with VanDine Geological Engineering.
- Gibbins, W.A. and Slaney, V.R. 1991. Preliminary geologic interpretation of SAR data, Yellowknife-Hearne Lake area, N.W.T. Arctic, Vol. 44, Supp. 1, pp. 81-93.
- Goodacre, A., Bonham-Carter, G.F., Agterberg, F.P., and Wright, D.F. 1993. A statistical analysis of the spatial association of seismicity with drainage patterns and magnetic anomalies in western Quebec. Tectonophysics, Vol. 217, pp. 205-305.
- Graham, D.F. and Grant, D.R. 1991. A test of airborne, side-looking synthetic-aperture radar in central Newfoundland for geological reconnaissance. Canadian Journal of Earth Science, Vol. 28, pp. 257-265.
- Gupta, R.P. and Joshi, B.C. 1990. Landslide hazard zoning using the GIS approach - A case study from the Ramganga Catchment, Himalayas. Engineering Geology, Vol. 28, pp. 119-132.
- Hansen, A. and Franks, C.A.M. 1991. Characterization and mapping of earthquake triggered landslides for seismic zonation. Proceedings, EERI Fourth International Conference on Seismic Zonation, State-of-the-art-papers, pp. 149-195, Stanford, California, U.S.A.
- Harris, J.R. 1984. Lineament mapping of central Nova Scotia using Landsat-MSS and Seasat-SAR imagery. Proceedings, Ninth Canadian Symposium on Remote Sensing, St. John's, Newfoundland, Canada, pp. 359-373.
- Harris, J.R., Bonham-Carter, G.F., Rencz, A.N., Sangster, A.L., and Bretzlaff, R. 1987. Lineament analysis of Cobequid Highlands, Nova Scotia, using Seasat, Landsat and SPOT data. Proceedings, Eleventh Canadian Symposium on Remote Sensing, Waterloo, Ontario, Canada, June 22-25, pp. 311-327.
- Harris, J.R. 1991. Mapping of regional structure of eastern Nova Scotia using remotely sensed imagery: Implications for regional tectonics and gold exploration. Canadian Journal of Remote Sensing, Vol. 17, No. 2, pp. 122-135.

- Hutchinson, J.N., 1988. General Report: Morphological and geotechnical parameters of landslides in relation to geology and hydrogeology. Proceedings, Sixth International Symposium on Landslides, Lausanne, France, July 10-15, pp. 3-35.
- Kenny, F.M., Singhroy, V.H., and Barnett, P.J. 1994. Integration of SPOT panchromatic, ERS-1, and digital elevation data for terrain and surficial mapping. Proceedings, Tenth Thematic Conference on Geologic Remote Sensing, San Antonio, Texas, U.S.A., May 9-12, pp. 503-516.
- Knapp, K.R., Morgan, K.M., Donovan, N., Busbey, A., and Kresic, N. 1994. Using SPOT and TM to map fractures related to groundwater resources in the Slick Hills of Oklahoma. Proceedings, Tenth Thematic Conference on Geologic Remote Sensing, San Antonio, Texas, U.S.A., May 9-12, pp. 155-160.
- Kotyukh, A.A. and Monakhov, A.K. 1990. Comparative analysis of features on radar imagery and aerial photographs in desert and mountainous landscapes. Mapping Sciences and Remote Sensing, Vol. 27, No. 1, pp. 9-15.
- Lattman, L.H. 1958. Technique of mapping geological fracture traces and lineaments on aerial photographs. Photogrammetric Engineering, Vol. 24, No. 4, 568-576.
- Leir, M. C. 1994. TREND, a FORTRAN77 program for calculating lineament trends from coordinate endpoint ASCII data. Unpublished computer code, Department of Geological Sciences, The University of British Columbia, Vancouver, British Columbia, Canada.
- Lillesand, T.H. and Kiefer, R.W. 1994. Remote Sensing and Image Interpretation. John Wiley & Sons, Inc. Toronto, Canada, pp. 648-729.
- Livingstone, C.E., Gray, A.L., Hawkins, R.K., Olsen, R.B., Halbertsma, J.G., and Deane, R.A. 1987. CCRS C-Band airborne radar: System description and test results. Proceedings, Eleventh Canadian Symposium on Remote Sensing, University of Waterloo, Waterloo, Ontario, Canada, June 22-25, pp. 503-518.
- Mason, P.J., Liu, J.G., and Moore, J.M. 1994. Integration of Landsat TM with SPOT Panchromatic and ERS-1 SAR imagery for neotectonic studies. Proceedings, Tenth Thematic Conference on Geologic Remote Sensing, San Antonio, Texas, U.S.A., May 9-12, pp. 253-261.
- McFall, G.H. and Singhroy, V.H. 1989. Remote sensing applications to neotectonic studies in southern Ontario, Canada. Proceedings, Seventh Thematic Conference on Remote Sensing for Exploration Geology, Calgary, Alberta, Canada, October 2-6, pp. 111-126.

- McKean, J., Buechel, S., and Gaydos, L. 1991. Remote sensing and landslide hazard assessment. Proceedings, Eighth Thematic Conference on Geologic Remote Sensing, Denver, Colorado, USA, April 29-May 2, pp. 729-742.
- McTaggart, K.C. and Thompson, R.M. 1967. Geology of part of the northern Cascades in southern British Columbia. Canadian Journal of Earth Sciences, Vol. 4, pp. 1119-1228.
- Mejía-Navarro, M., Wohl, E.E., and Oaks, S.D. 1994. Geological hazards, vulnerability, and risk assessment using GIS: model for Glenwood Springs, Colorado. Geomorphology, Vol. 10, pp. 331-354.
- Mejía-Navarro, M. and Wohl, E.E. 1994. Geological hazard and risk evaluation using GIS: methodology and model applied to Medellín, Columbia. Bulletin of the Association of Engineering Geologists, Vol. 31, No. 4, pp. 459-481.
- Misra, K.S., Slaney, V.R., Graham, D., and Harris J. 1991. Mapping of basement and other tectonic features using SEASAT and thematic mapper in hydrocarbon-producing areas of the western sedimentary basin of Canada. Canadian Journal of Remote Sensing, Vol. 17, No. 2, pp. 137-151.
- Mollard, J.D. 1988. First R.M. Hardy memorial lecture: Fracture lineament research and applications on the western Canadian plains. Canadian Geotechnical Journal, Vol. 25, No. 4, pp. 749-767.
- Monger, J.W.H. 1970. Hope map-area, west half (92H W1/2), British Columbia: Geological Survey of Canada, Paper 69-47.
- Monger, J.W.H. 1985. Structural evolution of the southwestern Intermontane Belt, Ashcroft and Hope map-areas, British Columbia; *in* Current Research, Part A, Geological Survey of Canada, Paper 85-1A, pp. 349-358.
- Monger, J.W.H. 1989. Geology of Hope map area, British Columbia. Geological Survey of Canada, Maps 41-1989, sheet 1, scale 1:250,000.
- Monger, J.W.H. 1991. Cascade segment of the Coast Belt. Structural styles, Chapter 17 *in* Geology of the Cordilleran Orogen in Canada, H. Gabrielse and C.J. Yorath (ed.), Geological Survey of Canada, Geology of Canada, No. 4, pp. 588-591 (also Geological Society of America, The Geology of North America, Vol. G-2).
- Moon, W.M., Won, J.S., Li, B., Slaney, V.R., and Lamontagne, M. 1991. Application of airborne C-SAR and SPOT image data to the geological setting of the Nahanni earthquake area. Canadian Journal of Remote Sensing, Vol. 17, No. 3, pp. 272-278.

- Moore, D.P., Ripley, B.D., and Groves, K.L. 1992. Evaluation of mountainslope movements at Wahleach *in* Geotechnique and Natural Hazards, Bitech Publishers, Vancouver, British Columbia, pp. 99-107.
- Mussakowski, R., Trowell, N.F., and Heather, K.B. 1991. Digital integration of remote sensing and geoscience data for the Goudreau-Lochalsh area, Wawa, Ontario. Canadian Journal of Remote Sensing, Vol. 17, No. 2, pp. 162-173.
- Naumann, C. M. 1990. The Cheam Slide: A study of the interrelationship of rock avalanches and seismicity. Unpublished M.A.Sc. thesis, Geological Engineering Program, Department of Geological Sciences, The University of British Columbia, Vancouver, Canada, 203 p.
- Naumann, C. M. and Savigny, K.W. 1992. Large rock avalanches and seismicity in southwestern British Columbia, Canada. Proceedings, Sixth International Symposium on Landslides, Christchurch, New Zealand, February 10-14, pp. 1187-1192.
- Nilsen, T.H. and Brabb, E.E. 1977. Slope-stability studies in the San Francisco Bay Region, California. Reviews in Engineering Geology, Vol. 3, D.R. Coates (ed.), pp. 235-243. The Geological Society of America.
- Paradella, W.R., Liu, C.C., Veneziani, P., dos Santos, A.R., Bignelli, P.A., and Dias, R.R. 1994. An overview of SAREX'92 (South American Radar Experiment) data acquisition and preliminary results from Carajas mineral province (Brazilian amazon region). Proceedings, Tenth Thematic Conference on Geologic Remote Sensing, San Antonio, Texas, U.S.A., May 9-12, pp. 214-225.
- Parrish, R.R. 1983. Cenozoic thermal evolution and tectonics of the Coast Mountains, British Columbia  
1. Fission track dating apparent uplift rates and pattern of uplift; Tectonics, Vol. 2, pp. 601-631.
- PCI Inc. 1992. Using PCI Software, Software Manuals, Version 5.1 EASI/PACE, Richmond Hill, Ontario.
- Pearson, E.J., Wadge, G. and Wislocki, A. P. 1991. Mapping natural hazards with spatial modelling systems. Proceedings, EGIS'91 Conference, Brussels, Belgium, April 2-5, pp. 847-855.
- Piteau, D. 1977. Regional slope-stability controls and engineering geology of the Fraser Canyon, British Columbia. Reviews in Engineering Geology, Vol. 3, D.R. Coates (ed.), pp. 85-112. The Geological Society of America.

- Posehn, G.A. and Genereux, J.A. 1991. The application of synthetic aperture radar to hydrocarbon exploration in the glaciated and boreal forested terrain of northeast British Columbia, Canada. Proceedings, Eighth Thematic Conference on Geological Remote Sensing, Denver, Colorado, U.S.A., April 29-May 2, pp. 677-685.
- Premmanee, J. 1989. Lineament mapping from Landsat TM and airborne C-SAR of part of the Sudbury Structure. Proceedings, Seventh Thematic Conference on Geological Remote Sensing for Exploration Geology, Calgary, Alberta, Canada, October 2-6, pp. 997-1010.
- Rengers, N., Soeters, R., and Westen, C.J. van 1992. Remote sensing and GIS applied to mountain hazard mapping. Episodes, Vol. 15, No. 1, pp. 36-45.
- Rib, H.T. and Liang, T. 1978. Recognition and identification. Landslides: Analysis and Control: R.L. Schuster and J.K. Kryzek (eds.), pp. 34-80. Special Report 176, Transportation Research Board, National Research Council, National Academy of Sciences: Washington D.C..
- Roy, D.W., Schmitt, L., Woussen, G., and DuBerger R. 1993. Lineaments from airborne SAR images and the 1988 Saguenay earthquake, Quebec, Canada. Photogrammetric Engineering and Remote Sensing, Vol. 59, No. 8., pp. 1299-1305.
- Sabins, F.F. 1987. Radar images *in* Remote Sensing - Principles and Interpretation. 2nd ed. New York. W.H. Truman & Co. pp. 177-234.
- Savigny, K.W. 1995. Engineering geology of large landslides in the lower Fraser Valley transportation corridor southwestern Canadian Cordillera. Canadian Geotechnical Journal (in press).
- Savigny, K.W. and Leir, M.C. 1995. Sackungen movements in the Hope, Fraser Valley, and Pemberton Regions, Southwestern British Columbia. Installation and monitoring of survey networks 1989 to 1994. Unpublished annual research report, Department of Geological Sciences, The University of British Columbia, Vancouver, Canada.
- Savigny, K.W. and Rinne, N.F. 1991. Assessment of landslide hazards along a pipeline corridor in mountainous terrain of southwestern British Columbia. Distributed at the 44th Canadian Geotechnical Conference, Calgary, Alberta, 19 p.
- Shasko, M.J. and Keller, C.P. 1991. Assessing large scale slope stability and failure within a geographic information system. Proceedings, GIS'91, Vancouver, Canada, February, pp. 319-327.

- Shuman, C.A. 1991. Joints, fracture traces, and lineaments: A multiple scale analysis of fracture features across the Appalachian Plateau in New York. Proceedings, Eighth Thematic Conference on Geologic Remote Sensing, Denver, Colorado, U.S.A., April 4 - May 2, pp. 1229-1241.
- Singhroy, V., Kenny, F.M., and Barnett, P.J. 1992. Radar imagery for Quaternary geological mapping in glaciated terrain. *Canadian Journal of Remote Sensing*, Vol. 18, No. 2, pp. 112-117.
- Singhroy, V., Slaney, R., Lowman, P., Harris, J., and Moon, W. 1993. RADARSAT and radar geology in Canada. *Canadian Journal of Remote Sensing*, Vol. 19, No. 4, pp. 338-351.
- Singhroy, V., Rivard, B., St. Jean, R., and Guindon, B. 1994. Guidelines for enhanced SAR image techniques for geologic applications. Proceedings, Tenth Thematic Conference on Geologic Remote Sensing, San Antonio, Texas, U.S.A., May 9-12, pp. 626-634.
- Spiegelhalter, D.J. and Knill-Jones, R.P. 1984. Statistical and knowledge-based approaches to clinical decision-support systems, with an application in gastroenterology. *Journal of the Royal Statistical Society, A*, Part 1, pp. 35-77.
- Toutin, T., Carbonneau, Y., and St-Laurent, L. 1992. An integrated method to rectify airborne radar imagery using DEM. *Photogrammetric Engineering and Remote Sensing*, Vol. 58, No. 4, pp. 417-422.
- Varnes, D.J. 1978. Slope movement types and processes. *Landslides: Analysis and Control*: R.L. Schuster and J.K. Kryzek (eds.), pp. 11-33. Special Report 176, Transportation Research Board, National Research Council, National Academy of Sciences: Washington, D.C., U.S.A.
- Varnes, D.J. 1984. *Landslide hazard zonation: A review of principles and practice*. Paris, Unesco, International Association of Engineering Geology, Commission on Landslides and Other Mass Movements on Slopes, Natural Hazards, Vol. 3, 176 p.
- van Dijke, J.J. and van Westen, C.J. 1990. Rockfall hazard: a geomorphological application of neighborhood analysis with ILWIS. *ITC Journal*, Vol. 1, pp. 40-44.
- Wadge, G. 1988. The potential of GIS modeling of gravity flows and slope instabilities. *International Journal of Geographic Information Systems*, Vol. 2, No. 2, pp. 143-152.
- Wadge, G., Wislocki, A.P., and Pearson, E.J. 1991. Spatial analysis in GIS for natural hazard assessment. Proceedings, First International Conference/Workshop on Integrating Geographic Information Systems and Environmental Modeling, Boulder, Colorado, September, pp. 1-14.

- Werle, D. 1992. Radar Remote Sensing. A Training Manual. Produced by Dendron Resource Surveys Inc. under contract to Canada Centre for Remote Sensing and distributed by Radarsat International, Ottawa, Ontario, Canada.
- Wheeler, R.L. and Wise, D.U. 1983. Linesmanship and the practice of linear geo-art: Discussion and reply. Geological Society of America Bulletin, Vol. 94, pp. 1377-1379.
- Whitehouse, I.E. and Griffiths, G.A. 1983. Frequency and hazard of large rock avalanches in central southern Alps, New Zealand. Geology, Vol. 11, No. 6, pp. 331-334.
- Wislocki, A.P., and Bentley, S.P. 1991. An expert system for landslide hazard and risk assessment. Computers and Structures, Vol. 40, No. 1, pp. 169-172.
- Wislocki, A.P., Wadge, G., Pearson, E.J., and Whittow, J. 1992. Expert system/geographic information system approaches to planning in areas of instability. Proceedings, The Institute of British Geographers Annual Conference, Swansea, Wales, January.
- Yamaguchi, Y. 1985. Image-scale and look direction effects on the detectability of lineaments in radar images. Remote Sensing of the Environment, Vol. 17, pp. 117-127.
- Yin, K.L. and Yan, T.Z. 1988. Statistical prediction models for slope instability of metamorphosed rocks. Proceedings, Fifth International Symposium on Landslides, Lausanne, Switzerland, July 10-15, Vol. 2, pp. 1269-1272.
- Yong, Z. and Qinghua, Y. 1990. The application of remote sensing images for research of landslides and rockfalls in the area of the Yangtze gorges. Proceedings, Twenty-Third International Symposium on Remote Sensing of Environment, Bangkok, Thailand, April 18-25, pp. 725-728.

APPENDIX I

Summary of the Hope Study Area Geologic History

(Adapted from Monger 1970, 1989)

Period or Epoch	Unit Deposited or Replaced	Group or Formation Name	Tectonic Activity
Quaternary L M E			upwarping and glaciation upwarping and glaciation upwarping and glaciation
Pliocene L M E	volcanics volcanics volcanics	Skagit Formation Skagit Formation Skagit Formation	upwarping upwarping upwarping
Miocene L M E	granodiorite granodiorite granodiorite	Coquihalla Group; Mount Barr Batholith Coquihalla Group; Mount Barr Batholith Coquihalla Group; Mount Barr Batholith	
Oligocene L M E	granodiorite granodiorite granodiorite	Skagit Formation, Coquihalla Group; Chilliwack Batholith Skagit Formation, Coquihalla Group; Chilliwack Batholith Skagit Formation, Coquihalla Group; Chilliwack Batholith	
Eocene L M E	volcanics; sandstone, conglomerate; volcanics; sandstone, conglomerate; granodiorite volcanics; sandstone, conglomerate; granodiorite	Princeton Group; Needle Peak and Mount Ouram Plutons Princeton Group; Needle Peak and Mount Ouram Plutons Princeton Group; Needle Peak and Mount Ouram Plutons	folding and normal and strike slip north-south faulting folding and normal and strike slip north-south faulting folding and normal and strike slip north-south faulting
Paleocene L M E	volcanics volcanics volcanics		
Cretaceous L M E	granodiorite quartz diorite thin marine pelites, sandstones, conglomerates (granitic and gneissic composition); granodiorite	Scuzzy Pluton Spuzzum Pluton Pasayten Group; Eagle Plutonic Complex	orogeny* orogeny* orogeny*
Jurassic L M E	hiatus local pyroclastic and flow volcanics; pelites, siltstones (volcanic composition); marine origin pelites, siltstones (volcanic composition); marine origin	Eagle Plutonic Complex Harrison Lake Formation: Lader Group Lader Group, Cultus Formation	local uplift local uplift
Triassic L M E	local volcanics; hiatus hiatus	Nicola Group; Cultus Formation	upwarping upwarping upwarping
Permian L M E	hiatus hiatus hiatus		upwarping upwarping upwarping
Pennsylvanian L M E	coarser clastics (volcanic and limestone composition); chert coarser clastics (volcanic and limestone composition); chert fine clastics and argillaceous limestone	Chilliwack Group (west); Hozameen Complex (east) Chilliwack Group (west); Hozameen Complex (east) Chilliwack Group (west); Hozameen Complex (east)	upwarping upwarping upwarping
Mississippian L M E			
Devonian L M E	amphibolites, schist		folding, intrusion, and metamorphism

\*Orogeny: 1) Cascade mountains core: gneiss and granite core is sheared and mylonitized.

2) East Cascade mountains: Late Paleozoic to mid-Cretaceous sedimentary and volcanic rocks folded, reverse faulted along the Hozameen, Chuwanien, and Pasayten reverse faults and metamorphosed to greenschist facies.

3) West Cascade mountains: Late Paleozoic to mid-Cretaceous sedimentary and volcanic rocks are folded and thrust to the west and northwest along the Church mountain and Shuksan thrust faults.

### Summary of the Hope study area geologic history (adapted from Monger 1970, 1989)

APPENDIX II

Chilliwack SAR Parameters

Band	C-Band
Presentation	Slant
Polarization	HH
Operational Mode	Narrow Swath
Resolution Mode	High
Pulse Width	38 ns
Slant Range Sampling	4 m
Slant Range Resolution	5.7 m
Azimuth Pixel Spacing	3.89 m
Azimuth Resolution	6 m
Near Ground Range Resolution	8.1 m
Far Ground Range Resolution	5.87 m
Number of Pixels per Line	4096
Number of Lines	12288

Unprocessed Chilliwack SAR parameters

Date	Aug. 7, 1993
Initial Latitude	49° 23.4' N
Initial Longitude	121° 48.8' W
Final Latitude	49° 07.4' N
Initial Longitude	122° 17.9' W
Altitude Above Surface	6028 m
Aircraft Heading	233°
Aircraft Track	230°
Aircraft Pitch	1.3°
Antenna Azimuth (relative to aircraft)	265.3°
Approximate Look Direction	Port (138°)

Chilliwack SAR aircraft parameters

(Parameters derived from the CCRS CV-580 C-SAR MAID printout and flight logs)

APPENDIX III

Weights of Evidence Calculations

Sample Calculations  
(Format adapted from Bonham-Carter 1994a)

Predictor weights and Studentized contrast calculated for the Custer Gneiss.

$N\{T\}$  = total study area = 880,000 pixels

$N\{S\}$  = landslide area = 17740 pixels

$N\{B\}$  = Custer Gneiss area = 21420 pixels

$N\{B \cap S\}$  = Intersection area of landslides and Custer Gneiss = 2315 pixels

For a given 100 m by 100 m pixel:

Prior probability of landslide occurrence S:

$$P\{S\} = N\{S\}/N\{T\} = 17740/880000 = 0.02$$

Prior odds of landslide occurrence S:

$$O\{S\} = P\{S\}/(1-P\{S\}) = 0.02/(1-0.02) = 0.02$$

Posterior probability of landslide occurrence S, given the presence of binary pattern B:

$$P\{S|B\} = N\{B \cap S\}/N\{B\} = 2315/21420 = 0.1081$$

Posterior probability of landslide occurrence S, given the absence of binary pattern B:

$$\begin{aligned} P\{S|B^*\} &= N\{S \cap B^*\}/N\{B^*\} = (N\{S\} - N\{B \cap S\})/(N\{T\} - N\{B\}) \\ &= (17740 - 2315)/(880000 - 21420) \\ &= 0.0180 \end{aligned}$$

Posterior probability of binary pattern B being present, given the presence of landslide occurrence S:

$$P\{B|S\} = N\{B \cap S\}/N\{S\} = 2315/17740 = 0.1305$$

Posterior probability of binary pattern B being present, given the absence of landslide occurrence S:

$$\begin{aligned} P\{B|S^*\} &= N\{B \cap S^*\}/N\{S^*\} = (N\{B\} - N\{B \cap S\})/(N\{T\} - N\{S\}) \\ &= (21420 - 2315)/(880000 - 17740) \\ &= 0.0222 \end{aligned}$$

Posterior probability of binary pattern B being absent, given the presence of landslide occurrence S:

$$\begin{aligned} P\{B^*|S\} &= N\{B^* \cap S\}/N\{S\} = (N\{S\} - N\{B \cap S\})/N\{S\} \\ &= (17740 - 2315)/17740 \\ &= 0.8695 \end{aligned}$$

Posterior probability of binary pattern B being absent, given the absence of landslide occurrence S:

$$\begin{aligned} P\{B^*|S^*\} &= N\{B^* \cap S^*\}/N\{S^*\} = (N\{T\} - N\{B\} - (N\{S\} - N\{B \cap S\}))/N\{T\} - N\{S\} \\ &= (880000 - 21420 - 17740 + 2315)/(880000 - 17740) \\ &= 0.9778 \end{aligned}$$

Sufficiency ratio (likelihood ratio) for pattern B:

$$LS = P\{B|S\}/P\{B|S^*\} = 0.1305/0.0222 = 5.8896$$

Positive weight of evidence for pattern B:

$$W_+ = \ln(LS) = 1.7732$$

Variance of the positive weight of evidence for pattern B:

$$s(W_+) = \sqrt{\frac{1}{N\{B \cap S\}} + \frac{1}{N\{B \cap S^*\}}} = \sqrt{\frac{1}{2315} + \frac{1}{(21420 - 2315)}} = 0.0220$$

Necessity ratio (likelihood ratio) for pattern B:

$$LN = P\{B^*|S\}/P\{B^*|S^*\} = 0.8695/0.9778 = 0.8892$$

Negative weight of evidence for pattern B:

$$W^- = \ln(LN) = -0.1174$$

Variance of the negative weight of evidence for pattern B:

$$s(W^-) = \sqrt{\frac{1}{N\{B^* \cap S\}} + \frac{1}{N\{B^* \cap S^*\}}} = \sqrt{\frac{1}{(17740 - 2315)} + \frac{1}{(880000 - 21420 - 17740 + 2315)}} = 0.008$$

Contrast:

$$C = W^+ - W^- = 1.7732 - -0.1174 = 1.8906$$

Variance of the contrast C:

$$s(C) = \sqrt{s^2(W^+) + s^2(W^-)} = \sqrt{(0.0220)^2 + (-0.0081)^2} = 0.0235$$

Studentized value of the contrast C:

$$C/s(C) = 1.889/0.0235 = 80.5926$$

Posterior odds of landslide occurrence S, given the presence of binary pattern B:

$$O\{S|B\} = O\{S\} * LS = 0.02 * 5.8783 = 0.1212$$



**WEIGHTS BEDROCK GEOLOGY**

I.D. Number	Rock Group/Formation	Rock Type	Weights			Intersection			Conditional Posterior Probabilities												
			Total study area	Area N(B)	N(B a S)	N(B a S) (cells)	P(S B) (calc)	P(S B) (input)	P(S B) (calc)	P(S B) (calc)	P(S B) (calc)	P(S B) (calc)	P(S B) (calc)	P(S B) (calc)	P(S B) (calc)	P(S B) (calc)	P(S B) (calc)	P(S B) (calc)	P(S B) (calc)	P(S B) (calc)	P(S B) (calc)
12	Chatter Gneiss	Gneiss, pelitic schist	880000	21420	2315	0.1081	0.1880	0.1305	0.0222	0.8695	0.9778	5.8896	1.7732	0.0259	0.8892	-0.1174	0.0081	1.8906	0.0235	80.5926	0.1212
60	Chulivack Group	Pelite, ss, conglom.,...	17740	18185	1642	0.0903	0.0187	0.0926	0.0192	0.9074	0.9808	4.8244	1.5737	0.0259	0.9252	-0.0778	0.0080	1.6514	0.0271	61.0072	0.0993
41	Cultus Formation	Arg., ss, carb	0.02	15721	1232	0.0784	0.0191	0.0694	0.0168	0.9306	0.9832	4.1329	1.4190	0.0297	0.9465	-0.0550	0.0079	1.4740	0.0307	48.0142	0.0850
23	Spuzzum Pluton	gd, d, gd	30816	1787	1787	0.0580	0.0188	0.1007	0.0337	0.8993	0.9663	2.9211	1.0960	0.0244	0.9306	-0.0719	0.0080	1.1679	0.0257	45.5322	0.0616
14	Stollikum Schist	meta volca, phyllites,...	24837	1796	1796	0.0522	0.0192	0.0731	0.0273	0.9269	0.9727	2.6759	0.9843	0.0285	0.9530	-0.0482	0.0079	1.0325	0.0296	34.8816	0.0531
26	Peninsula Formation	ss, conglom	6148	394	394	0.0641	0.0199	0.0222	0.0067	0.9778	0.9933	3.3282	1.2024	0.0321	0.9844	-0.0158	0.0077	1.2182	0.0526	23.1433	0.0685
53	Ultramafic, gabbro	Ultramafic, gabbro	4548	299	299	0.0657	0.0199	0.0169	0.0049	0.9831	0.9951	3.4203	1.2297	0.0398	0.9880	-0.0121	0.0076	1.2418	0.0603	20.5873	0.0704
37	Dewdney Ck. Fm.	ss., arg., volca.	30708	1018	1018	0.0332	0.0197	0.0574	0.0344	0.9426	0.9656	1.6666	0.5108	0.0319	0.9762	-0.0241	0.0078	0.5348	0.0328	16.2967	0.0343
57	Ultramafic, gabbro	Ultramafic, gabbro	509	68	68	0.1336	0.0201	0.0038	0.0005	0.9962	0.9995	7.4947	2.0142	0.1303	0.9967	-0.0033	0.0076	2.0175	0.1305	15.4595	0.1542
54	Hozomeen Complex	Chert, pelite, volca,...	62352	1525	1525	0.0245	0.0198	0.0860	0.0705	0.9140	0.9295	1.2186	0.1977	0.0259	0.9834	-0.0167	0.0079	2.1144	0.0271	7.9087	0.0251
55	Hozomeen Complex	Mafic volcanics	22908	594	594	0.0259	0.0200	0.0335	0.0259	0.9665	0.9741	1.2939	0.2576	0.0416	0.9922	-0.0078	0.0077	0.2655	0.0423	6.2787	0.0266
33	Billhook Ck. Fm.	Int. volcanics	992	43	43	0.0433	0.0201	0.0024	0.0011	0.9976	0.9989	2.2024	0.7895	0.1559	0.9987	-0.0013	0.0076	0.7909	0.1561	5.0663	0.0453
22	Jackass Mountain Group	ss., arg., conglom.	6876	159	159	0.0231	0.0201	0.0090	0.0078	0.9910	0.9922	1.1506	0.1402	0.0802	0.9988	-0.0012	0.0076	0.1414	0.0806	1.7547	0.0237
36	Ladner Group	arg., slate, silt., tuff,...	26324	549	549	0.0209	0.0201	0.0309	0.0259	0.9691	0.9701	1.0353	0.0347	0.0431	0.9989	-0.0011	0.0077	0.0358	0.0438	8.162	0.0213
10	Princeton Group	ss., conglom., arg.	5502	83	83	0.0151	0.0202	0.0047	0.0063	0.9953	0.9937	0.7445	-0.2951	0.1106	1.0016	0.0016	0.0076	-0.2967	0.1109	-2.6763	0.0153
24	Brekendige Gneiss	Felsic and mafic gneiss	7058	89	89	0.0126	0.0202	0.0050	0.0081	0.9950	0.9919	0.6207	-0.4769	0.1067	1.0031	0.0031	0.0076	-0.4799	0.1069	-4.4877	0.0128
28	Eagle Plutonic Complex	Diorite and amphibolite	4806	52	52	0.0108	0.0202	0.0029	0.0055	0.9971	0.9945	0.5317	-0.6318	0.1394	1.0026	0.0026	0.0076	-0.6344	0.1396	-4.5429	0.0109
6	Coquihalla Fm.	Pyroclastics and flows	7086	72	72	0.0102	0.0202	0.0041	0.0081	0.9959	0.9919	0.4989	-0.6953	0.1185	1.0041	0.0041	0.0076	-0.6994	0.1187	-5.8920	0.0103
21	Paayten Group	ss., conglom., arg.	18721	2	2	0.0001	0.0206	0.0001	0.0217	0.9999	0.9783	0.0052	-2.2604	0.7071	1.0221	0.0218	0.0076	-2.2822	0.7072	-7.4694	0.0001
8	Needle Peak Pluton	Granodiorite	25477	335	335	0.0135	0.0204	0.0189	0.0292	0.9811	0.9708	0.6476	-0.4344	0.0550	1.0106	0.0105	0.0077	-0.4450	0.0555	-8.0130	0.0133
7	Chulivack Batholith	Granodiorite	31164	420	420	0.0135	0.0204	0.0237	0.0357	0.9763	0.9643	0.6640	-0.4095	0.0491	1.0124	0.0123	0.0077	-0.4218	0.0497	-8.4831	0.0137
5	Mount Barr Batholith	Granodiorite	22149	265	265	0.0120	0.0204	0.0149	0.0254	0.9851	0.9746	0.5886	-0.5300	0.0618	1.0107	0.0107	0.0076	-0.5407	0.0623	-8.6830	0.0121
13	Settler Schist	Schist, amphibolite	34286	405	405	0.0118	0.0205	0.0228	0.0393	0.9772	0.9607	0.5810	-0.5430	0.0500	1.0171	0.0170	0.0077	-0.5600	0.0506	-11.0729	0.0120
29	Eagle Plutonic Complex	Granite and pegmatite	14036	38	38	0.0027	0.0205	0.0021	0.0162	0.9979	0.9838	0.1319	-2.0253	0.1624	1.0143	0.0142	0.0076	-2.0396	0.1626	-12.7440	0.0027
11	Early Tertiary Intrusions	Granodiorite	16746	45	45	0.0027	0.0205	0.0025	0.0194	0.9975	0.9806	0.1310	-2.0328	0.1493	1.0172	0.0170	0.0076	-2.0498	0.1495	-13.7145	0.0027
27	Eagle Plutonic Complex	Granodiorite and gneiss	53659	288	288	0.0054	0.0211	0.0162	0.0619	0.9838	0.9381	0.2623	-1.3383	0.0591	1.0487	0.0475	0.0077	-1.3859	0.0596	-23.2613	0.0054
15	Scauzey Pluton	Granodiorite, quartz monz	131597	576	576	0.0044	0.0229	0.0325	0.1520	0.9675	0.8480	0.2137	-1.5433	0.0418	1.1409	0.1318	0.0077	-1.6751	0.0425	-39.4451	0.0044

Calculations for determining weights for the bedrock geology predictor map.

WEIGHTS	FAULTS				Conditional Posterior Probabilities																	
	Total study area	N{I}	cells	(input)	Intersection	N{B n S}	P{S B}	P{S B*}	P{B S}	P{B S*}	P{B* S}	P{B* S*}	LS	W+	s(W+)	LN	W-	s(W-)	C	s(C)	C/s(C)	
Area of slides	N{S}	cells	(input)	N{B}	(cells)	(input)	(calc)	(calc)	(calc)	(calc)	(calc)	(calc)	(calc)	(calc)	(calc)	(calc)	(calc)	(calc)	(calc)	(calc)	(calc)	(calc)
Prior Probability	P{S}	0.02	(calc)	17740	0.02	(calc)	0.0200	0.0224	0.0139	0.9776	0.9861	1.6118	0.4773	0.0510	0.9914	-0.0087	0.0077	0.4860	0.0516	9.4208		
Prior Odds	O{S}	0.02	(calc)	880000	0.0321	(calc)	0.0194	0.0876	0.0534	0.9124	0.9466	1.6412	0.4954	0.0258	0.9638	-0.0368	0.0079	0.5322	0.0270	19.7233		
100	12369	47577	1554	2706	0.0335	0.0188	0.1525	0.0905	0.8475	0.9095	1.6859	1.6859	0.5223	0.0196	0.9318	-0.0707	0.0082	0.5930	0.0212	27.9477		
200	80722	102767	3548	4411	0.0345	0.0183	0.2000	0.1151	0.8000	0.8849	1.7381	1.7381	0.5528	0.0171	0.9040	-0.1009	0.0085	0.6537	0.0191	34.2767		
300	123759	152645	5604	6468	0.0356	0.0176	0.2486	0.1384	0.7514	0.8616	1.7964	1.7964	0.5858	0.0153	0.8721	-0.1369	0.0087	0.7227	0.0176	40.9502		
400	171841	194177	7475	8477	0.0367	0.0167	0.3159	0.1705	0.6841	0.8295	1.8524	1.8524	0.6165	0.0136	0.8247	-0.1927	0.0092	0.8092	0.0164	49.3328		
500	216443	235700	9303	9994	0.0376	0.0159	0.3646	0.1918	0.6354	0.8082	1.9010	1.9010	0.6424	0.0127	0.7862	-0.2406	0.0095	0.8830	0.0158	55.7540		
600	253666	269375	10553	11053	0.0385	0.0150	0.4214	0.2165	0.5786	0.7835	1.9460	1.9460	0.6658	0.0118	0.7386	-0.3031	0.0099	0.9688	0.0154	62.7967		
700	287388	305300	11483	11806	0.0392	0.0140	0.4778	0.2412	0.5222	0.7588	1.9812	1.9812	0.6837	0.0111	0.6881	-0.3738	0.0105	1.0575	0.0152	69.3902		
800	321047				0.0395	0.0131	0.5244	0.2626	0.4756	0.7374	1.9973	1.9973	0.6918	0.0106	0.6449	-0.4386	0.0110	1.1304	0.0152	74.2134		
900					0.0399	0.0124	0.5634	0.2826	0.4366	0.7174	1.9935	1.9935	0.6899	0.0102	0.6086	-0.4965	0.0114	1.1864	0.0153	77.4137		
1000					0.0399	0.0118	0.5949	0.3002	0.4051	0.6998	1.9818	1.9818	0.6840	0.0099	0.5789	-0.5466	0.0119	1.2306	0.0155	79.5335		
1100					0.0385	0.0113	0.6231	0.3205	0.3769	0.6795	1.9441	1.9441	0.6648	0.0097	0.5547	-0.5893	0.0123	1.2541	0.0157	80.0665		
1200					0.0376	0.0109	0.6473	0.3408	0.3527	0.6592	1.8996	1.8996	0.6416	0.0095	0.5350	-0.6255	0.0127	1.2671	0.0159	79.8096		
1300					0.0368	0.0106	0.6655	0.3586	0.3345	0.6414	1.8556	1.8556	0.6182	0.0094	0.5215	-0.6510	0.0131	1.2692	0.0161	78.9752		

Variation of weights of evidence with cumulative distance from faults.

WEIGHTS LINEAMENTS

Distance (m)	Weights				Conditional Posterior Probabilities															
	Total study area Area of slides Prior Probability Prior Odds	N(T) N(S) P(S) O(S)	cells cells (calc) (calc)	N{B n S} (cells) (input)	P{S B} (calc)	P{S B*}	P{B S}	P{B S*}	P{B* S}	P{B* S*}	LS	W+	s(W+)	LN	W-	s(W-)	C	s(C)	C/s(C)	O(S B)
<100				1046	0.0258	0.0199	0.0590	0.0458	0.9410	0.9542	1.2876	0.2528	0.0313	0.9862	-0.0139	0.0078	0.2667	0.0323	8.2590	0.0265
200				3706	0.0249	0.0192	0.2089	0.1681	0.7911	0.8319	1.2428	0.2174	0.0166	0.9509	-0.0503	0.0085	0.2677	0.0187	14.3203	0.0256
300				6042	0.0257	0.0181	0.3406	0.2652	0.6594	0.7348	1.2845	0.2503	0.0130	0.8974	-0.1083	0.0093	0.3586	0.0160	22.3742	0.0264
400				7581	0.0265	0.0171	0.4273	0.3236	0.5727	0.6764	1.3206	0.2781	0.0116	0.8466	-0.1665	0.0100	0.4446	0.0154	28.9654	0.0272
500				8980	0.0272	0.0159	0.5062	0.3724	0.4938	0.6276	1.3594	0.3071	0.0107	0.7868	-0.2398	0.0108	0.5469	0.0152	36.0226	0.0280
600				10797	0.0284	0.0139	0.6086	0.4291	0.3914	0.5709	1.4182	0.3494	0.0098	0.6856	-0.3775	0.0121	0.7269	0.0155	46.7855	0.0292
700				11938	0.0290	0.0124	0.6729	0.4635	0.3271	0.5365	1.4520	0.3730	0.0093	0.6096	-0.4950	0.0132	0.8680	0.0161	53.7481	0.0299
800				13131	0.0296	0.0105	0.7402	0.4986	0.2598	0.5014	1.4844	0.3950	0.0089	0.5182	-0.6574	0.0148	1.0524	0.0173	60.9906	0.0305
900				14081	0.0299	0.0090	0.7937	0.5302	0.2063	0.4698	1.4972	0.4036	0.0086	0.4390	-0.8233	0.0166	1.2269	0.0187	65.6753	0.0308
1000				14851	0.0301	0.0075	0.8371	0.5549	0.1629	0.4451	1.5086	0.4112	0.0083	0.3659	-1.0054	0.0187	1.4166	0.0204	69.2722	0.0310
1100				15416	0.0300	0.0063	0.8690	0.5774	0.1310	0.4226	1.5049	0.4087	0.0082	0.3100	-1.1711	0.0208	1.5799	0.0224	70.6602	0.0310
1200				15823	0.0299	0.0055	0.8919	0.5983	0.1081	0.4047	1.4983	0.4043	0.0081	0.2670	-1.3205	0.0229	1.7248	0.0243	71.0293	0.0308
1300				16259	0.0298	0.0044	0.9165	0.6140	0.0835	0.3860	1.4927	0.4006	0.0080	0.2163	-1.5312	0.0260	1.9318	0.0272	70.9351	0.0307
1400				16575	0.0296	0.0037	0.9343	0.6312	0.0657	0.3688	1.4802	0.3922	0.0079	0.1781	-1.7255	0.0294	2.1177	0.0304	69.6777	0.0305
1500				16827	0.0294	0.0030	0.9485	0.6451	0.0515	0.3549	1.4703	0.3855	0.0078	0.1450	-1.9309	0.0331	2.3164	0.0341	68.0168	0.0303

Variation of weights of evidence with cumulative distance from lineaments.

**WEIGHTS PLUTONIC CONTACTS**

Distance (m)	Area N(B) (cells) (input)	Intersection N(B∩S) (cells) (input)	cells cells (input) (input)	Conditional Posterior Probabilities				W.	s(W.)	C	s(C)	C/s(C)	O(S B)					
				P(S B) (calc)	P(S B*) (calc)	P(B S) (calc)	P(B S*) (calc)							P(B+ S) (calc)	LN			
<100	14904	281	0.0189	0.0202	0.0158	0.0170	0.9842	0.9830	0.9340	-0.0683	0.0602	1.0011	0.0011	0.0076	-0.0694	0.0607	-1.1431	0.0192
200	54754	1009	0.0184	0.0203	0.0569	0.0623	0.9431	0.9377	0.9125	-0.0916	0.0318	1.0058	0.0058	0.0078	-0.0974	0.0327	-2.9753	0.0188
250	82252	1510	0.0184	0.0203	0.0851	0.0936	0.9149	0.9064	0.9090	-0.0954	0.0260	1.0094	0.0094	0.0079	-0.1048	0.0272	-3.8580	0.0187
300	92080	1676	0.0182	0.0204	0.0945	0.1048	0.9055	0.8952	0.9011	-0.1041	0.0247	1.0116	0.0115	0.0080	-0.1157	0.0259	-4.4642	0.0185
400	118085	2158	0.0183	0.0205	0.1216	0.1344	0.8784	0.8656	0.9048	-0.1060	0.0217	1.0148	0.0147	0.0081	-0.1147	0.0232	-4.9482	0.0186
500	142719	2594	0.0182	0.0205	0.1462	0.1625	0.8538	0.8375	0.8998	-0.1056	0.0198	1.0194	0.0193	0.0082	-0.1249	0.0214	-5.8212	0.0185
600	174705	3133	0.0179	0.0207	0.1766	0.1990	0.8234	0.8010	0.8876	-0.1193	0.0180	1.0279	0.0275	0.0084	-0.1468	0.0199	-7.3883	0.0183
700	196896	3501	0.0178	0.0208	0.1974	0.2243	0.8026	0.7757	0.8799	-0.1280	0.0171	1.0347	0.0341	0.0085	-0.1621	0.0190	-8.5130	0.0181
800	213610	3783	0.0177	0.0209	0.2132	0.2433	0.7868	0.7567	0.8763	-0.1320	0.0164	1.0398	0.0390	0.0086	-0.1710	0.0185	-9.2448	0.0180
900	245796	4335	0.0176	0.0211	0.2211	0.2521	0.7789	0.7479	0.8771	-0.1311	0.0161	1.0414	0.0406	0.0086	-0.1717	0.0183	-9.4042	0.0180
1000	266756	4688	0.0176	0.0213	0.2643	0.3039	0.7357	0.6961	0.8695	-0.1399	0.0147	1.0570	0.0554	0.0088	-0.1953	0.0172	-11.3623	0.0179
1100	286655	5034	0.0176	0.0214	0.2838	0.3266	0.7162	0.6734	0.8688	-0.1406	0.0142	1.0636	0.0617	0.0090	-0.2023	0.0168	-12.0330	0.0179
1200	304420	5333	0.0175	0.0216	0.3006	0.3469	0.6994	0.6531	0.8667	-0.1431	0.0138	1.0708	0.0684	0.0091	-0.2115	0.0165	-12.7948	0.0178
1300	323837	5656	0.0175	0.0217	0.3188	0.3690	0.6812	0.6310	0.8640	-0.1462	0.0134	1.0795	0.0765	0.0092	-0.2227	0.0163	-13.6917	0.0178
1500	361290	6321	0.0175	0.0220	0.3563	0.4117	0.6437	0.5883	0.8655	-0.1444	0.0127	1.0941	0.0899	0.0095	-0.2343	0.0158	-14.8047	0.0178
1750	405571	7122	0.0176	0.0224	0.4015	0.4621	0.5985	0.5379	0.8688	-0.1407	0.0120	1.1127	0.1068	0.0098	-0.2475	0.0155	-15.9986	0.0179
2000	439743	7757	0.0176	0.0227	0.4373	0.5010	0.5627	0.4990	0.8728	-0.1361	0.0115	1.1277	0.1373	0.0101	-0.2563	0.0153	-16.7620	0.0180
2250	475497	8413	0.0177	0.0231	0.4742	0.5417	0.5258	0.4583	0.8755	-0.1330	0.0110	1.1472	0.1635	0.0108	-0.2703	0.0152	-17.7949	0.0180
2500	504475	8961	0.0178	0.0234	0.5051	0.5747	0.4949	0.4253	0.8790	-0.1290	0.0107	1.1635	0.1514	0.0112	-0.2990	0.0152	-19.6450	0.0181
2750	535999	9537	0.0178	0.0238	0.5376	0.6106	0.4624	0.3894	0.8805	-0.1273	0.0103	1.1874	0.1899	0.0115	-0.3149	0.0153	-20.5644	0.0182
3000	562244	10027	0.0178	0.0243	0.5652	0.6404	0.4348	0.3596	0.8826	-0.1249	0.0101	1.2092	0.1899	0.0115	-0.3149	0.0153	-20.5644	0.0182
3250	588219	10583	0.0180	0.0245	0.5966	0.6699	0.4034	0.3301	0.8905	-0.1160	0.0098	1.2222	0.2007	0.0120	-0.3126	0.0157	-19.9224	0.0185
3500	611071	11104	0.0182	0.0247	0.6259	0.6958	0.3741	0.3042	0.8996	-0.1058	0.0096	1.2297	0.2068	0.0129	-0.3192	0.0159	-20.0226	0.0186
3750	632733	11564	0.0183	0.0250	0.6519	0.7204	0.3481	0.2796	0.9049	-0.1000	0.0094	1.2451	0.2192	0.0133	-0.3227	0.0162	-19.8993	0.0187
4000	651380	11976	0.0184	0.0252	0.6751	0.7415	0.3249	0.2585	0.9104	-0.0939	0.0092	1.2571	0.2288	0.0139	-0.3223	0.0166	-19.4551	0.0189
4250	669920	12407	0.0185	0.0254	0.6994	0.7625	0.3006	0.2375	0.9172	-0.0865	0.0091	1.2660	0.2359	0.0143	-0.3299	0.0169	-19.5337	0.0189
4500	685282	12741	0.0186	0.0257	0.7182	0.7800	0.2818	0.2200	0.9208	-0.0825	0.0089	1.2807	0.2474	0.0143	-0.3299	0.0169	-19.5337	0.0189
4750	700650	13008	0.0186	0.0264	0.7333	0.7975	0.2667	0.2025	0.9195	-0.0840	0.0089	1.3172	0.2755	0.0147	-0.3595	0.0172	-20.9144	0.0189
5000	713826	13228	0.0185	0.0272	0.7457	0.8125	0.2543	0.1875	0.9177	-0.0859	0.0088	1.3566	0.3050	0.0151	-0.3908	0.0175	-22.3847	0.0189
5250	727504	13492	0.0185	0.0279	0.7605	0.8281	0.2395	0.1719	0.9184	-0.0851	0.0086	1.3928	0.3313	0.0156	-0.4164	0.0178	-23.3607	0.0189
5500	738281	13691	0.0185	0.0286	0.7718	0.8403	0.2282	0.1597	0.9184	-0.0851	0.0086	1.4295	0.3573	0.0159	-0.4425	0.0181	-24.4072	0.0189
5750	749895	13915	0.0186	0.0294	0.7844	0.8535	0.2156	0.1465	0.9190	-0.0845	0.0086	1.4722	0.3868	0.0164	-0.4713	0.0185	-25.4630	0.0189
6000	759535	14097	0.0186	0.0302	0.7946	0.8645	0.2054	0.1355	0.9192	-0.0843	0.0085	1.5157	0.4159	0.0168	-0.5002	0.0189	-26.5334	0.0189

Variation of weights of evidence with cumulative distance from plutonic contacts.

**Contingency Table**

	(input)	N(B1)	expected	N(B1*)	observed	expected	TOTAL
N{B1 n S}	11053	observed	1442	observed	249	873	2315
N{B2 n S}	2315	(input)	9611	observed	6438	5814	15425
N{B1* n S}	6687	(calc)	11053	observed	6687	6687	17740
N{B2* n S}	15425	(calc)					
N{B1 n B2 n S}	2066	(input)					
N{S}	17740	(input)					
						X <sup>2</sup>	822.67

Chi-Square Test:

**Intersection**

N{B1 n B2 n S}

(cells)	Lineaments	Faults	4050 Slopes	3040 Slopes	2030 Slopes
(input)	9727				
Lineaments	-				
Custer Gneiss	2315	2066	160	514	859
Chilliwaack Group	1420	722	94	418	632
Cultus Formation	893	370	180	322	424
Ultramafic, gabbro	183	299	0	0	97
Peninsula Formation	344	394	0	11	258
Spuzzum Pluton	1679	140	57	220	438
Stollieun Schist	1296	738	147	406	452
40°-50° Slopes	1059	712	-	0	0
Dewdney Ck. Fm.	1018	789	0	135	439
30°-40° Slopes	3320	2067	0	-	0
20°-30° Slopes	5580	3947	0	0	-

**X<sup>2</sup>**

Lineaments	Cramer Coef	Faults	Cramer Coef	4050 Slopes	Cramer Coef	3040 Slopes	Cramer Coef	2030 Slopes	Cramer Coef	Average
Lineaments	0.0000	265.94	0.1224							0.1224
Custer Gneiss	0.1236	822.67	0.2153	1.52	0.0093	11.61	0.0256	12.78	0.0268	0.0801
Chilliwaack Group	0.0472	259	0.1208	1.12	0.0079	39.64	0.0473	17.57	0.0315	0.0509
Cultus Formation	0.1724	587.15	0.1819	453.08	0.1598	36.11	0.0451	0.2	0.0034	0.1125
Ultramafic, gabbro	0.1336	183.99	0.1018	20.55	0.0340	74.06	0.0646	0.26	0.0038	0.0676
Peninsula Formation	0.0180	243.78	0.1172	27.23	0.0392	72.14	0.0638	180.38	0.1008	0.0678
Spuzzum Pluton	0.0369	2510.53	0.3762	33.06	0.0432	66.72	0.0613	77.06	0.0659	0.1167
Stollieun Schist	0.0896	17.11	0.0311	59.24	0.0578	122.46	0.0831	0.69	0.0062	0.0535
40°-50° Slopes	0.0318	0.61	0.0059	-	0.0000	-	0.0000	-	0.0000	0.0075
Dewdney Ck. Fm.	0.0787	106.23	0.0774	72.99	0.0641	27.41	0.0393	41.69	0.0485	0.0616
30°-40° Slopes	0.0824	14.31	0.0284	-	0.0000	-	0.0000	-	0.0000	0.0222
20°-30° Slopes	0.0549	46.41	0.0511	-	0.0000	-	0.0000	-	0.0000	0.0212
Average	0.0790		0.0875		0.0502		0.0558		0.0341	0.0613

Contingency table, intersection values, chi-square, and Cramer coefficients to test conditional independence between binary predictor maps.

APPENDIX IV

Non-geologic Acronyms and Terminology

BC DTM	British Columbia Digital Terrain Model	1:20,000 scale topographic maps in digital format acquired from BC Maps in Victoria, B.C. Maps include contours, planimetric data, and a DEM.
C-band SAR	Synthetic Aperture Radar	Microwave sensor with wavelength of 5.66 cm. SAR imagery will look different with different sensor wavelengths.
CIR	Color Infrared	Color infrared imagery. Useful for investigating vegetation type and health.
decimated		A 3000 pixel by 3000 line image is decimated when pixels and lines must be removed from the image so that it can fit on a 1024 by 768 computer screen.
DEM	Digital Elevation Model	A grid of pixels (raster image) where each grey level within a pixel contains an elevation value.
DTM	Digital Terrain Model	Topographic maps in digital format acquired from BC Maps in Victoria, B.C. Maps include contours, planimetric data, and a DEM.
ERS-1 SAR		SAR imagery collected by the European Space Agency satellite.
FORTRAN		A computer language best used for linear programming.
GCPs	Ground Control Points	Points of known x, y, and z used to spatially correct a distorted image to a undistorted image such as a map.
geocoded		An image is geocoded when distortions have been removed and it can be used as a map.
GIS	Geographic Information System(s)	Software and technology used to store and model spatial and associated attribute data.
hardcopy		information on paper
HH polarization		Radar signals are both transmitted and received in the horizontal plane. This is one of four polarization modes: HH, HV, VH, VV. SAR imagery will look different with different polarization.
IDRISI		Low cost PC raster based GIS software with a broad range of functionality.

Landsat MSS	Landsat Mutlispectral Scanner	Optical satellite imagery with 60 m resolution and capable of sensing in four areas in the visible and infrared regions of the electromagnetic spectrum.
Landsat TM	Landsat Thematic Mapper	Optical satellite imagery with 30 m resolution and capable of sensing in seven areas in the visible and infrared regions of the electromagnetic spectrum.
Lee adaptive filter		A square matrix that passes over and smoothes a radar image by de-emphasizing local areas of brightness.
PCI EASI/PACE		PC based Canadian image processing software capable of importing, altering, and outputting digital raster and vector images.
predictor map		A layer of spatial data (i.e.: bedrock geology) that is thought to influence the spatial location of the response variable (i.e. landslides).
radiometric quality		Referring to the visual aesthetics and interpretability of an image.
RADARSAT		Canadian SAR satellite to be launched on September 20, 1995. Also the name of the Canadian company responsible for the distribution and marketing of the SAR imagery.
resolution		Describes the amount of spectral or spatial detail seen in a image. Smaller objects can be seen on earth, (i.e. more spatial detail) in high spatial resolution imagery because the pixel size is smaller.
SAR	Synthetic Aperture Radar	Airborne or satellite microwave sensor that produces < 12 m resolution images from the energy reflected from the ground.
softcopy		Data in digital format.
SPANS	Spatial Analysis Software	PC raster based Canadian GIS software with strong modelling capability.
speckle		Grainy, salt-and-pepper pattern seen in unprocessed SAR images that results from random constructive and destructive interference of radar waves.

SPOT	Systeme Pour l'Observation de la Terre	French 10-20 m resolution optical satellite
TRIM	Terrain Resources Inventory Mapping	1:20,000 scale topographic maps in digital format acquired from BC Maps in Victoria, B.C. Maps include contours, planimetric data, and a DEM.
UTM	Universal Transverse Mercator	Worldwide metric coordinate system derived from latitudes and longitudes.
VV polarization		Radar signals are both transmitted and received in the vertical plane. This is one of four polarization modes: HH, HV, VH, VV. SAR imagery will look different with different polarization.
X-band SAR	Synthetic Aperture Radar	Microwave sensor with wavelength of 3.2 cm. SAR imagery will look different with different sensor wavelengths.